INFORMATION TO USERS

This manuscript has been reproduced from the microfilm master. UMI films the text directly from the original or copy submitted. Thus, some thesis and dissertation copies are in typewriter face, while others may be from any type of computer printer.

The quality of this reproduction is dependent upon the quality of the copy submitted. Broken or indistinct print, colored or poor quality illustrations and photographs, print bleedthrough, substandard margins, and improper alignment can adversely affect reproduction.

In the unlikely event that the author did not send UMI a complete manuscript and there are missing pages, these will be noted. Also, if unauthorized copyright material had to be removed, a note will indicate the deletion.

Oversize materials (e.g., maps, drawings, charts) are reproduced by sectioning the original, beginning at the upper left-hand corner and continuing from left to right in equal sections with small overlaps. Each original is also photographed in one exposure and is included in reduced form at the back of the book.

Photographs included in the original manuscript have been reproduced xerographically in this copy. Higher quality 6" x 9" black and white photographic prints are available for any photographs or illustrations appearing in this copy for an additional charge. Contact UMI directly to order.

U·M·I

University Microfilms International
A Bell & Howell Information Company
300 North Zeeb Road, Ann Arbor, MI 48106-1346 USA
313/761-4700 800/521-0600

Reproduced with permission of the copyright owner. Further reproduction prohibited without permission.

Reproduced with permission of the copyright owner. Further reproduction prohibited without permission.

Order Number 9432362

Electron tunneling dynamics in engineered semiconductor nanostructures and applications to efficient solar cells

Mohaidat, Jihad Mansour, Ph.D.

City University of New York, 1994

Copyright ©1994 by Mohaidat, Jihad Mansour. All rights reserved.

U·M·I
300 N. Zeeb Rd.
Ann Arbor, MI 48106

Reproduced with permission of the copyright owner. Further reproduction prohibited without permission.

Reproduced with permission of the copyright owner. Further reproduction prohibited without permission.

Electron Tunneling Dynamics in Engineered Semiconductor Nanostructures and Applications to Efficient Solar Cells

By

Jihad M. Mohaidat

A dissertation submitted to the Graduate Faculty in Engineering in partial fulfillment of the requirements for the degree of Doctor of Philosophy, The City University of New York.

1994

Reproduced with permission of the copyright owner. Further reproduction prohibited without permission.

© 1994
Jihad M. Mohaidat
All rights reserved

Reproduced with permission of the copyright owner. Further reproduction prohibited without permission.

This manuscript has been read and accepted for the Graduate Faculty in Engineering in satisfaction of the dissertation requirement for the degree of Doctor of Philosophy.

4/27/94
Date

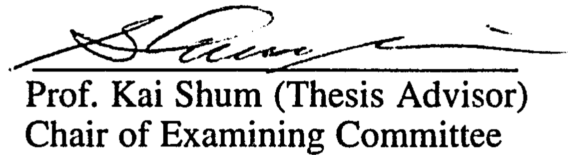

Prof. Kai Shum (Thesis Advisor)
Chair of Examining Committee

4/29/94
Date

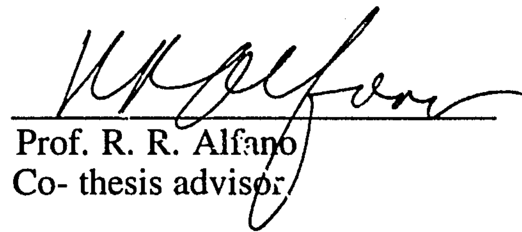

Prof. R. R. Alfano
Co- thesis advisor

5/2/94
Date

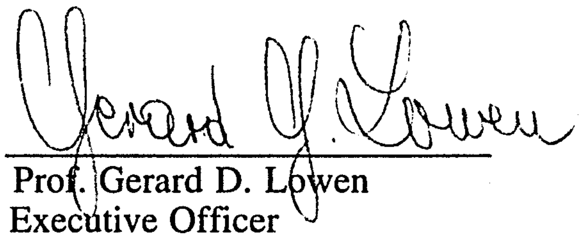

Prof. Gerard D. Lowen
Executive Officer

Prof. Ping Pei Ho
Prof. Roger Dorsinville
Prof. Fred Pollak

Supervisory Committee

The City University of New York

Reproduced with permission of the copyright owner. Further reproduction prohibited without permission.

Abstract

Electron Tunneling Dynamics in Engineered Semiconductor Nanostructures and Applications to Efficient Solar Cells

by

Jihad M. Mohaidat

Advisor: Kai Shum, Associate Professor of Electrical Engineering

Co-Advisor: Robert Alfano, Distinguished Professor of Science and Engineering

This thesis investigates the electron tunneling dynamics in engineered semiconductor nanostructures in the presence of electron-hole and electron-phonon interactions for device and solar applications. The temporal dynamics of a traveling electron wave packet in a double barrier structure was calculated as a function of wave packet's central incident energy by calculating the charge build-up inside the quantum well. As time passes 40 fs features associated with resonance started to develop. The electron tunneling dynamics problem were also extended to include electron-hole interaction on the coherent oscillation of a photoexcited electron wave packet in a double quantum well structure. It is shown both in energy and time domains that the electron hole interaction affect the electron wave packet's oscillation period by as much as 15%. This method was extended to include the presence of electron-plane wave and electron-localized LO phonon interactions on the dynamics of electron tunneling. It was shown that the tunneling

Reproduced with permission of the copyright owner. Further reproduction prohibited without permission.

current and charge build-up decreases in the presence of these LO phonon modes while the tunneling times are not affected.

One of the key aspects of this thesis is the use of electron resonant tunneling in MQW based solar cell structures for the purpose of high energy conversion efficiency. By incorporating tunneling through a MQW structure with different quantum well sizes in a p-i-n structure, higher efficiency was achieved by eliminating intrinsic losses associated with the single band gap solar cell structures. The effect of MQW solar cell structures made with small quantum well material band-gap such as that of InAs in InAs/GaInAs structures and a large band-gap as that of GaAs in GaAs/AlGaAs were presented.

Reproduced with permission of the copyright owner. Further reproduction prohibited without permission.

To my parents,

Mansour and Fatimah Mohaidat

Reproduced with permission of the copyright owner. Further reproduction prohibited without permission.

ACKNOWLEDGMENTS

I would like to thank and gratefully acknowledge my thesis advisor Professor Kai Shum. His patience, guidance, vast knowledge, and willingness to spend his valuable time to listen, direct to what is next, and teaching me how to be first were of enormous help in achieving the research goals.

Sincere thanks to Professor Robert Alfano for his advice, support, and valuable discussions.

I am obliged to Professors Roger Dorsinville, Ping Pei Ho and Fred Pollak for serving on my doctoral committee. I would like also to take this opportunity to thank all of the Institute for Ultrafast Spectroscopy and Lasers staff for their friendly support and valuable assistance. I thank Oxford Lasers for partial support to carry out this research.

Last but not least I would like to thank and pay my respect and love to my parents for their endless support and love. Their sacrifice and understanding shed happiness to a most difficult time.

Reproduced with permission of the copyright owner. Further reproduction prohibited without permission.

TABLE OF CONTENTS

Abstract iv

Acknowledgments vii

Table of contents viii

Lists of figures xi

Chapter One " Introduction"

1.1 Background 1

1.2 Thesis statement 7

1.3 Thesis Organization 8

1.4 References 10

Chapter Two "Dynamics of a traveling electron wave packet in a double barrier structure"

2.1 Introduction 15

2.2 Theory 16

2.3 Results and discussion 29

2.4 References 34

Chapter Three "Excitonic effects on the coherent oscillation of a photoexcited electron wave packet in coupled double quantum wells"

3.1 Introduction 46

3.2 Theory 48

3.3 Results and discussion 52

3.4 References 55

Reproduced with permission of the copyright owner. Further reproduction prohibited without permission.

Chapter Four " Electron Tunneling Dynamics Through a Double Barrier structure in the Presence of LO Phonon Modes"

4.1 Introduction 61

4.2 Theory 63

4.3 Results and Discussion 76

4.4 References 79

Chapter Five " Ultrafast Charging Dynamics in a double Barrier Structure in the Presence of Localized Phonon Modes"

5.1 Introduction 84

5.2 Localized phonon modes dispersion relations 85

5.2.1 Interface Phonon modes 87

5.2.2 Confined Phonon modes 91

5.3 Theory 93

5.4 Results and Discussion 94

5.5 References 98

Chapter Six "Barrier Potential Design Criteria in Multiple Quantum Well Based Solar Cell Structures"

6.1 Introduction 103

6.2 Theory 107

6.3 Results and Discussion 113

6.4 References 118

Reproduced with permission of the copyright owner. Further reproduction prohibited without permission.

Chapter Seven " Summary "

7.1 Summary 128

Chapter Eight "Future Directions

8.1 Introduction 131

8.2 Electron tunneling in the presence of
Γ-X mixing 131

8.3 4 to 8 μm wide band infrared photodetector 132

Appendices 130

A.1 A FORTRAN-77 program for the generation of chapter
two figures 134

A.2 A FORTRAN-77 program for the generation of chapter
three figures 136

A.3 A FORTRAN-77 program for the generation of chapters
Four and five figures 138

A.4 A FORTRAN-77 program for the generation of chapter six
figures 141

Bibliography 144

Reproduced with permission of the copyright owner. Further reproduction prohibited without permission.

LIST OF FIGURES

Chapter 1

Fig. (1.1) A semilog plot of the measured current voltage characteristics at 200K, 300K, and 400K. (After Esaki, phys. Rev. 109, 603 (1957)............................... 12

Fig. (1.2) (a) Domains relevant to the single barrier tunneling structure for $E<V$. (b) The wave function in the different domains, showing the decay of the wave function inside the barrier region and decrease in amplitude of the transmitted wave. (c) Transmission coefficient T versus E/V.. 13

Fig. (1.3) Current voltage characteristic of a double barrier resonant tunneling diode. The position of the quasi bound state with respect to incoming energy is also shown.. 14

Chapter two

Fig. (2.1) A schematic diagram of the GaAs-AlGaAs double barrier structure used in our simulation. The structure consists of a 60-Å GaAs quantum well and two 30-Å AlGaAs barriers of 280 meV potential height.. 35

Fig. (2.2) A 3-D plot of charge build up inside the quantum well of a double barrier structure as a function of

Reproduced with permission of the copyright owner. Further reproduction prohibited without permission.

both time and wave packet's central incident energy.......36

Fig. (2.3) The time evolution of charge inside the quantum well of the double barrier structure shown in Fig.(2.1) as a function of wave packet's central incident energy between 10-60 fs 37

Fig. (2.4) The time evolution of charge inside the quantum well of a double barrier structure (shown in Fig.(2.1)) as a function of wave packet's central incident energy between 70-150 fs 38

Fig. (2.5) The time evolution of charge inside the quantum well of the double barrier structure shown in Fig.(2.1) as a function of wave packet's central incident energy between 200-450 fs 39

Fig. (2.6) A schematic diagram showing in the top portion a typical energy spectrum of a Gaussian wave packet with central energy E. The lower portion shows the position of the quasi bound state centered at E and has an energy spread of 2Δ. 40

Fig. (2.7) The temporal behavior of the charge build-up resonance peak position and bandwidth of the first excited quasi bound state. The peak position and bandwidth reach a fixed value after about 300 fs. 41

Fig. (2.8) The temporal behavior of charge build-up at the ground state of the double barrier structure shown in Fig.(2.1) with wave packet's energy matching and close to the resonant energy.......................................42

Reproduced with permission of the copyright owner. Further reproduction prohibited without permission.

Fig. (2.9) The temporal behavior of charge build-up at the first excited state of the double barrier structure shown in Fig. (2.1) with wave packet's energy matching and close to the resonant energy....................43

Fig. (2.10) The time evolution of charges inside the quantum well of the double barrier structure of chapter two as a function of wave packet's central incident energy with a wave packet's spatial width of 900-Å........44

Fig. (2.11) The time evolution of charges inside the quantum well of the double barrier structure of chapter two as a function of wave packet's central incident energy with a wave packet's spatial width of 1200-Å......45

Chapter 3

Fig. (3.1) A schematic illustration of a double quantum well structure showing the difference in the excitation energies of the two wells. This difference allows the ability to selectively photoexcite the wider well by the proper choice of the excitation energy 56

Fig. (3.2) Schematic illustration of wave function and tunneling processes of electrons associated mainly with the wide quantum well in a coupled well structure under three respective conditions. (a), (b), and (c) correspond, respectively, to "below" resonance, on resonance and "above" resonance

Reproduced with permission of the copyright owner. Further reproduction prohibited without permission.

conditions, where the energy level associated with the wide well is lower than, equal, and higher than that of the narrow well 57

Fig. (3.3) Selective photoexcitation of an electron wave packet in the wider well of a double quantum well structure. At resonance the wave packet will oscillate between the two wells. The width of the wide (narrow) well is 170 (120)-Å and the barrier is 17-Å with a height of 300 meV....58

Fig. (3.4) Normalized charge inside the narrow well as a function of time. The solid (dotted) line is the charge oscillation without (with) the Coulomb interaction 59

Fig. (3.5) Energy level in a coupled quantum well structure without (solid) and with (dotted) Coulomb interaction....60

Chapter 4

Fig. (4.1) (a) The LO- phonon ω-q dispersion relation, (b) The electron-phonon scattering matrix as a function of phonon wave numbers....80

Fig. (4.2) Tunneling current components in a double barrier structure in the presence of electron-phonon interaction. The double barrier structure consists of a 45-Å quantum well and two 28-Å barriers of 280 meV potential....81

Reproduced with permission of the copyright owner. Further reproduction prohibited without permission.

Fig. (4.3) Temporal behavior of the 1D resonant tunneling current density for the different conditions: (i) the solid curve for coupling constant g=0.0, (ii) the dotted curve for g=0.1 and T=300K, and (iii) the dashed curve for g=0.1 and T=0K..............................82

Fig. (4.4) The temperature dependence of the tunneling current density peak ratio *J(K)/J(10K)*. The solid curve is calculated by the model described in the text. The solid circles indicate the experimental data......83

Chapter 5

Fig. (5.1) The spatial dependence of the localized phonon modes electrostatic potential. Solid curve represent the interface antisymmetric phonon modes. The dashed (dotted) represent the interface symmetric (confined) phonon modes...99

Fig. (5.2) The temporal development of the charges inside the quantum well of a double barrier structure. The solid curve is for no electron-phonon interaction. The dashed, dot-dashed, and dotted curves belong to electrons interacting with interface antisymmetric, interface symmetric, and confined phonons, respectively...100

Fig. (5.3) The phonon assisted charge build-up due to confined phonon modes at room temperature. The solid (dashed) curve is when the electron wave packet is

Reproduced with permission of the copyright owner. Further reproduction prohibited without permission.

incident at one phonon energy above the resonant energy (at one phonon energy below the resonant energy).....101

Fig. (5.4) The maximum value of the electron-phonon coupling constant g(z) as a function of the quantum well width. The solid, dashed, and dot-dashed curves are for confined, interface symmetric, and interface antisymmetric phonon modes, respectively.....102

Chapter 6

Fig. (6.1) A schematic diagram of a p-n junction showing the energy band scheme as a function of position in the junction. Photons irradiate the material results in extra carriers in the conduction band and a flow of current.....119

Fig. (6.2) A schematic representation of the intrinsic losses associated with single band gap solar cell structures. These losses can be eliminated by using MQW solar cell structures.....120

Fig. (6.3) A schematic diagram of the intrinsic MQW region of a solar cell structure, quantum wells change in width to cover different absorption bands. Barrier widths are fixed at 20-Å, (a) Schematic p-i-n, (b) under flat band conditions, (c) under resonant conditions.....121

Reproduced with permission of the copyright owner. Further reproduction prohibited without permission.

Fig. (6.4) (a) The reverse biasing conditions. Barrier potential increases and the current will decrease. (b) The forward biasing conditions. The potential barrier will decrease resulting in a current increase. (c) The equivalent circuit of an illuminated p-n junction photovoltiac solar cell 122

Fig. (6.5) The temporal profiles of the short circuit current density reaching the collector side of the solar cell. Each curve is marked by the barrier height of the MQW structure used 123

Fig. (6.6) The MQW solar cell current density at maximum power along with output voltage at maximum power for InAs/GaInAs and GaAs/AlGaAs based MQW structures 124

Fig. (6.7) The energy efficiency of InAs/GaInAs and GaAs/AlGaAs MQW based solar cell structures 125

Fig. (6.8) The photon density of the solar spectrum as a function of wave numbers 126

Fig. (6.9) A schematic representation of the MQW solar cell structure. The scheme for covering the major solar cell spectrum is shown. Under resonant conditions, energy levels will couple and carrier collection will be achieved via resonant tunneling 127

Reproduced with permission of the copyright owner. Further reproduction prohibited without permission.

CHAPTER ONE

INTRODUCTION

1.1 Background

The concept of electron tunneling and its experimental manifestation can be considered as one of the early triumphs of the Schrödinger wave mechanics. The first application of the concept was made in 1928 by Oppenheimer[1] to describe the autoionization of the excited states of atomic hydrogen in a strong electric field. The idea of tunneling was used for the calculation of free electron emission in a metal into vacuum by Fowler and Nordhiem[2] in 1928. Frankel[3] quickly extended this calculation to the case of metal-vacuum-metal junction in which a net current flows when the potential of one electrode is different than the other.

In 1930, Frankel discussed the electron tunneling in metal-vacuum-semiconductor junctions, but at that time the quantum theory of electronic states in semiconductors had not been formulated. Therefore, he could not give a quantitative analysis of this tunneling process. The advent of quantum theory of semiconductors in 1931 permitted the two generalizations of Frankl's calculation. The first was the analysis of metal-insulator-semiconductor junction and the second was the metal-insulator-metal junction.

Reproduced with permission of the copyright owner. Further reproduction prohibited without permission.

The most convincing experimental evidence for the electron tunneling in solid was given by Esaki[4] in a semiconductor p-n diode in 1957. The trick to observe the electron tunneling in this diode was that both the n and p sides were heavily doped so that the depletion layer thickness was very *thin*, enough to have detectable tunneling current. Esaki used a very narrow germanium p-n junction with a depletion length of about 150-Å and doping densities in both sides of the junction of about 10^{19} cm^{-3}. An I-V curve for Esaki diode is shown in Fig. (1.1). Note, the maximum in the current curves at about 0.035 volt. In the range over 0.3 volt the current-voltage curve follow quantitatively the familiar p-n junction diode equation $I = I_o[exp(qV/kT) - 1]$.

With advances in thin film preparation and developments in epitaxial growth techniques such as molecular beam epitaxy (MBE) and metal-organic chemical vapor deposition (MOVCD), ultra thin hetrolayers can be readily fabricated nowadays. It is now possible to create potential profiles consisting of barriers and wells with a monolayer (2-5 Å) thickness resolution. In structures composed of quantum wells and barriers, the carriers are confined to thin semiconductor layers. When the layer thickness approaches the Bohr radius, the electronic system enters the quantum regime and the material exhibits modified electrical and optical properties as compared to bulk material like the step like density of states and structure dependent energy spectrum of allowed states

To illustrate the concept of electron tunneling, consider a one-dimensional barrier structure shown in Fig. 1.1a. The potential is 0 for $x < -a, x > a$, and is V for $-a \le x \le a$. The incident electron wave comes

Reproduced with permission of the copyright owner. Further reproduction prohibited without permission.

from $x=-\infty$. To construct the wave function $\psi(x)$ we divide the x axis into three domains: region I, region II, and region III, depicted in Fig. 1.1a. The time-independent Schrödinger equation can be written as:

$$-\frac{\hbar^2}{2m^*}\psi''+v(x)=E\psi, \tag{1.1}$$

where ψ'' is the wave function second derivative with respect to the space coordinate x. The energy E is the eigen energy. In region I, Schrödinger equation appears as:

$$-\frac{\hbar^2}{2m^*}\psi''=E\psi. \tag{1.2}$$

In this domain the energy is entirely kinetic. If we set $\frac{\hbar^2 k_1^2}{2m^*}=E$ then Eq. (1.2) becomes:

$$\psi''=-k_1^2\psi. \tag{1.3}$$

In region II, the potential is V and the Schrödinger equation appears as:

$$-\frac{\hbar^2}{2m^*}\psi''=(E-V)\psi. \tag{1.4}$$

The eigen energy decreases by V and is given by $\frac{\hbar^2 k_2^2}{2m^*}=E-V$. In terms of k_2, the Schrödinger equation appears as:

$$\psi''=-k_2^2\psi. \tag{1.5}$$

In region III, the conditions are exactly as in region I, the solution for the wave function in the different regions can be written as:

Reproduced with permission of the copyright owner. Further reproduction prohibited without permission.

$$\begin{aligned}\psi_I(x) &= Ae^{ik_1x} + Be^{-ik_1x} \\ \psi_{II}(x) &= Ce^{ik_2x} + De^{-ik_2x} \\ \psi_{III}(x) &= Fe^{ik_1x} + Ge^{-ik_1x}\end{aligned} \tag{1.6}$$

Since the term Ge^{-ik_1x} represent a wave emerging from the right ($x=+\infty$ in Fig. 1.2a), and there is no such wave, we conclude that G=0. The interpretation of the remaining *A, B, C, D,* and *F* terms in the wave function equation is given as follows: Ae^{ik_1x} represent the incident wave, Be^{-ik_1x} represent the reflected wave, Ce^{ik_2x} represent the part of the incident wave that tunneled into the barrier region, De^{-ik_2x} represent the reflected wave part from the inside the barrier, and Fe^{ik_1x} represent the transmitted wave.

For the case of $E < V$, the following modification applies:

$$ik_2 \to \kappa, \qquad \frac{\hbar^2\kappa^2}{2m^*} = V - E > 0. \tag{1.7}$$

In Fig. 1.2b, the wave functions in each region are plotted. Note the wave function inside the barrier region is simply a decaying wave. Matching the wave functions and their derivatives at the interfaces ($-a$, and a) the transmission coefficient can be written as:

$$T = \left|\frac{F}{A}\right|^2 = \frac{1}{1+\dfrac{1}{4}\dfrac{V^2}{E(E-V)}\sinh^2(2\kappa a)}, \quad E < V \tag{1.8}$$

Fig. 1.2c displays the transmission coefficient versus the E/V. Three salient features can be observed in this figure. First, the probability of transmission is only about 20% even when the incident electron energy matches the barrier potential. Second, the oscillation that appear on the

Reproduced with permission of the copyright owner. Further reproduction prohibited without permission.

transmission curve for $E/V > 1.5$, which is due to what is known as above the barrier resonant states. Third, note the exponential like behavior of the transmission probability as a function of incident energy.

The concept of resonant tunneling refers to the process of an enhancement of electron tunneling by an intermediate energy state. The simplest case is that of a single potential well sandwiched between two potential barriers. The current flows between two outside electrodes through the structure, and resonance occurs when the incoming electrons coincide in energy with the quantum states created in the well. The current-voltage characteristics of a tunneling diode is illustrated in Fig. 1.3a. The current rises as the energy separation between electron wave packet in the emitting electrode and the quantum state in the quantum well decreases by increasing the applied voltage (Fig. 1.3b,c). As the applied voltage increases further, the quantum state in the quantum well will be aligned in energy with the electron's wave packet energy and the current reaches a maximum (Fig. 1.3d). With more applied voltage, the quantum state passes below the wave packet's incident resulting in breaking the resonance condition which in turn leads to a reduction in the tunneling probability and the tunneling current as well as shown in Fig. 1.3e. The current rises again with the increase in applied voltage as the incident energy becomes closer to the top of the barrier where the tunneling probability increases. Indeed, the first observation of resonant tunneling was made in a double barrier structure consisting of GaAs-GaAlAs[5] in 1974. This experiment served as the first demonstration that prescribed, man-made quantum states can be formed in ultra thin semiconductor heterostructures.

Reproduced with permission of the copyright owner. Further reproduction prohibited without permission.

There are many applications of resonant tunneling processes in semiconductor engineered structures such as high frequency microwave oscillators[6] where frequencies up to 712 GHz at room temperature were reported using InAs/AlSb resonant tunneling diodes (RTDs). Oscillation in the RTDs are achievable when the tunneling diode is biased in the negative differential resistance region. Tunable photodetectors[7] which are realized by incorporating a superlattice or a multiple quantum well structure in the undoped region of a p-i-n structure. Tunability is achieved by changing the applied voltage across the structure which results in changing the separation between quantum states and as a result the operating wavelength will change. Quantum well solar cells[8] is another application which I will elaborate on in chapter six. Therefore, understanding the resonant tunneling process is of technological importance.

Although an extensive amount of work has been done aiming at understanding the process of electron tunneling, little is known about the fundamental dynamics of this process. Tunneling is usually considered an extremely fast process. The time it takes for electrons to tunnel through a barrier (which is usually known to as the tunneling time) can be much faster than a picosecond in typical cases. In a double barrier structure, the life time of the quasi bound states is the crucial parameter, which is expected to be related to the accumulation and escape of carriers in the quantum well. There still remains many questions need to be answered: (1) what are the various characteristic times associated with the tunneling process such as the charge build-up time in the quantum well of a double barrier structure? (2) how does

Reproduced with permission of the copyright owner. Further reproduction prohibited without permission.

electron-hole interaction affect electron tunneling between coupled double quantum wells? (3) in what way do the electron-phonon and electron-photon interaction affect the electron tunneling process? and (4) how to enhance the solar cell efficiency through quantum well electron resonant tunneling.

The work of this thesis focuses on the dynamical nature of electron resonant tunneling process in semiconductor nanostructures attempting to find answers to the above questions.

1.2 Thesis Statement

In this thesis electron tunneling dynamics in the presence of electron-phonon and electron-hole interaction in semiconductor nanostructures were investigated theoretically by numerically solving the time-dependent Schrödinger equation.

The specific tasks that were accomplished in this thesis as published in the literature[9] are:

(1) The time-dependent charge build-up inside the quantum well of a double barrier structure.[9a]

(2) The excitonic effects on the coherent oscillation of photoexcited charges between coupled double quantum wells.[9b,c]

(3) Effect of electron-phonon interaction on the electron tunneling current density in a double barrier structure.[9d]

(4) The effect of localized phonon modes on the charge build-up inside the quantum well of a double barrier structure.[9e]

Reproduced with permission of the copyright owner. Further reproduction prohibited without permission.

(5) The proper design and engineering of barrier potential for efficient multiple quantum well based solar cells structures.[9f]

1.3 Thesis Organization

This thesis is organized into eight chapters including the introduction chapter

In chapter 2, the detailed numerical procedure for solving the time-dependent Schrödinger equation is presented. This procedure is then used to explore the temporal characteristics of charge build-up in the quantum well of a double barrier structure as a function of the incident electron's wave packet central energy. Specific features of charge build-up inside the quantum well such as the time needed for the resonance to take place, the shifting of the resonance peak as a function of time, and the charge decay time inside the quantum well were all detailed .

In chapter 3, I investigated the coherent oscillation of photoexcited charges between two coupled quantum wells at the resonance conditions and results were compared with available experimental data. The effect of electron-hole interaction on the oscillation period was also investigated.

The time-dependent electron tunneling current through a double barrier structure at resonance conditions was calculated in chapter 4. The effect of electron-phonon interaction on the tunneling current density was addressed in the presence of plane wave LO phonons. Results were compared with available experimental data.

Reproduced with permission of the copyright owner. Further reproduction prohibited without permission.

Chapter 5 is an extension of chapter 4, where I addressed the effect of localized phonon modes such as confined modes in the quantum well, symmetric, and antisymmetric phonon modes on the tunneling current density through the double barrier structure.

The proper design criteria for multiple quantum well based solar cell structures was presented in chapter 6. The effect of tunneling current density on the solar cell energy efficiency was discussed. Specific design criteria and specific multiple quantum well materials and structures were given.

The final two chapters of the thesis summarizes the achievements of my research and future research to advance the use of electron tunneling in high technology devices.

Reproduced with permission of the copyright owner. Further reproduction prohibited without permission.

1.4. References

1. J. R. Oppenheimer, Phys. Rev. **31**, 66 (1928).
2. R. H. Fowler and L. Nordheim, Proc. Roy. Soc. (London), **A119**, 173 (1928).
3. J. Frenkel, Phys. Rev. **36**, 1604 (1930).
4. L. Esaki, Phys. Rev. **109**, 603 (1957).
5. L. Esaki, and L. L. Chang, Phys. Rev. Lett. **33**, 495 (1974).
6. E. R. Brown, J. R. Soderstrom, C. D. Parker, L. J. Mahoney, K. M. Mplvar, and T. C. McGill, Appl. Phys. Lett. **58**, 2291 (1991).
7. A. Larsson, P. A. Andrekson, S. T. Eng, and A. Yariv, IEEE, **24**, 787 (1988).
8. K. W. J. Barnham and G. Duggan, J. Appl. Phys. **67**, 3490 (1990).
9. Publications relative to thesis

9a. Jihad M. Mohaidat, Kai Shum, and R. R. Alfano, submitted for publication in Phys. Rev. B

9b. Jihad M. Mohaidat, Kai Shum, and R. R. Alfano, Phys. Rev. B, **45**, 3822 (1992).

9c. Jihad M. Mohaidat, Kai Shum, and R. R. Alfano, SPIE *Proceedings,* Vol. 1677 (1992).

9d. Jihad M. Mohaidat, Kai Shum, and R. R. Alfano, Phys. Rev. B, **48**, 8809 (1993).

9e. Jihad M. Mohaidat, Kai Shum, and R. R. Alfano, submitted for publication in *Solid State Communication.*

Reproduced with permission of the copyright owner. Further reproduction prohibited without permission.

9f. Jihad M. Mohaidat, Kai Shum, W. B. Wang, and R. R. Alfano, submitted for publication in Phys. Rev. B.

Reproduced with permission of the copyright owner. Further reproduction prohibited without permission.

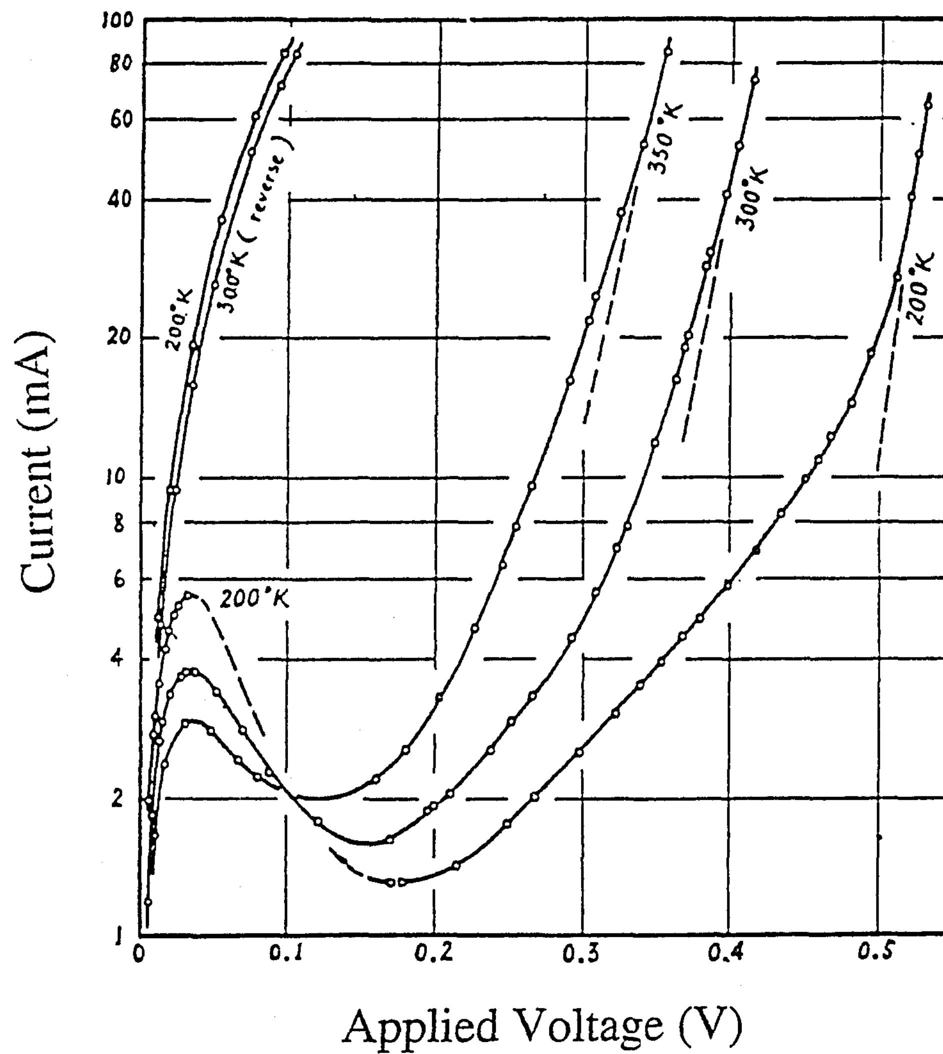

Fig. 1.1 A semilog plot of the measured current voltage characterstics of Esaki diode at 200K, 300K, and 400K. (After Esaki, Phys. Rev. 109, 603 (1957))

Reproduced with permission of the copyright owner. Further reproduction prohibited without permission.

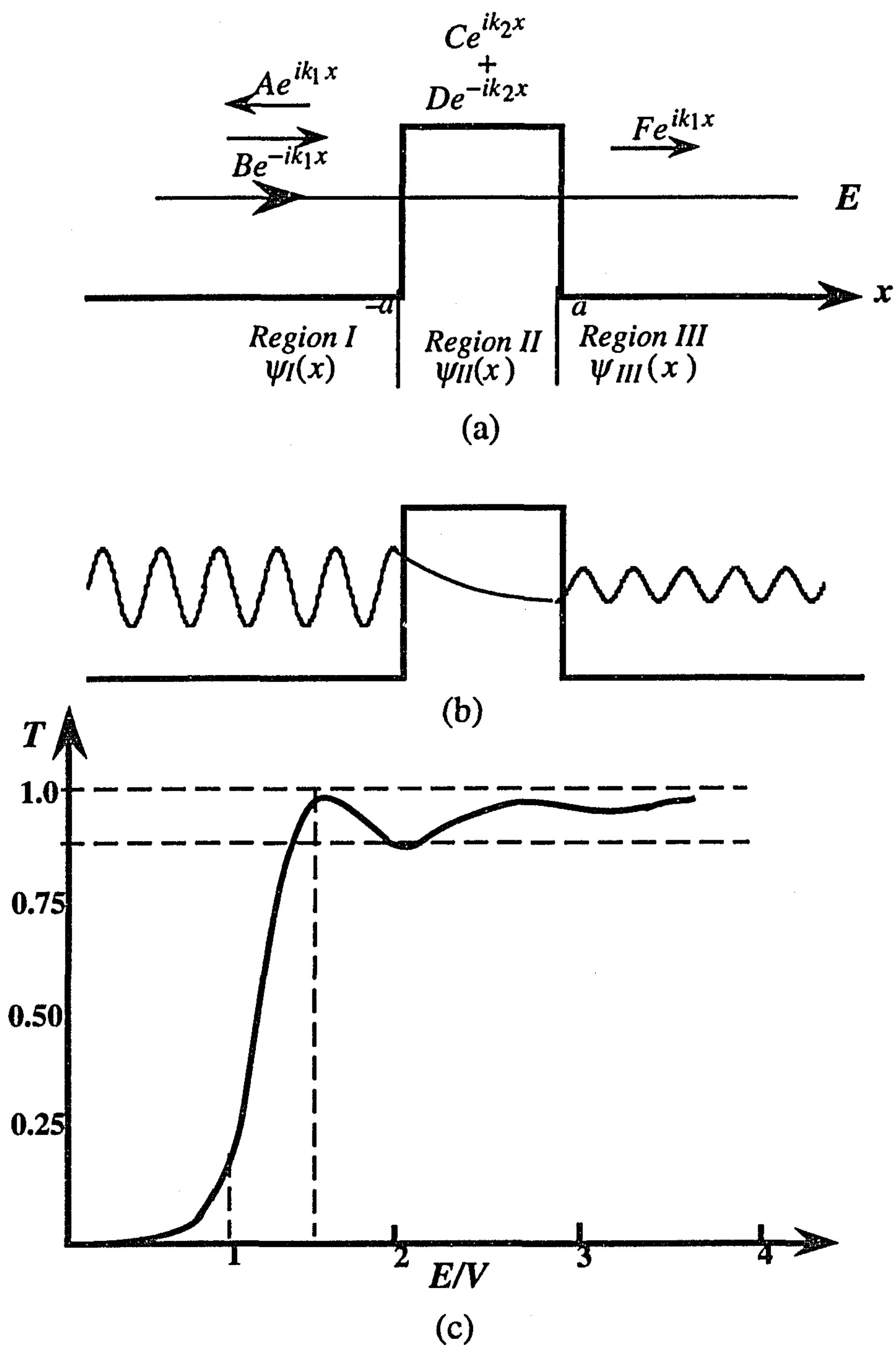

Fig.1.2 (a) Domains relevant to the single barrier tunneling structure for $E<V$. (b)The wave function in the different domains, showing the decay of the wave function inside the barrier region and decrease in amplitude of the transmitted wave. (c) Transmission Coefficient T versus E/V.

Reproduced with permission of the copyright owner. Further reproduction prohibited without permission.

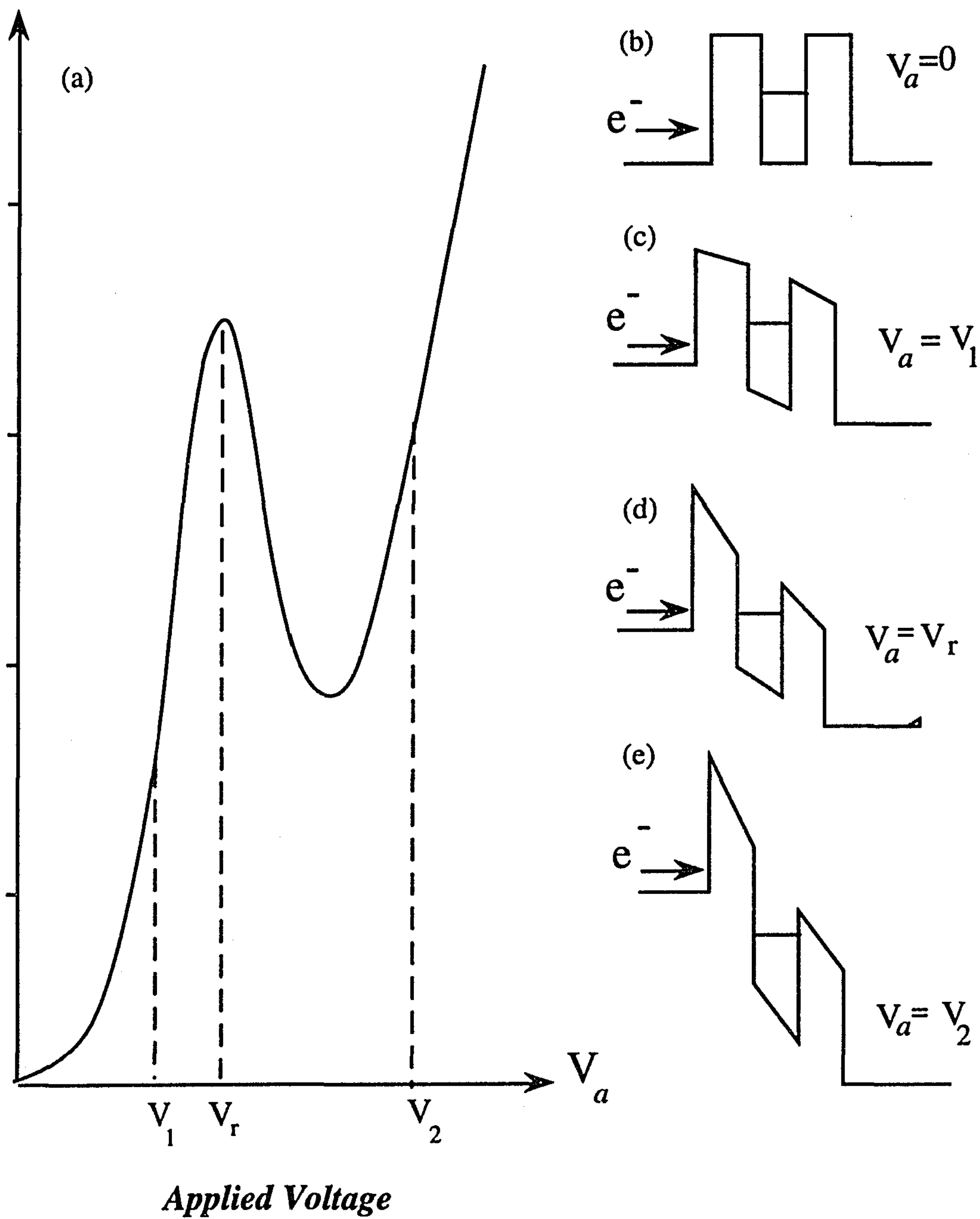

Fig.1.3 Current Voltage characteristic of a double barrier resonant tunneling diode. The position of the quasi bound state with respect to the incoming electron energy at different applied voltage is also shown.

Reproduced with permission of the copyright owner. Further reproduction prohibited without permission.

CHAPTER TWO

DYNAMICS OF A TRAVELING ELECTRON WAVE PACKET IN A DOUBLE BARRIER STRUCTURE

2.1 Introduction

The dynamics of an electron wave packet tunneling through a semiconductor double barrier quantum-well structure has been of interest since the seminal work of Tsu and Esaki[1] where using a GaAs/AlGaAs structure they demonstrate not only formation of quantum states but their manifestation in controlling the transport properties. Gou *et al*[2] studied the time the charge needs to reach the peak inside the quantum well of a double barrier structure when the wave packet is incident at the resonant energy. Juaho et al[3,4] presented numerical simulations of wave packets of different shapes tunneling through a static and time modulated barrier in an attempt to cast light on tunneling times. They conclude that the wave packet shape is unimportant in determining the tunneling time. Collins[5] showed that the tunneling time through a double barrier structure is primarily controlled by the energy width of the quasi bound states. See also references 6 through 9 for more work. In this chapter, the temporal behavior of a traveling electron wave packet initiated in the left lead of a double barrier structure as a function of the wave packet's central

Reproduced with permission of the copyright owner. Further reproduction prohibited without permission.

incident energy are investigated. Some of the conclusions from this investigation are:

- the tunneling probability or equivalently charge build up enhancement due to the double barrier quantum well resonance states is *not* reflected in the spectral profile of the charge build-up inside the quantum well during the early time period 0-40 fs.
- the charge build-up enhancement due to the resonance states starts developing as time passes 40 fs and appear initially to be *blue-shifted* from the energy position calculated using the time-independent Schrödinger equation by as much as 26 meV.
- the Full Width at Half Maximum (FWHM) of the charge build-up temporal profiles as a function of packet central incident energy starts to be large and decreases as time increases.

These observations can be explained by taking into account the energy spread of the traveling wave packet relative to the energy position of the resonant states. In the next section, I will detail the procedure for the numerical solution of the time-dependent Schrödinger equation. In section 2.3, I will apply this method to study the dynamics of an electron wave packet traveling through a double barrier structure.

2.2 Theory

Our simulations throughout this research are based on the numerical solution of the time-dependent Schrödinger equation.

Reproduced with permission of the copyright owner. Further reproduction prohibited without permission.

Within the framework of the effective-mass approximation, the evolution of a one-dimensional envelope wave function $\psi(z,t)$ is determined by the time-dependent Schrödinger equation:

$$H\psi(z,t) = i\hbar \frac{\partial}{\partial t}\psi(z,t), \tag{2.1}$$

where H is the Hamiltonian operator associated with the system. A standard procedure for solving this equation is in terms of the stationary states of the Hamiltonian H. If we have $Hu_m = E_m u_m$ for the bound states and $Hu_k = E(k)u_k$ for the continuum states, then a formal solution to the problem is given by:

$$\psi(z,t) = \sum_m a_m e^{-itE_m/\hbar} u_m(z) + \int a(k) e^{-iE(k)t} u_k(z), \tag{2.2}$$

with

$$a_m = \langle u_m | \psi(z,0) \rangle \tag{2.3}$$

and

$$a(k) = \langle u_k | \psi(z,0) \rangle \tag{2.4}$$

where $\psi(z,0)$ is the *given* initial state of the system. This procedure was not adopted here for several reasons: (i) for almost all potentials the eigenfunctions and their eigenvalues have to be determined numerically, (ii) even with all the eigenfunctions and eigenvalues known or evaluated, the computation of the terms comprising equation (2.2) at each t and z of interest is a lengthy task, and (iii) we should have to restrict the initial state of the system $\psi(z,0)$, to some limited combination of eigenstates or be forced to carry out the many numerical

Reproduced with permission of the copyright owner. Further reproduction prohibited without permission.

integrations required to evaluate the coefficients a_m and $a(k)$ given by Eq. (2.3) and Eq. (2.4) and required by Eq. (2.2).

To avoid these problems I have found it more convenient to deal directly with Eq. (2.1). In dealing with equation (2.1), we convert it from a differential equation into a finite difference equation in both space and time, a procedure which is described in detail later in this section.

The one-dimensional system Hamiltonian H that appears in the above equations and been used in the literature can assume one of the following forms:[10,11]

1) The conventional operator:

$$H_1 = \frac{-\hbar^2}{2m^*}\frac{\partial^2}{\partial z^2} + V(z), \tag{2.5}$$

2) Ben Daniel and Duke Hamiltonian:

$$H_2 = -\frac{\hbar^2}{2}\frac{\partial}{\partial z}\left(\frac{1}{m^*(z)}\frac{\partial}{\partial z}\right) + V(z), \tag{2.6}$$

or

3)Bastard Hamiltonian:

$$H_3 = -\frac{\hbar^2}{4}\left(\frac{1}{m^*(z)}\frac{\partial^2}{\partial z^2} + \frac{\partial^2}{\partial z^2}\frac{1}{m^*(z)}\right) + V(z), \tag{2.7}$$

where $m^*(z)$ is the position-dependent effective mass. The potential $V(z)$ is the potential associated with the particular system under consideration.

Reproduced with permission of the copyright owner. Further reproduction prohibited without permission.

The presence of different models for the Hamiltonian is due to quantum mechanical problems associated with them which I will outline below. Other version were suggested to overcome these problems.

It is found[11] that when the conventional Hamiltonian H_1 is used, the wave function is smooth at the interfaces. However, this wave function does not satisfy the unitarity conditions, that is $\langle \psi_m | \psi_m \rangle$ is different from unity. As a result, the total energy E_m is no longer conserved. This suggests that the conventional Hamiltonian is inappropriate to describe a heterojunction such as a double barrier structure. When Bastard Hamiltonian H_3 is applied, discontinuities in the wave function at the heterojunction interfaces were found. This also suggest that Bastard Hamiltonian is inappropriate as well by not maintaining the wave function continuity. When Ben Daniel and Duke's Hamiltonian is used, the wave function is found to be continuous at the interfaces. More importantly, the unitarity condition $\langle \psi_m | \psi_m \rangle$ is satisfied and the total energy remains constant. Based on these observations, I adopted the Ben Daniel and Duke Hamiltonian throughout this thesis work.

Using the Ben-Daniel and Duke's Hamiltonian, the time-dependent Schrödinger equation then appears as follows:

$$\begin{aligned} i\hbar \frac{\partial}{\partial t} \psi(z,t) &= H_2 \psi(z,t) \\ &= -\frac{\hbar^2}{2} \frac{\partial}{\partial z} \left(\frac{1}{m^*(z)} \frac{\partial}{\partial z} \right) \psi(z,t) + V(z) \psi(z,t), \end{aligned} \tag{2.8}$$

Reproduced with permission of the copyright owner. Further reproduction prohibited without permission.

Using a standard differencing technique, the finite difference equation for $H_2\psi(z,t)$ can be written in the following format:

$$H_2\psi_j = -\frac{\hbar^2}{\varepsilon^2}\left(\frac{\psi_{j+1}}{m_{j+1}^* + m_j^*} + \frac{\psi_{j-1}}{m_{j-1}^* + m_j^*} - \right.$$
$$\left. - \frac{\psi_j}{m_{j+1}^* + m_j^*} - \frac{\psi_j}{m_{j-1}^* + m_j^*}\right) + V_j\psi_j, \tag{2.9}$$

where ε and j are the space interval and index, respectively. Note that the effective mass has been differentiated with respect to the space coordinate in Eq.(2.9).

To treat the time development of ψ, we note that the formal solution of Eq. (2.2) is given by:

$$\psi(z,t) = e^{-itH}\psi(z,0) \tag{2.10}$$

where the exponential factor is defined in terms of Taylor's series:

$$e^{-itH} = \sum_{k=0}^{\infty} \frac{[-it]^k}{k!} H^k. \tag{2.11}$$

From Eq. (2.10) we have

$$\psi_j^{n+1} = e^{-i\delta H}\psi_j^n \tag{2.12}$$

where δ and n are the time interval and index, respectively. The above equation, correct to terms of order δ, becomes:

Reproduced with permission of the copyright owner. Further reproduction prohibited without permission.

$$\psi_j^{n+1} = (1 - i\delta H)\psi_j^n = \psi_j^n - i\delta H\psi_j^n. \tag{2.13}$$

substituting for $H\psi_j^n$ from Eq. (2.9) into the above equation results in:

$$\psi_j^{n+1} = \psi_j^n - i\delta\left[\frac{-\hbar^2}{\varepsilon^2}\left(\frac{\psi_{j+1}^n}{m_{j+1}^* + m_j^*} + \frac{\psi_{j-1}^n}{m_{j+1}^* + m_j^*} - \frac{\psi_j^n}{m_{j+1}^* + m_j^*} - \frac{\psi_j^n}{m_{j-1}^* + m_j^*}\right) + V_j\psi_j^n\right] \tag{2.14}$$

rearranging and collecting terms, Eq. (2.14) can be written as:

$$\psi_j^{n+1} = \frac{1}{m_{j+1}^* + m_j^*}\frac{i\delta\hbar^2}{\varepsilon^2}\cdot\psi_{j+1}^n + \left\{1 - \frac{i\delta\hbar^2}{\varepsilon^2}\left(\frac{1}{m_{j+1}^* + m_j^*} - \frac{1}{m_{j-1}^* + m_j^*}\right) - i\delta V_j\right\}\psi_j^n. + \frac{i\delta\hbar^2}{\varepsilon^2}\frac{1}{m_{j-1}^* + m_j^*}\psi_{j-1}^n \tag{2.15}$$

One feature of this equation is especially attractive: it is an *explicit* differencing scheme, i.e. one which gives the wave function at time step $n+1$ directly in terms of the wave function at early time n. Clearly this permits a straightforward integration scheme and allows for an easy determination of the wave function for all n and all j. The scheme, however, has a very serious drawback of being numerically unstable; that is to say errors can grow without bounds as the time of integration proceeds from step to step.

A procedure which eliminates this instability involves rewriting Eq. (2.12) in the form:

Reproduced with permission of the copyright owner. Further reproduction prohibited without permission.

$$\psi_j^n = e^{i\delta H}\psi_j^{n+1}, \tag{2.16}$$

which leads to a difference equation that is *implicit,* rather than explicit. By this I mean the wave function at time $n+1$ is *not* directly determined by the wave function at the early time n and certain algebraic techniques must be applied in order to obtain the wave function at time $n+1$. Unfortunately, the implicit deference equation resulting from the use of Eq. (2.16) must be ruled out based on the grounds that it is not *unitary.*

Unitarity is the characteristic of the original wave equation which insures that the normalization of the wave function does not change in time. The operators $e^{\pm i\delta H}$ are unitary. However, no approximation of these operators which involves expanding the exponential and retaining only a finite number of terms is unitary. In particular, the first order approximation $1 \pm i\delta H$, are not unitary. A relatively simple unitary approximation to $e^{-i\delta H}$ is, however, provided by the Cayley form:

$$e^{-i\delta H} \cong \left(1-\frac{1}{2}i\delta H\right)\Big/\left(1+\frac{1}{2}i\delta H\right). \tag{2.17}$$

Let me then replace $e^{-i\delta H}$ in Eq. (2.12) by the Cayley form to get:

$$\psi_j^{n+1} = \left[\left(1-\frac{1}{2}i\delta H\right)\Big/\left(1+\frac{1}{2}i\delta H\right)\right]\psi_j^n. \tag{2.18}$$

which can be also written in the following format:

$$\left[1+\tfrac{1}{2}i\delta H\right]\psi_j^{n+1} = \left[1-\tfrac{1}{2}i\delta H\right]\psi_j^n \tag{2.19}$$

Reproduced with permission of the copyright owner. Further reproduction prohibited without permission.

or

$$\psi_j^{n+1} + \tfrac{1}{2} i\delta H \psi_j^{n+1} = \psi_j^n - \tfrac{1}{2} i\delta H \psi_j^n \tag{2.20}$$

substituting for $H\psi_j^{n+1}$ and $H\psi_j^n$ from Eq. (2.9) leads to:

$$\begin{aligned}
&\psi_j^{n+1} + \tfrac{1}{2} i\delta \left[\frac{-\hbar^2}{\varepsilon^2} \left(\frac{\psi_{j+1}^{n+1}}{m_{j+1}^* + m_j^*} + \frac{\psi_{j-1}^{n+1}}{m_{j-1}^* + m_j^*} \right.\right. \\
&\left.\left. - \frac{\psi_j^{n+1}}{m_{j+1}^* + m_j^*} - \frac{\psi_j^{n+1}}{m_{j-1}^* + m_j^*} \right) + V_j \psi_j^{n+1} \right] = \\
&\psi_j^n + \tfrac{1}{2} i\delta \left[\frac{-\hbar^2}{\varepsilon^2} \left(\frac{\psi_{j+1}^n}{m_{j+1}^* + m_j^*} + \frac{\psi_{j-1}^n}{m_{j-1}^* + m_j^*} \right.\right. \\
&\left.\left. - \frac{\psi_j^n}{m_{j+1}^* + m_j^*} - \frac{\psi_j^n}{m_{j-1}^* + m_j^*} \right) + V_j \psi_j^n \right]
\end{aligned} \tag{2.21}$$

which in turn can be written as follows:

$$\begin{aligned}
&\frac{\psi_{j+1}^{n+1}}{m_{j+1}^* + m_j^*} + \left(\frac{2\varepsilon^2}{\hbar\delta} i - \frac{\varepsilon^2}{\hbar^2} V_j - \frac{1}{m_{j+1}^* + m_j^*} - \frac{1}{m_{j-1}^* + m_j^*} \right) \psi_j^{n+1} + \\
&\frac{\psi_{j-1}^{n+1}}{m_{j+1}^* + m_j^*} + \frac{\psi_{j+1}^{n-1}}{m_{j+1}^* + m_j^*} - \\
&\left(\frac{2\varepsilon^2}{\hbar\delta} i + \frac{\varepsilon^2}{\hbar^2} V_j + \frac{1}{m_{j+1}^* + m_j^*} + \frac{1}{m_{j-1}^* + m_j^*} \right) \psi_j^n + \frac{\psi_{j-1}^n}{m_{j-1}^* + m_j^*} = 0
\end{aligned} \tag{2.22}$$

This difference equation (Eq. (2.22) can be written in the matrix format $Ax = b$ with A being a complex tridiagonal complex matrix. A solution for this equation was given by Goldberg[12] which is rather tedious and requires a huge amount of computer memory. The method

Reproduced with permission of the copyright owner. Further reproduction prohibited without permission.

that was used in my work reduces the time of computations and computer memory requirements tremendously.

To illustrate the method of solution, let me rewrite Eq. (2.22) at a particular time $(n+1)$ in the following format:

$$a(j)\psi_{j-1} + b(j)\psi_j + c(j)\psi_{j+1} = d(j) \tag{2.23}$$

expanding the above equation:

$$\begin{aligned}
&b_1\psi_1 + c_1\psi_2 &&= d_1 \\
&a_2\psi_1 + b_2\psi_2 + c_2\psi_3 &&= d_2 \\
&\quad a_3\psi_2 + b_3\psi_3 + c_3\psi_4 &&= d_3 \\
&\quad\cdots\cdots\cdots\cdots\cdots\cdots && \\
&\qquad a_i\psi_{i-1} + b_i\psi_i + c_i\psi_{i+1} &&= d_i \\
&\qquad\cdots\cdots\cdots\cdots\cdots\cdots\cdots\cdots && \\
&\qquad\qquad a_{N-1}\psi_{N-2} + b_{N-1}\psi_{N-1} + c_{N-1}\psi_N &&= d_{N-1} \\
&\qquad\qquad\qquad a_N\psi_{N-1} + b_N\psi_N &&= d_N
\end{aligned} \tag{2.24}$$

where the $d_1, d_2, \ldots d_N$ are known quantities at time n where at n=0, the *d's* are represented by the initial condition of the system. N runs over all the space of the problem. In writing the above equation, I used zero boundary conditions at both sides of the space over which the structure extends. The coefficients *a, b,* and *c* can be acquired directly from Eq. (2.22). The matrix with coefficients of *a, b,* and *c* alone is called a *tridiagonal* matrix. With three variables per equation, the solution can be expressed very concisely.

I first demonstrate the validity of a *recursion solution* of the form:

Reproduced with permission of the copyright owner. Further reproduction prohibited without permission.

$$\psi_i = \gamma_i - \frac{c_i}{\beta_i}\psi_{i+1}, \tag{2.25}$$

in which the constants β_i and γ_i are to be determined. Substitution into the *i*th equation of Eq. (2.24) gives:

$$a_i\left(\gamma_{i-1} - \frac{c_{i-1}}{\beta_{i-1}}\psi_i\right) + b_i\psi_i + c_i\psi_{i+1} = d_i. \tag{2.26}$$

That is,

$$\psi_i = \frac{d_i - a_i\gamma_{i-1}}{b_i - \dfrac{a_i c_{i-1}}{\beta_{i-1}}} - \frac{c_i\psi_{i+1}}{b_i - \dfrac{a_i c_{i-1}}{\beta_{i-1}}}, \tag{2.27}$$

which verifies the above form, subject to the following conditions:

$$\beta_i = b_i - \frac{a_i c_{i-1}}{\beta_{i-1}}, \tag{2.28a}$$

and

$$\gamma_i = \frac{d_i - a_i\gamma_{i-1}}{\beta_i}. \tag{2.28b}$$

Also, from the first equation of (2.24),

$$\psi_1 = \frac{d_1}{b_1} - \frac{c_1}{b_1}\psi_2, \tag{2.29}$$

where $\beta_1 = b_1$ and $\gamma_1 = {}^{d_1}\!/_{\beta_1}$. Finally, substitution of the recursion solution into the last equation of (2.24) yields:

Reproduced with permission of the copyright owner. Further reproduction prohibited without permission.

$$\psi_N = \frac{d_N - a_N \psi_{N-1}}{b_N} = \frac{d_N - a_N \left(\gamma_{i-1} - \frac{c_{N-1}}{\beta_{N-1}} \psi_N \right)}{b_N}, \tag{2.30}$$

hence,

$$\psi_N = \frac{d_N - a_N \gamma_{N-1}}{b_N - \frac{a_N c_{N-1}}{\beta_{N-1}}} = \gamma_N. \tag{2.31}$$

To summarize, the complete algorithm for the solution of the tridiagonal system is

$$\begin{aligned} &\psi_N = \gamma_N \\ &\psi_i = \gamma_i - \frac{c_i \psi_{i+1}}{\beta_i}, \qquad i = N, N-1, N-2, \ldots\ldots, 1, \end{aligned} \tag{2.32}$$

where the β's and γ's are determined from the recursion formulas:

$$\begin{aligned} &\beta_1 = b_1, \\ &\gamma_1 = \frac{d_1}{\beta_1}, \\ &\beta_i = b_i - \frac{a_i c_{i-1}}{\beta_{i-1}}, \qquad i = 2, 3, \ldots\ldots., N, \\ &\gamma_i = \frac{d_i - a_i \gamma_{i-1}}{\beta_i}, \qquad i = 2, 3, \ldots\ldots., N. \end{aligned} \tag{2.33}$$

Knowing the initial condition at time t=0, and using the above algorithm we can solve for the wave function at time n=1, then this can be used to evaluate the wave function for n=2, The process is repeated for n=3, 4, and so forth. Note that it is necessary to limit the time n of integration to a certain maximum such that the traveling packet will not

Reproduced with permission of the copyright owner. Further reproduction prohibited without permission.

hit the hard walls represented by the boundary conditions of the problem and bounce back causing errors in the computations.

The electric field, electron-hole, electron-phonon, and/or electron-photon effects can be treated as part of the potential term whether these effects are time-dependent or time-independent as we shall see in the subsequent chapters.

Now we turn to apply the above mentioned procedure to solve the time-dependent Schrödinger equation in studying the dynamics of a traveling electron wave packet in a double barrier structure potential as a function of the wave packet's central incident energy. A double barrier structure consisting of 60Å GaAs quantum well sandwiched by two 30Å AlGaAs barriers of 280 meV potential height was chosen as the potential profile which the electron wave packet is tunneling through. A schematic representation of the band diagram of this structure is shown in Fig. 2.1. This structure is chosen to contain two quasi-bound states.

An initial electron wave function $\psi(z,t=0)$ (from which the vector *d(j)* in Eqs. (2.23) and (2.24) can be evaluated) of the form:

$$\psi(z,t=0)=\exp(ik_{ci}z)\exp\left(-\frac{(z-z_0)^2}{4\sigma^2}\right), \tag{2.34}$$

was placed in the left lead of the double barrier structure and the solution of Schrödinger difference equation (Eq. (2.22)) was initiated. z_0 is the wave packet center location in the growth direction, k_{ci} is the central incident energy wave number of the wave packet and σ is the wave packet's spatial width. A value of $0.067\,m_0$ ($0.092\,m_0$) for electron

Reproduced with permission of the copyright owner. Further reproduction prohibited without permission.

effective mass was taken for GaAs (AlGaAs). A time mesh size[3] δ of 1fs, spatial mesh size[3] ε of 0.5Å, zero boundary conditions at the two end points 1μm away from the structure (Under the considered time scale, 1-μm distance away from the barriers is far enough to insure that the packet will not hit the boundary and bounce back to affect the calculations.), and a wave packet spatial width of 550Å where also used. Note that the space and time mesh sizes were chosen as above to insure the accuracy of the numerical technique. These values are used throughout the thesis work.

At time t=0 the initial electron wave packet was placed at the position 1450Å away from the double barrier structure in the left lead. Tunneling process is initiated at t=0. This wave packet simulates a photoexcitation by an ultrafast laser pulse. The development of the wave function in time inside the quantum well is followed as the wave packet moves into the structure.

The electronic charge inside the quantum well is calculated by:

$$q_w(t, E_{ci}) = e\int_0^d \psi^*(x,t)\,\psi(z,t)\,dz. \tag{2.35}$$

where d is the width of the quantum well. The electronic charge is taken to be unity. Here, I am treating a single particle or a single electron problem in which the charge inside the quantum well or the probability (the multiplication of the wave function and its complex conjugate represent a probability density function) of finding the electron inside the quantum well will reveal the same information.

Reproduced with permission of the copyright owner. Further reproduction prohibited without permission.

2.3 Results and discussion

Fig. 2.2 shows a 3-D plot for the charge build-up inside the quantum well as a function of time and wave packet's central incident energy (t, E_{ci}). It is clear that it takes about 200 fs for the charge to reach a maximum at the first excited quasi-bound state located at 244 meV, while it takes about 450 fs for the charge to reach a maximum at the ground quasi-bound state. After 200 fs, the charge at the first excited quasi-bound state start to decay reflecting that it starts tunneling out of the structure. It is generally known that the higher the resonant peak, the shorter the charge build-up time. Consequently, I can reasonably draw the following picture of the process: The incident charge first quickly populate the higher state within the energy spread of the wave packet and then fully fill it. When the charge density starts decaying in the high resonant state, the charge in the lower resonant state is still in the build up stage.

In order to understand the early dynamics of the charge build-up process, snapshots along the time axis of Fig. 2.2 are shown in Figs. 2.3, 2.4, and 2.5 for different time intervals. By inspection of these figures, three important features can be observed: (1) from 0-40 fs, the quasi-bound states of the double barrier structure quantum well are not reflected in the charge build-up profile $q(t, E_{ci})$; (2) during the next time period 40-200 fs(40-450 fs), the first excited (ground) quasi-bound state resonance peak develops and appear initially to be *blue-shifted* from a fixed energy positions by as much as 26 meV for both quasi-

Reproduced with permission of the copyright owner. Further reproduction prohibited without permission.

bound states; (3) the charge build-up resonance peaks bandwidth (FWHM) start to be large and then decreases as time increases.

To explain these features, let us refer to Fig. 2.6 that displays in its top portion the energy spectrum of a Gaussian wave packet of central energy E_{ci} that matches one of the quasi-bound state energies. In the lower portion is the corresponding quasi-bound state energy position center at E and energy spread 2Δ. In interpreting the first observation, namely, no resonant peaks in $q(t, E_{ci})$ for the first 40 fs, notice that resonance occurs only when the incident energy *matches* the quasi-bound state energy. The wave packet's high energy portion that reaches the structure in the 0-40 fs time period corresponds to energies that are larger than $E+\Delta$. This wave packet's energy does not *match* the resonant energy and as a result resonant features are not reflected in the charge profile $q(t, E_{ci})$ in the first 40 fs.

Referring to the second feature, Fig. 2.7a displays the charge build-up resonant peak energy position as a function of time when the wave packet's central incident energy matches the first excited state central energy. The peak position starts at 270 meV and shifts to a position of 244 meV in a time period of 200 fs. The peak position remains at 244 meV as time passes the 200 fs. To explain this shift, note that as time passes 40 fs, the wave packet's energies that are equal or slightly less than $E+\Delta$ reach and match the corresponding part of the quasi-bound state (Fig. 2.6). As a result, a resonance will occur at that energy (blue shifted from E). As time increases, wave packet's energies that are closer to E will reach and match the corresponding energy at the quasi-bound state where the resonance takes place. The closer the

Reproduced with permission of the copyright owner. Further reproduction prohibited without permission.

wave packet's energy portion to the central energy E, the more significant that energy is. As time increases further, such that wave packet's energies less than E reach and match the corresponding part of the quasi-bound state, the peak position will not be shifted because those energies will be less significant than energies close to E that are still in the quantum well.

To explain the third feature, Fig. 2.7b shows the charge build-up resonant peak bandwidth (FWHM) as a function of time for a wave packet's energy that matches that of the first excited state. This FWHM starts to be about 100 meV at t=50 fs and reduces to 24 meV at t=250 meV. As time passes 250 fs, the FWHM remains at 24 meV until the charge tunnels out of the structure. This observation can be explained as follows: the resonant peak start developing initially due to wave packet energies close to $E+\Delta$. These energies have a large FWHM and cover a large portion of the energy spread of the quasi-bound state. As wave packet's energies shift closer to the central energy E, their bandwidth is reduced thereby covering a small portion of the quasi-bound state energies and hence, the smaller the resonant peak bandwidth.

In Figs. (2.8) and (2.9) the temporal profiles of charge build-up at the ground and first excited states are displayed respectively, at several wave packet's central incident energy in the region of the resonance energies. From those figures, it is clear that charge build up probability peaks at the resonant energy. The time it takes the charge to reach a maximum and the charge decay time in the ground state is much larger than these in the first excited state. This is attributed to the tunneling probability being proportional to the energy level energy

Reproduced with permission of the copyright owner. Further reproduction prohibited without permission.

width. The energy width of the ground state energy level is much narrower than that of the first excited state.

It is important to mention that the above calculations were performed using a wave packet with a fixed spatial width of 550Å. Changing the packet's spatial width will not change the overall picture of charge build-up in the quantum well. In spite of how large is the wave packet's spatial width, there will a certain time needed for the resonance to occur. To verify this, Figs. (2.10) and (2.11) show the time evolution of charge inside the quantum well in the time region 0 to 60 fs when the wave packet is incident with it spatial width changed from 550-Å to 900-Å and 1200-Å, respectively. It is clear that even at the packet's width of 1200-Å, there is about 40 fs needed for the resonance to occur, which is not much different from that at 550-Å aside from the magnitude of the charge inside the well. The maximum charge build-up probability will not be different with different wave packet's spatial width unless the spatial width is reduced drastically such that the packet's energy width is larger than the resonance level energy spread. The charge decay time inside the quantum well is almost constant with different packet's spatial width.

It is also important to mention that in specifying the energy of a wave packet, we are only specifying the average central energy. The energy spread of a wave packet is controlled by controlling its spatial width. For the case at hand with a wave packet of 550-Å spatial width, the energy spread obtained by spectral analysis is about 20 meV. Energy-time uncertainty reveals that such energy spread corresponds to an excitation pulse width of ≈ 15 fs. This time width is small compared

Reproduced with permission of the copyright owner. Further reproduction prohibited without permission.

to the time scales of charge build-up and decay shown in our results. Hence, these results are accurate to ≈ 15 fs.

Finally, it is worth mentioning that such calculations may be useful in determining the ultimate speed of a tunneling device especially if such tunneling device is set to a threshold that is determined by the amount of charge inside the quantum well.

Reproduced with permission of the copyright owner. Further reproduction prohibited without permission.

2.4 References

1. R. Tsu and L. Esaki, Appl. Phys. Lett. **22**, 562 (1974).
2. H. Gou, K. Diff, G. Neofotistos, and J. Gunton, Appl. Phys. Lett. **53**, 131, (1988).
3. A. P. Jauho and M. Johnson, *Superlattices and Microstructures*, **6**, 303 (1989).
4. A. P. Jauho and M. Nieto, *Superlattices and Microstructures,* **2**, 407 (1986).
5. S. Collins, D. Lowe, and J. R. Barker, J. Phys. C: Solid state Phys. **20**, 6213 (1987).
6. F. Capasso, K. Mohammad, and A. Y. Cho, IEEE J. Quantum Electron. **QE-22**, 1853 (1986).
7. S. Collins, D. Lowe, and J. R. Barker, J. Phys. C: Solid state Phys. **20**, 6233 (1987).
8. M. Tsuchiya, T. Matsusue, and H. Sakaki, Phys. Rev. Lett. **59**, 2356 (1987).
9. Jin-feng Zhang and Ben-yuan Gu, Phys. Rev. B, **43**, 5028 (1991).
10. D. J. BenDanil and C. B. Duke, Phys. Rev. **152**, 683 (1966).
11. C. Juang, K. J. Kuhn, and R. B. Darling, Phys. Rev. B, **41**, 12047 (1990).
12. A. Goldberg, H. M. Schey, and J. C. Swarts, Am. J. Phys. **35**, 177 (1967).

Reproduced with permission of the copyright owner. Further reproduction prohibited without permission.

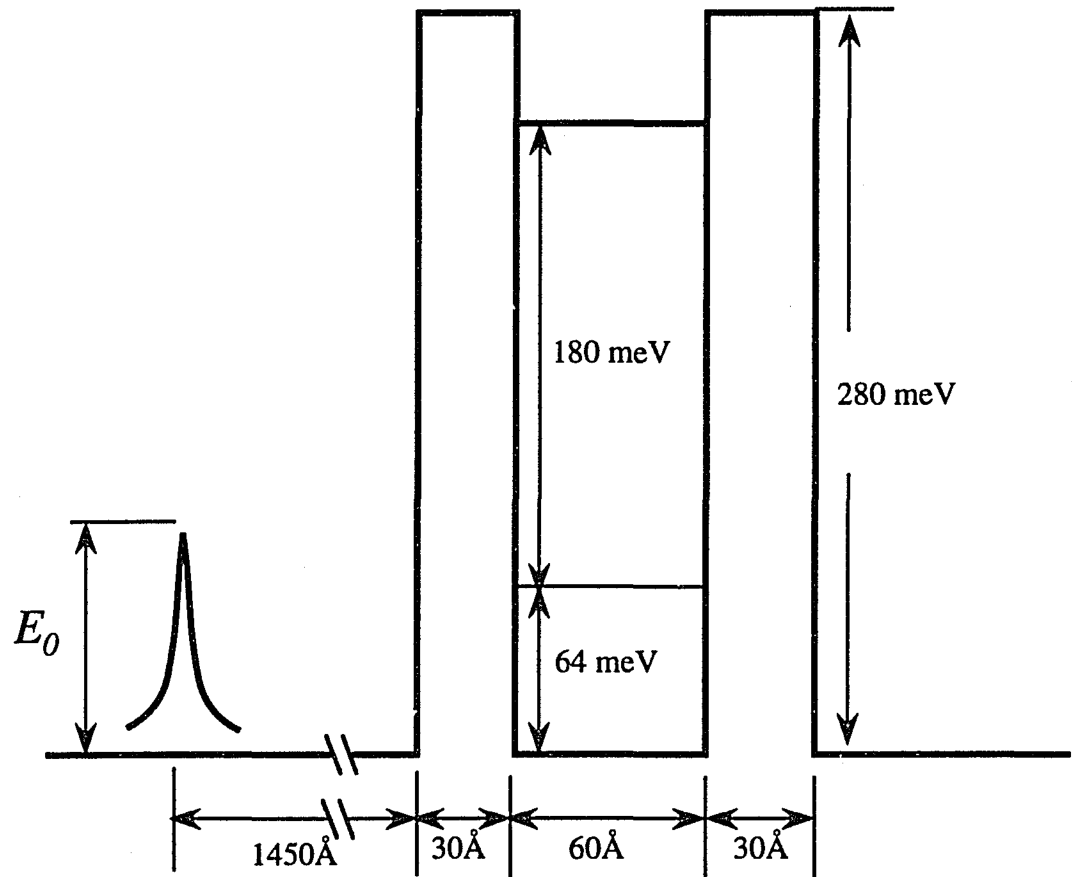

Fig. 2.1 A schematic diagram of the GaAs-AlGaAs double barrier structure used in our simulation. The structure consist of a 60Å GaAS quantum well and two 30Å AlGaAs barriers of 280 meV potential.

Reproduced with permission of the copyright owner. Further reproduction prohibited without permission.

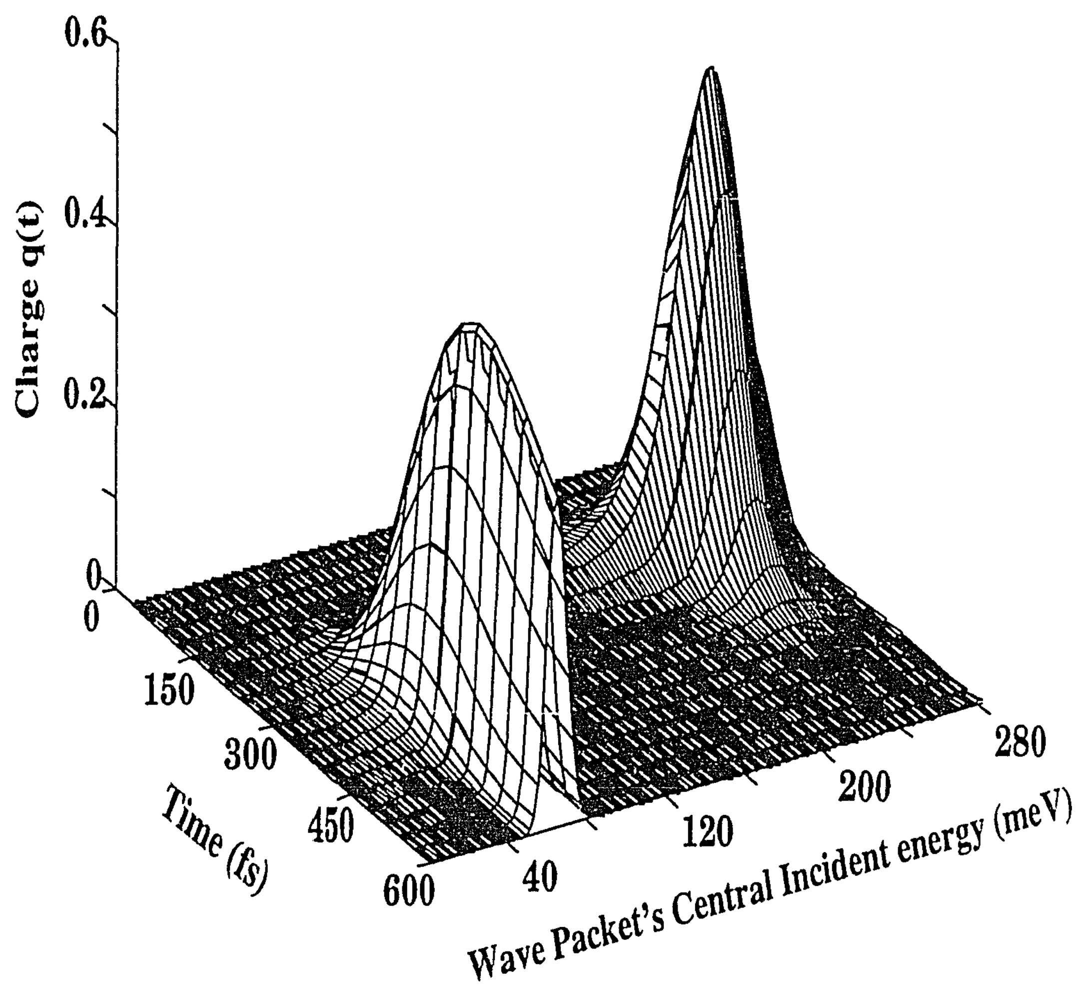

Fig.2.2 A 3-D plot of charge build-up inside the quantum well of a double barrier structure as a function of both time and wave packet central incident energy.

Reproduced with permission of the copyright owner. Further reproduction prohibited without permission.

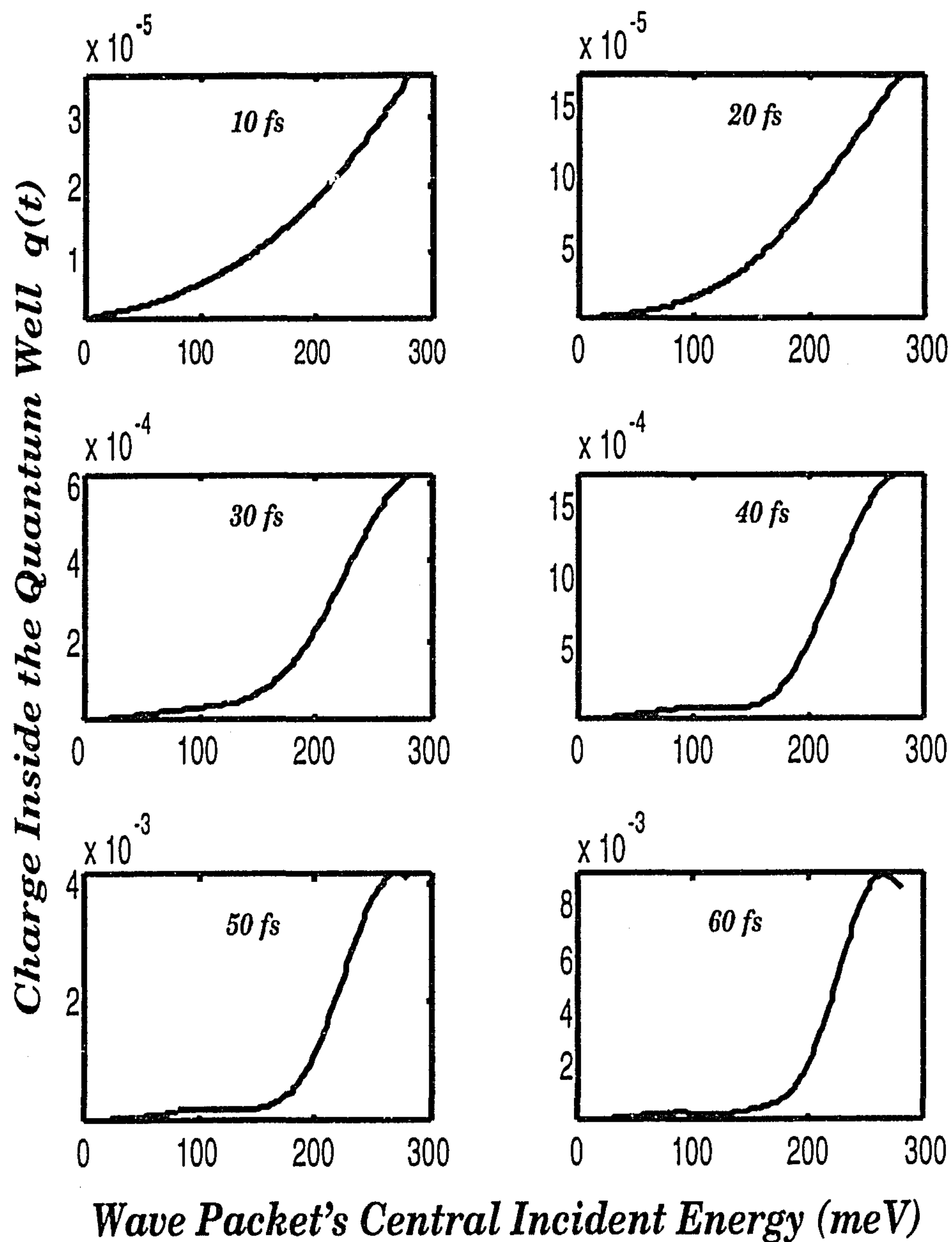

Fig.2.3 The time evolution of charge inside the quantum well of a double barrier structure shown in Fig.2.1 as a function of wave packet's central incident energy.

Reproduced with permission of the copyright owner. Further reproduction prohibited without permission.

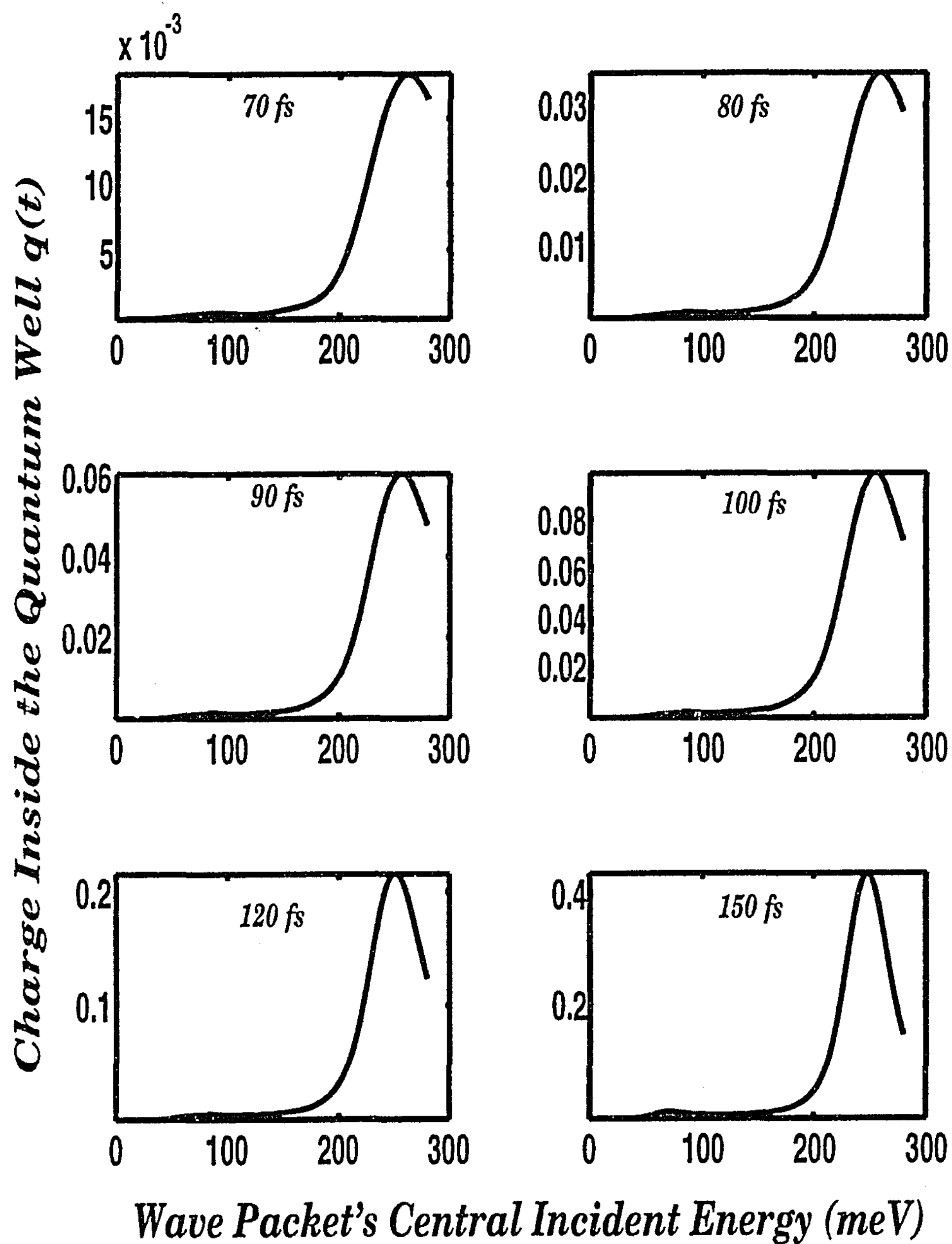

Fig.2.4 The time evolution of charge inside the quantum well of a double barrier structure shown in Fig.2.1 as a function of the wave packet's central incident energy.

Reproduced with permission of the copyright owner. Further reproduction prohibited without permission.

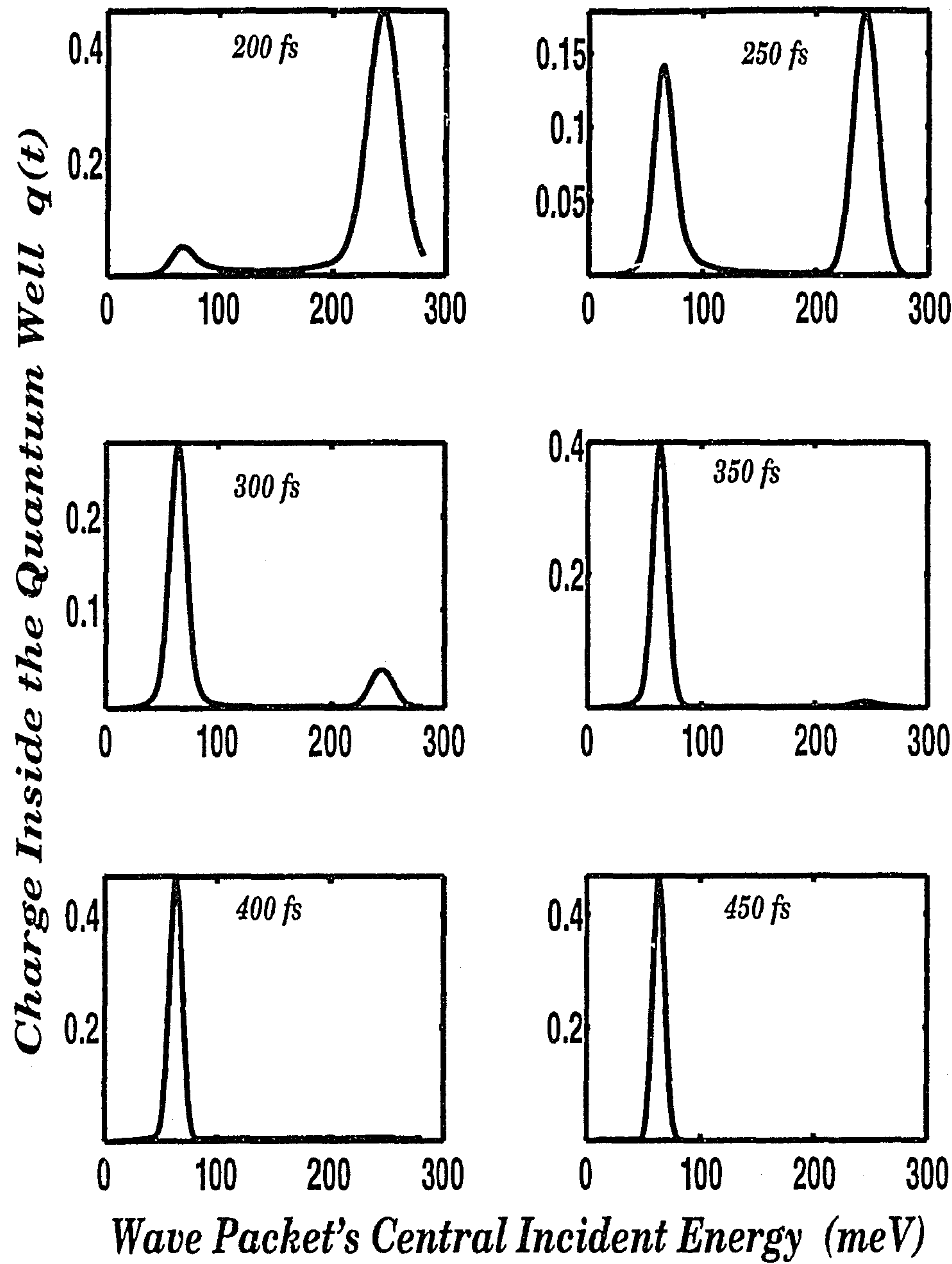

Fig.2.5 The time evolution of charge inside the quantum well of a double barrier structure shown in Fig.2.1 as a function of wave packet's central incident energy.

Reproduced with permission of the copyright owner. Further reproduction prohibited without permission.

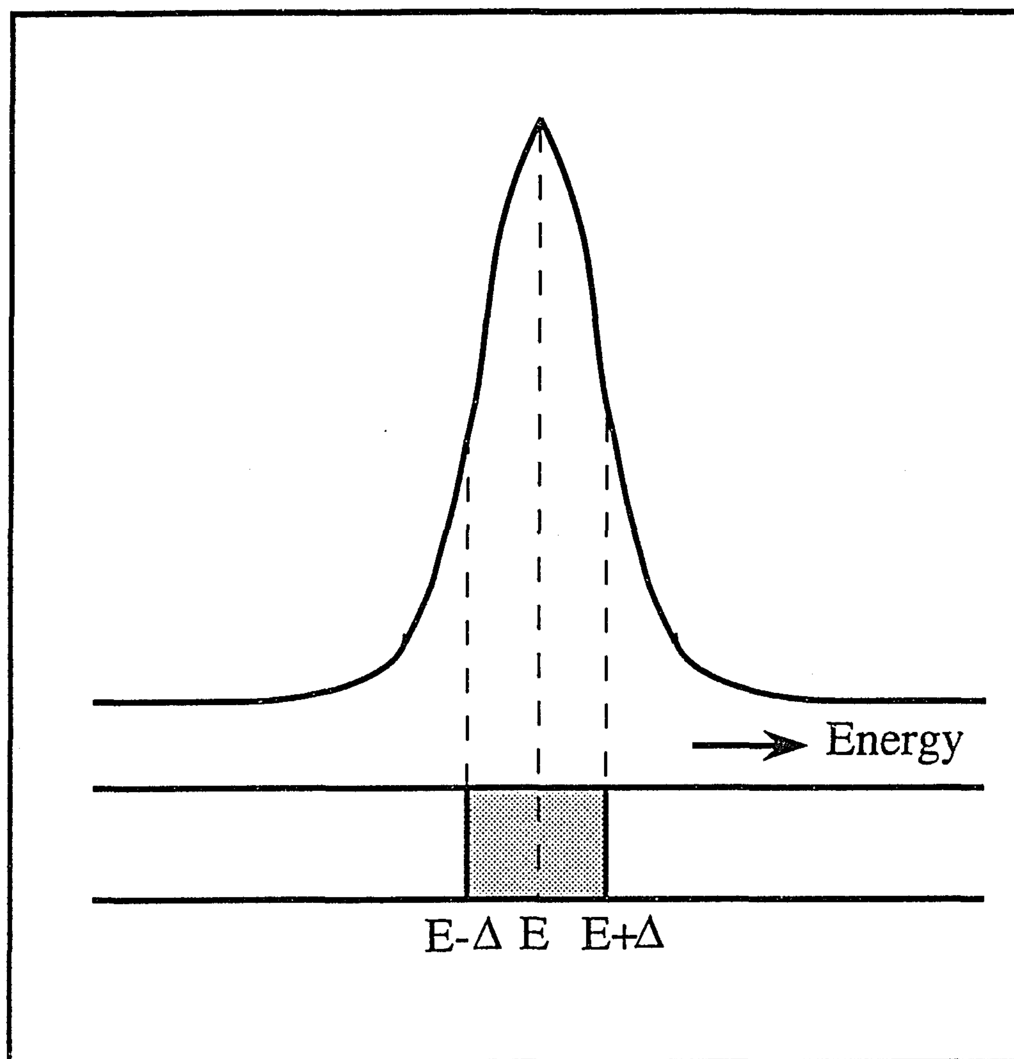

Fig. 2.6 A schematic diagram showing in the top portion a typical energy spectrum of a Gaussian wave packet with central energy E. THe lower portion shows the position of a quasi bound state centerd at E and has an energy spread of 2Δ

Reproduced with permission of the copyright owner. Further reproduction prohibited without permission.

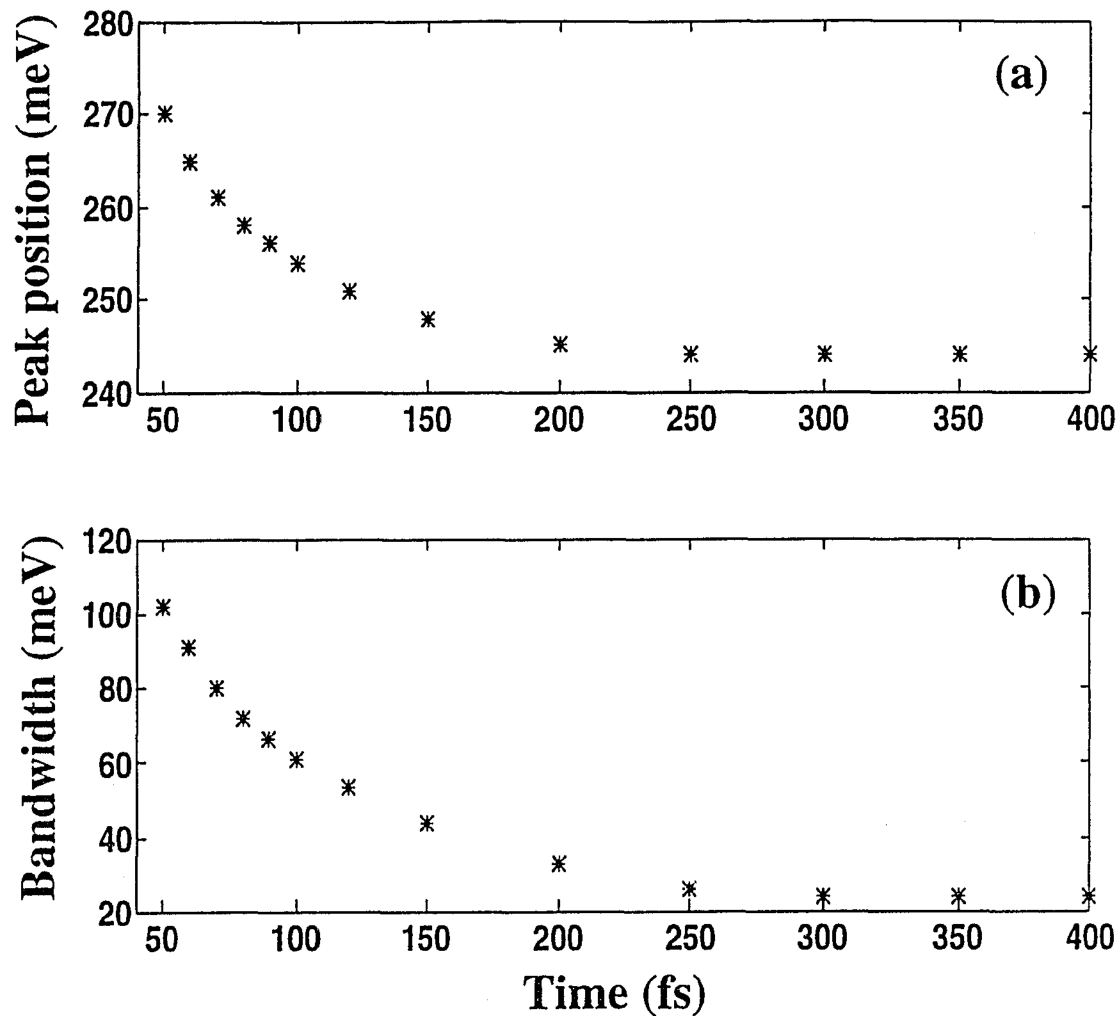

Fig. 2.7 The tempral behavior of the charge build-up resonance peak position and bandwidth of the first excited quasi bound state. The peak position and the bandwidth reach a fixed value after about 300 fs.

Reproduced with permission of the copyright owner. Further reproduction prohibited without permission.

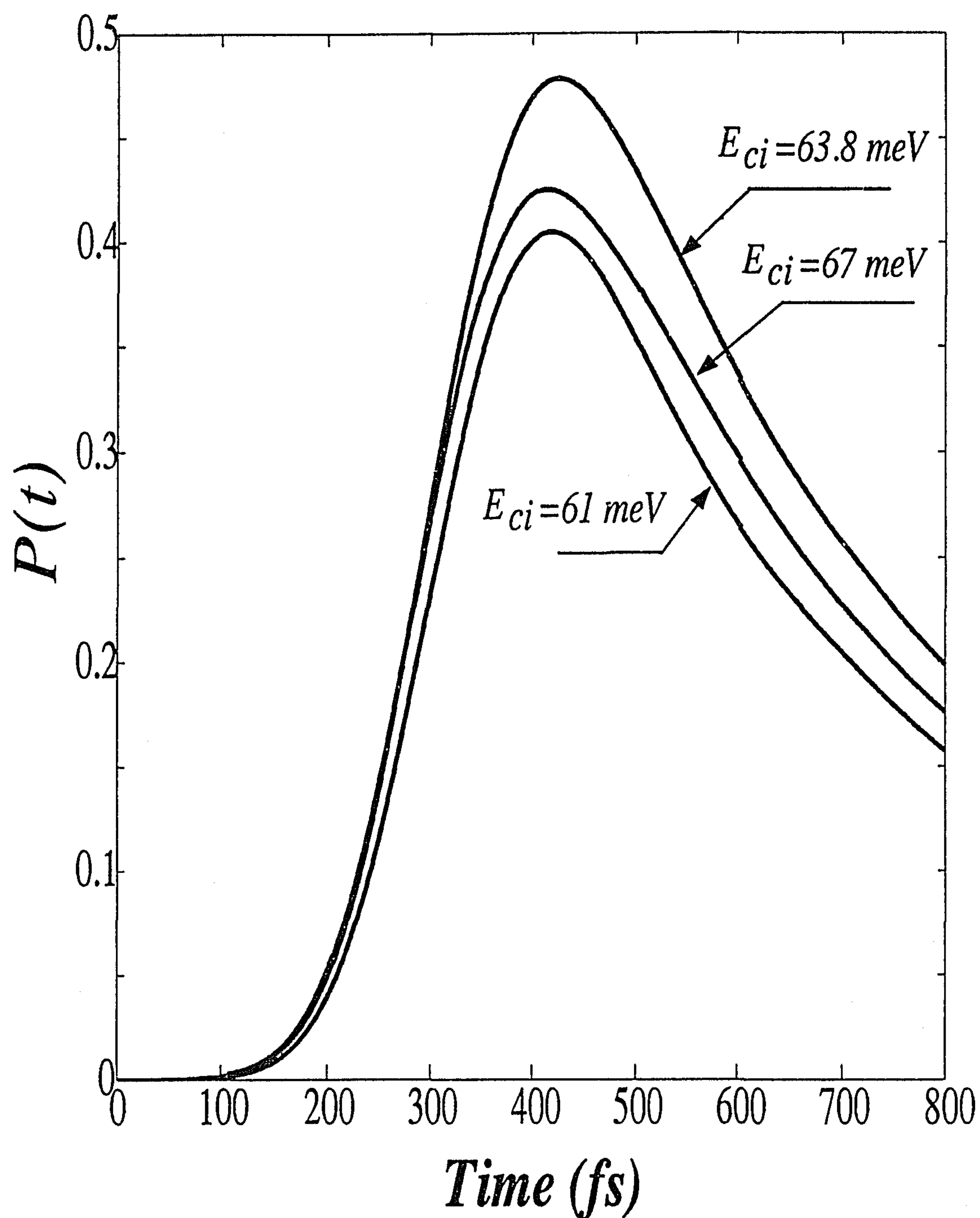

Fig. 2.8 The tempral behavior of charge build-up at the ground state of the double barrier structure used in this chapter with wave packet's energy matching the resonant energy (at E=63.8 meV) and with energy slightly different from the resonant energy.

Reproduced with permission of the copyright owner. Further reproduction prohibited without permission.

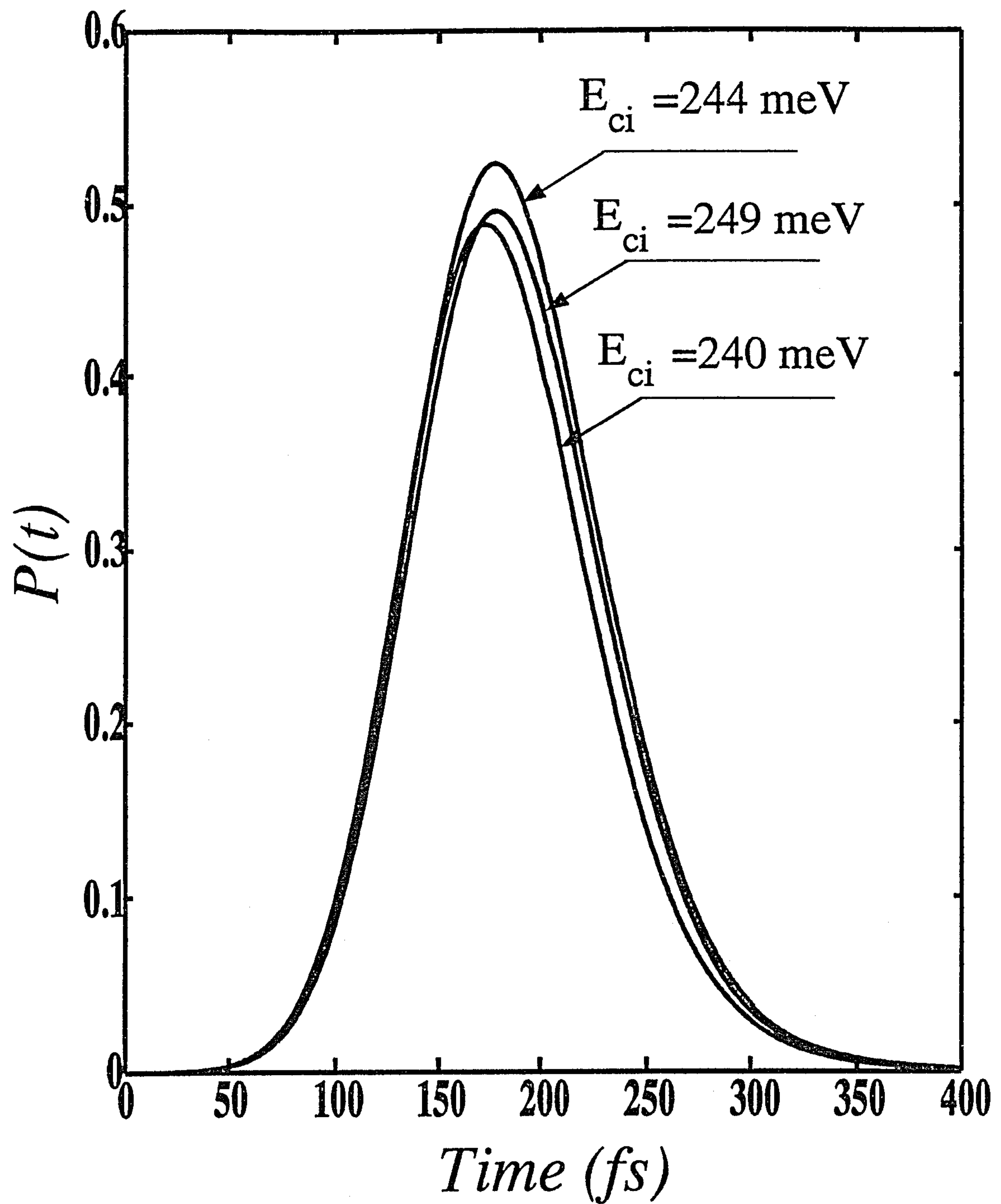

Fig. 2.9 The temporal behavior of the charge build-up at the first excited state in the double barrier structure used in this chapter with wave packet's energy matching the resonant state (E=244 meV) and when the wave packet's energy slightly deviates from resonance.

Reproduced with permission of the copyright owner. Further reproduction prohibited without permission.

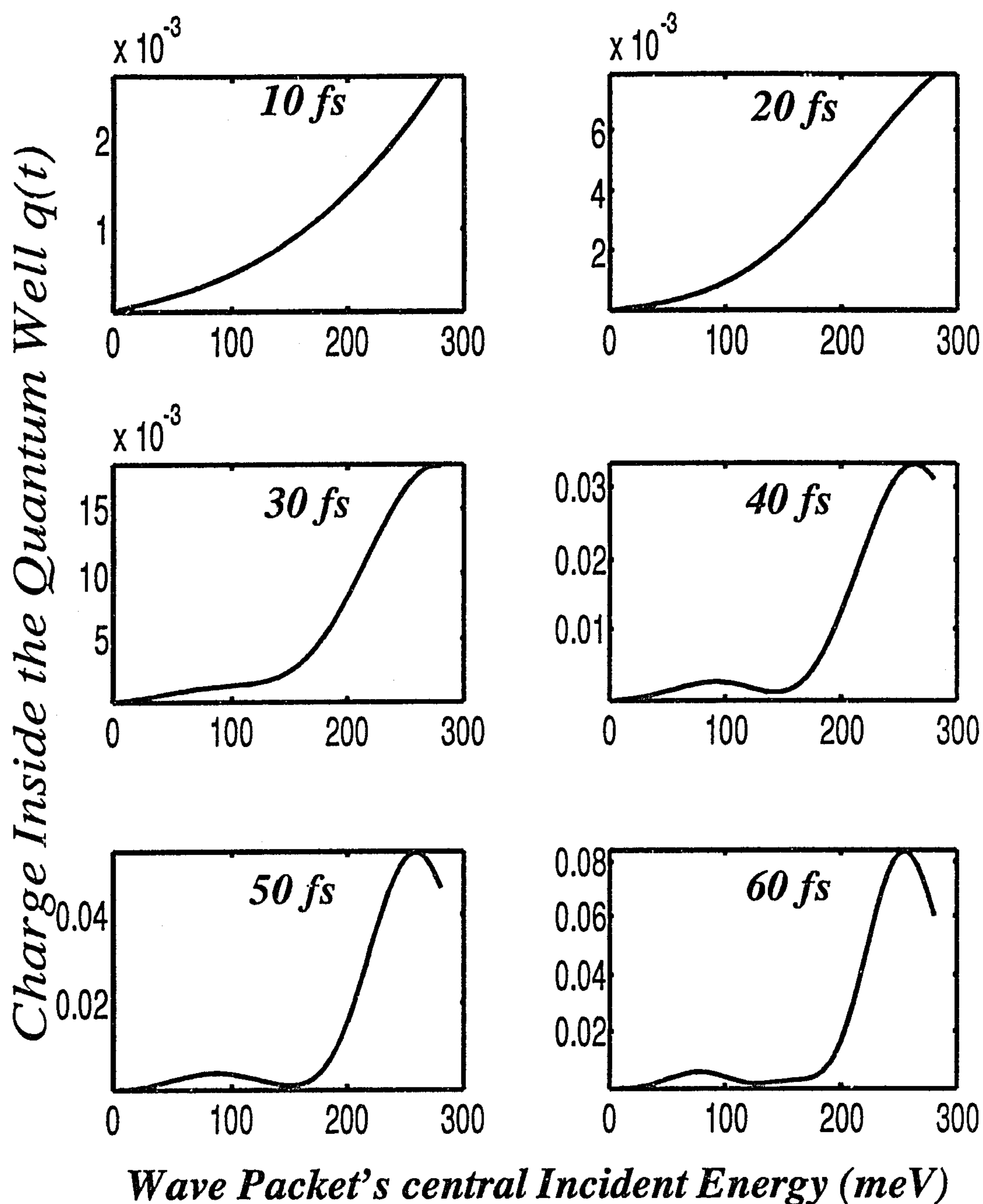

Fig. 2.10 The time evolution of charges inside the quantum well of the double barrier structure shown in Fig. 2.1 as a function of the wave packet's central incident energy and with a wave packet spatial width of 900A.

Reproduced with permission of the copyright owner. Further reproduction prohibited without permission.

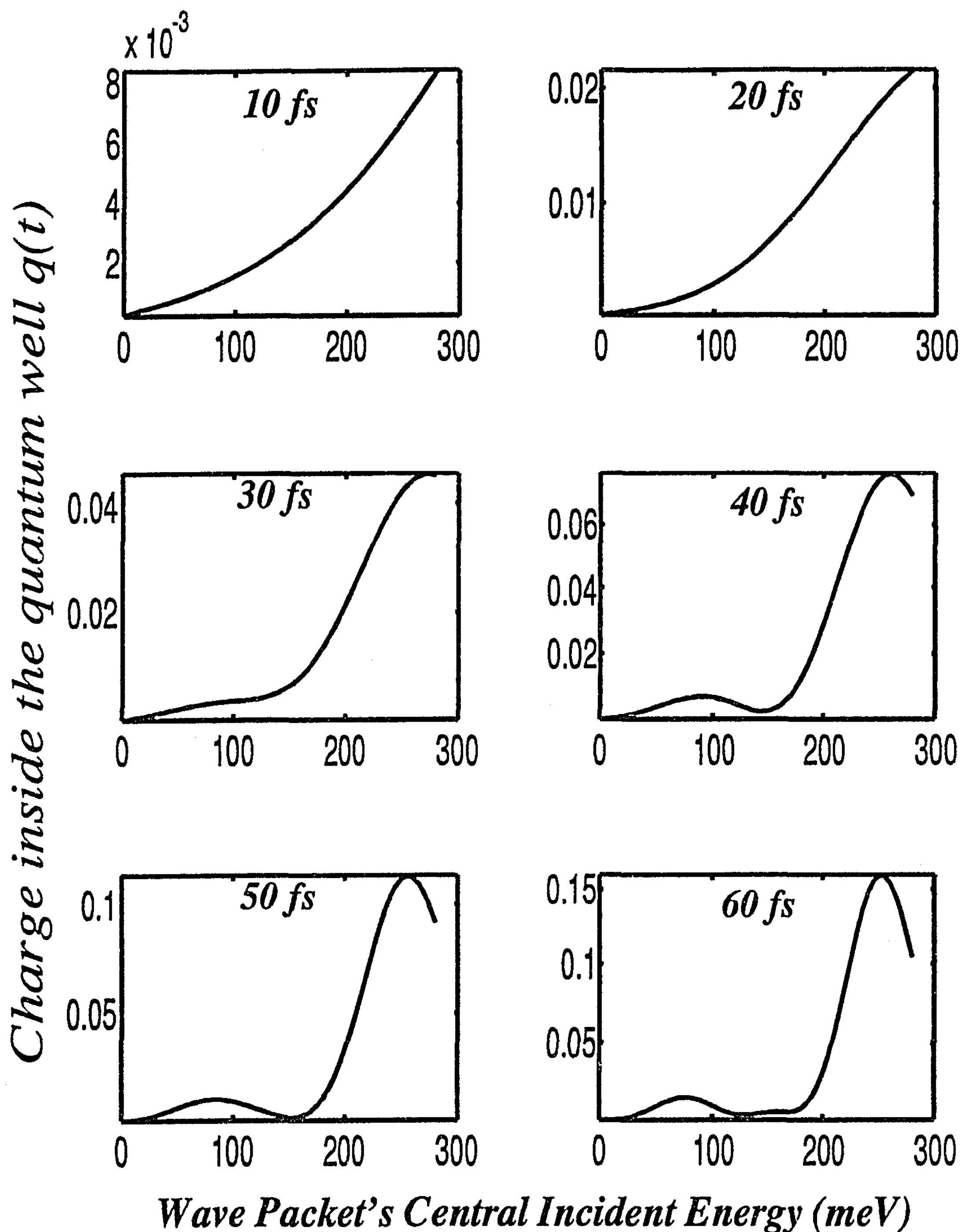

Fig. 2.11 The time evolution of charges inside the quantum well of the double barrier structure shown in Fig. 2.1 as a function of the wave packet's central incident energy and with a wave packet spatial width of 1200 A.

Reproduced with permission of the copyright owner. Further reproduction prohibited without permission.

CHAPTER THREE

EXCITONIC EFFECTS ON THE COHERENT OSCILLATION OF A PHOTOEXCITED ELECTRON WAVE PACKET IN COUPLED DOUBLE QUANTUM WELLS

3.1 Introduction

Beyond the double barrier single quantum well structure discussed in chapter 1, the simplest structure is the double well configuration. The double well configuration is simply two quantum wells separated by a thin barrier. In the case the quantum wells are of the same width, the structure is known as symmetric double quantum wells and if the widths are different it is known as asymmetric double quantum wells. Various researchers have studied tunneling in double quantum wells. Matsusue *et al*[1] studied the tunneling dynamics between a wide quantum well and a narrow well and that from the wide well to the continuum in the presence of electric field by means of photoluminescence (PL) technique. They showed that interwell tunneling and tunneling to the continuum is maximum when the two quantum wells are in resonance. Golub et al[2] used double quantum well structure to study the life times of direct and indirect excitons. In a strongly coupled double quantum wells (separated by a very thin

Reproduced with permission of the copyright owner. Further reproduction prohibited without permission.

barrier) Choi and co-workers (Ref. 3) studied the energy level structure as well as the oscillator strength by means of infrared photoelectron tunneling spectroscopy. Charge accumulation in a quantum well of a double-barrier structure[4,5] has been determined using PL spectroscopy, where it is shown that the maximum charge accumulation occurs when the structure is biased at resonance. The escape rate of electrons confined in a quantum well through a thin barrier to the continuum[6] was determined by measuring electron lifetimes using time-resolved PL.

Tunneling between double quantum wells is of special interest because of its potential device applications since tuning of the eigenstates can be achieved by the application of an electric field. An important feature of double quantum wells is the coherent oscillation of a photoexcited electron wave packet between the two wells under resonance condition. The experimental observation of the charge oscillation was reported by Shah and co-workers[7] using four-wave mixing and pump-and-probe spectroscopies. A potential application of the double well structure is the generation of a high frequency radiation due the charge oscillation. Coherent submillimeter wave emission from such structure was reported by Roskos *et al.*[8]

In this chapter, I have studied tunneling in asymmetrical double-quantum-well structure consisting of a wide well and a narrow well to address the effect of electron-hole Coulomb interaction on the electron wave packet oscillation between the two wells which was not addressed or well known in the previous work by other researchers. I have shown both in time and energy domains that the Coulomb interaction affects the oscillation behavior of an electron wave packet in coupled double

Reproduced with permission of the copyright owner. Further reproduction prohibited without permission.

quantum wells. This effect is found to be finite and in the vicinity of 15%.

3.2 Theory

A schematic representation of an asymmetrical coupled double quantum well consisting of a wide well and a narrow well separated by a thin barrier is shown in Fig. 3.1. This structure allows the selective excitation of an electron wave packet in the wide well because of the difference in the ground state energies of the two wells. As the barrier thickness is decreased, the exponentially decaying wave function in the barrier can have some finite value in the next well. The interest in such kind of structure lies not only in understanding the tunneling basic physics but also in the use as a high frequency generator.

The tunneling dynamics of electrons is expected to vary with electric field. Under flat band conditions (Fig. 3.2a) known also as the "below-resonance" condition where the ground level E_{w1} of electrons in the wide quantum well is below the that E_{n1} of the narrow quantum well, the tunneling probability of electron from the wide well to the narrow well will be small, since the coupling between the two wells will be weak. Under the resonant condition (Fig. 3.2b), the ground state levels of both quantum wells coincide and electrons tunnel back and forth between the two wells since coupling between the two wells is maximum and probability of tunneling between the two wells will be large. When the electric field is made further negative (Fig. 3.2c), the ground level of the narrow quantum well goes above that of the wide

Reproduced with permission of the copyright owner. Further reproduction prohibited without permission.

quantum well. In such an "above resonance" condition, the penetration of the wave function to the narrow quantum well decreases again since the coupling between the two wells will be smaller. Note in this structure, the charge populate the wider well because of the selective excitation.

At the minimum level separation (i.e., resonance condition,), the ground state wave functions are $\psi^{+}$and ψ^{-}, the familiar symmetric and asymmetric wave functions, respectively. These wave functions can be expressed as:

$$\psi^{\pm} = a_{\pm}^{w}\Phi_{w} + a_{\pm}^{n}\Phi_{n}, \tag{3.1}$$

where the coefficients $a_{\pm}^{w}$and $a_{\pm}^{n}$ depend on the bias field F. The time-independent Schrödinger equation can be written as the eigen-value problem:

$$\begin{pmatrix} E_w - E_{\pm} & -u \\ -u & E_n - E_{\pm} \end{pmatrix} \begin{pmatrix} a_{\pm}^{w} \\ a_{\pm}^{n} \end{pmatrix} = 0, \tag{3.2}$$

where $E_w = E_w^0 - eFd$, $E_n = E_n^0 + eFd$, u is the coupling energy, and $2d$ is the distance between the center positions of the two wells. E_w^0 represents the unperturbed confinement energy of the ground state of the wide quantum well with no electric field, E_n^0 is that for the narrow well.

Under resonance conditions (Fig. 3.2b) the electron wave packet excited by a laser pulse in the wider well will oscillate back and forth between the two wells. The oscillation period is governed by the strength of coupling between the two wells. The photoexcitation of an electron wave packet in the wider well will simultaneously create a hole

Reproduced with permission of the copyright owner. Further reproduction prohibited without permission.

wave packet, which will affect the behavior of the electron wave packet oscillation through the Coulomb interaction. An electron in the valence band of the structure will absorb a photon of proper energy through photoexcitation and fill an empty state in the conduction band leaving behind an empty state or a hole. At the resonant condition where the coupling between the two well is maximum, the photoexcited electron will oscillate between the two wells. The empty hole left behind in the valence will try to decelerate the electron due to the force of attraction between them. The effect of which is expected to enlarge the oscillation period. A schematic representation of the of this process is illustrated in Fig. 3.3.

The asymmetric double-quantum-well structure used in our calculation consists of a 170-Å GaAs well, 17-Å $Al_{0.35}Ga_{0.65}As$ barrier, and a 120-Å GaAs well.

The numerical solution of the Schrödinger equation follow the procedure detailed in section 2.2 with an initial electron wave function $\psi(z,r,t=0)$:

$$\psi(z,r,t=0)=sin\left(\frac{\pi(z-z_0)}{L_z}\right)exp\left(-\frac{(r-r_0)^2}{4\sigma^2}\right), \tag{3.3}$$

where L_z is the wide well width, z_0 is the center location of the wave packet in the growth direction and $\sigma, r,$ and r_0 are the wave packet's spatial width, spatial position, and center location in the transverse direction, respectively.

Reproduced with permission of the copyright owner. Further reproduction prohibited without permission.

By assuming a fixed position of the wave packet in the transverse direction, that is $r = r_0$, the solution will be limited to the one-dimensional case, or simply $\psi(z,r,t) = \psi(z,t)$.

In the problem at hand the potential term $V(z)$ in the Schrödinger equation will consist this time of three different terms: the potential due the band edge discontinuity between GaAs and $Al_{0.35}Ga_{0.65}As$ $V_0(z)$, the potential change due to the application of the electric field $-eFz$ where F is the magnitude of the electric field, and the potential due the electron-hole Coulomb interaction $C(z)$. The potential variation due the electron-hole interaction is given by:

$$C(z) = \frac{-e^2}{4\pi\varepsilon_\infty\varepsilon_0\sqrt{(z-z_0)^2 + r_0^2}}, \tag{3.4}$$

or the potential can be written as follows:

$$V(z) = V_o(z) - eFz + C(z) \tag{3.5}$$

where z_0 is the fixed position of the hole, z is position of the moving electron, ε_∞ is the high frequency dielectric constant, ε_0 is the free space permitivity, and e is the electron charge.

In our computations of the potential, probability of tunneling, and the charge in the various places within the double well structure we assumed the hole to be fixed and located at the midpoint of the wider well because of its heavy mass compared to the electron mass. The spatial separation between the electron and the hole in the x-y plane

Reproduced with permission of the copyright owner. Further reproduction prohibited without permission.

(perpendicular to the growth direction) is assumed also to be on the average, the 2D Bohr radius (r_0) which is 57-Å in GaAs.

At time t=0, the initial electron wave packet is placed in the wider well, the electric field required for resonance to occur is turned on and the tunneling process is initiated. The development of the wave function $\psi(z,t)$ in time is followed as the packet moves into and out of the narrow well (*nw*). The charge inside the narrow well is calculated by integrating the amplitude of the wave function inside the narrow well:

$$Q_{NW} = e\int \psi^*_{NW}\psi_{NW}dz \qquad (3.6)$$

We use the procedure developed in chapter two to solve the time-dependent Schrödinger equation with the structure of the double quantum well and potential given via equation (3.5).

3.3 Results and Discussion

Two periods of the electron wave packet oscillation (solid line) are shown in Fig. 3.4 when the Coulomb interaction term $C(z)$ is neglected. The salient feature to be noticed from the profile in this figure is that the electron wave packet oscillation period is about 1.21 ps. Changing the width of the central barrier will change the splitting between the energy levels ($\Delta E = E_1 - E_2$, Fig. 3.3) and, hence, the oscillation period will be changed as will be shown later in the chapter. The dotted line in Fig. 3.4 shows the electron wave packet oscillation when the Coulomb interaction term $C(z)$ included. It is noticed that the

Reproduced with permission of the copyright owner. Further reproduction prohibited without permission.

oscillation period has shifted and changed to 1.36 ps, which agrees with the energy difference ΔE of about 3 meV between the energy levels of the two quantum wells measured by Leo *et al.*[7]

The oscillation periods in both cases (with and without Coulomb interaction) behave similarly, but are shifted in time from each other. By inspecting the first period, when most of the wave packet is still in the wide well, the Coulomb interaction does not show a clear effect, while it is more pronounced when the wave packet is in the narrow well region. This result can be interpreted as follows: when the wave packet is in the wide well, part of the packet moving toward the hole is accelerated, while the other part moving away from the hole is attracted by the hole. The two actions on the whole wave packet almost exactly compensate for each other. The Coulomb interaction effect becomes stronger when the wave packet approaches the narrow well since the *whole wave packet* is being retarded. The net effect is an increase of the oscillation period by about 150 fs for each period.

The effect of the Coulomb interaction on the electron wave packet oscillation, shown already in the time domain, can also be demonstrated in the energy domain. Because of the difficulty to determine the location of the energy levels in the coupled double quantum well structure shown in Fig. 3.3 using my numerical method, I will employ a test structure shown in the inset of Fig. 3.5 to determine the energy separation ΔE between the two levels (E_1 and E_2) with and without Coulomb interaction. By sending a variable-energy wave packet from the left lead of the structure, the time integrated current density is calculated at 50-Å to the right of the last barrier as a function of energy. Figure 3.5 shows

Reproduced with permission of the copyright owner. Further reproduction prohibited without permission.

the time-integrated current density versus energy without (solid curve) and with (dotted curve) Coulomb interaction. Note that ΔE without Coulomb interaction equals 21.0 meV, while ΔE is 20.2 meV with Coulomb interaction. Since the oscillation period $\Delta\tau$ of the wave packet can be expressed as $\Delta\tau = h/\Delta E$, smaller values of ΔE with the Coulomb interaction implies a larger oscillation period. In this test structure the oscillation period with Coulomb interaction is larger by about 8 fs.

Reproduced with permission of the copyright owner. Further reproduction prohibited without permission.

3.4 References

1. T. Matsusue, M. Tsychiya, J. Shulman, and H. Sakaki, Phys. Rev. B, **42**, 5719 (1990).
2. J. E. Golub, K. Kash, J. Harbison, and L. Flores, Phys. Rev. B **41**, 8564 (1990)
3. K. Choi, B. Levine, C. Bethea, J. Walker, and R. Malik, Phys. Rev. B **39**, 8029 (1989)
3. B. Deveaud, A. Chomette, F. Clerot, P. Auvrsy, A. Regreny, R. Ferreira, and G. Bastard, Phys. Rev. B, **42**, 7021 (1990).
4. J. Young, B. Wood, G. Aers, R. Devine, H. Liu, D. Landheer, M. Buchanan, A. SpringThrope, and P. Mandeville, Phys. Rev. Lett. **60**, 2085 (1988).
5. H. Yoshimura, J. Schulman, and H. Sakaki, Phys. Rev. Lett. **64**, 2422 (1990).
6. M. Tsuchiya, T. Matsusue, and H. Sakaki, Phys. Rev. Lett. **59**, 2356 (1987).
7. Karl Leo, J. Shah, E. Göbel, T. Damen, S. Schmitt, W. Schafer, and K. Köhler, Phys. Rev. Lett. **66**, 201 (1991).
8. H. Roskos, M. Nuss, J. Shah, K. leo, and D. Miller, Phys. Rev. lett.**68**, 2216 (1992)

Reproduced with permission of the copyright owner. Further reproduction prohibited without permission.

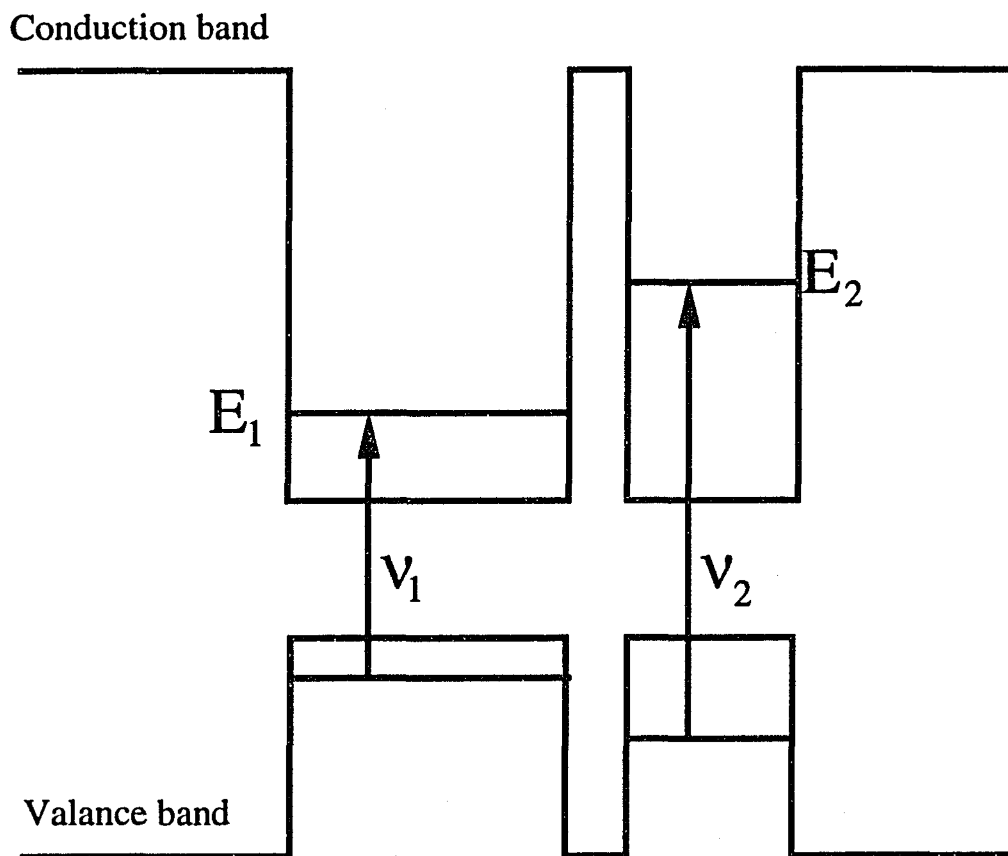

Fig. 3.1 A schematic illustation of a double quantum well structure showing in the difference in the excitation energies of the two wells which allow the ability to excite the wider well only by the proper choice of the excitation source excitation energy.

Reproduced with permission of the copyright owner. Further reproduction prohibited without permission.

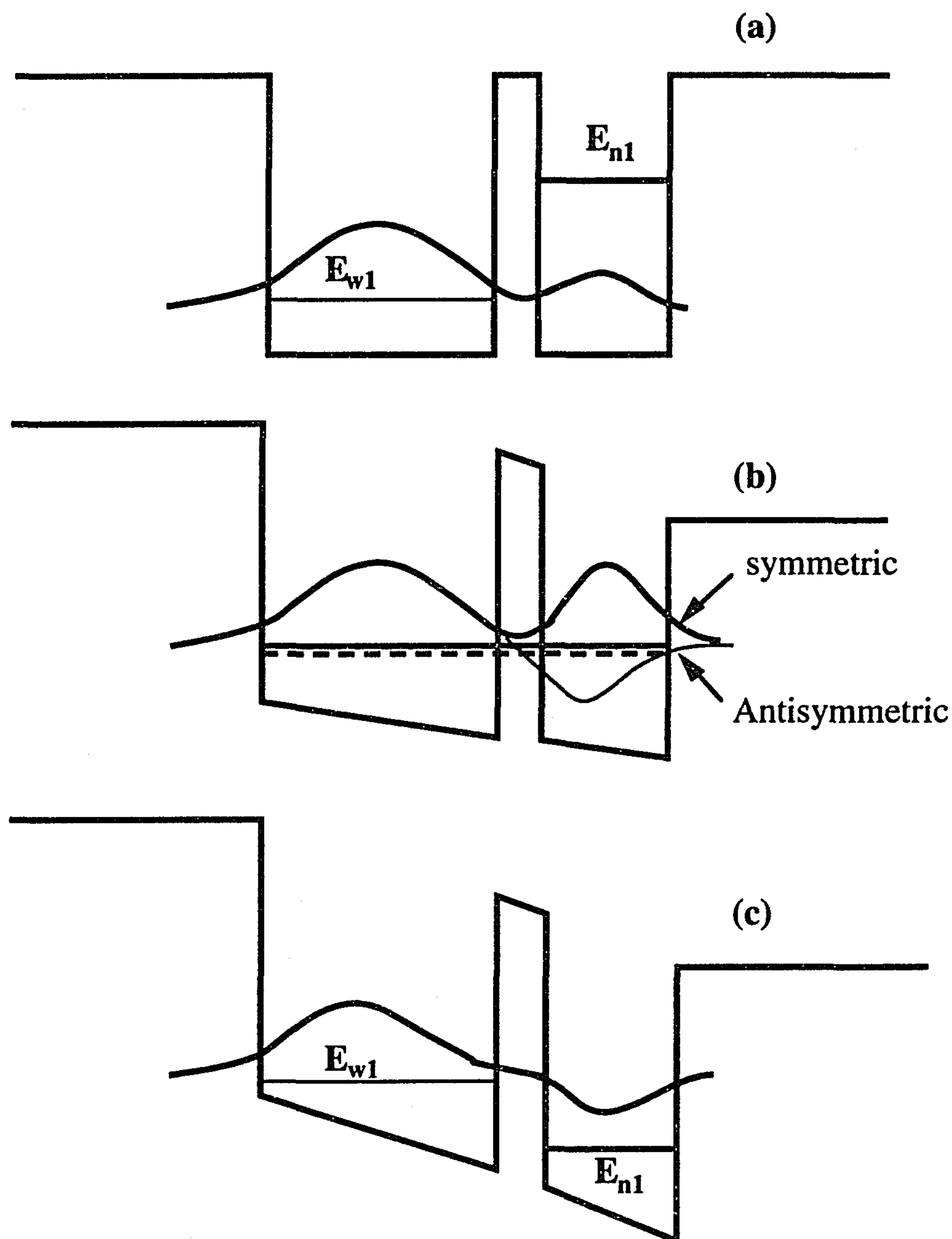

Fig. 3.2 Schematic illustration of wave function and tunneling processes of electrons associated mainly with the wide quantum well in a coupled quantum well structure under three representative conditions. Figures (a), (b), and (c) correspond, respectively, to "below" -resonance, on resonance, and "above -resonance conditions, where the energy level associated with the wide quantum well is lower than, equal to, and higher than that of the narrow well.

Reproduced with permission of the copyright owner. Further reproduction prohibited without permission.

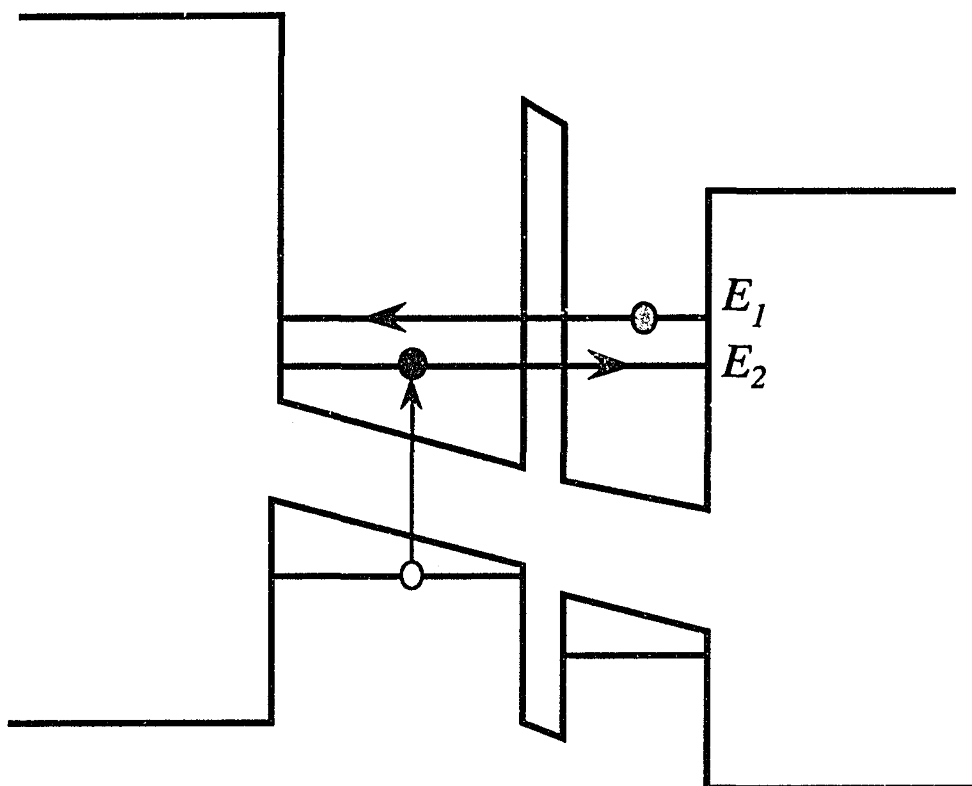

Fig 3.3 Selective photoexcitation of an electron wave packet in the wider well of a double-quantum-well structure. At resonance the wave packet will oscillate between the two wells. The width of the wide (narrow) well is 170 (120) Å and the barrier is 17Å with a height of 300 meV.

Reproduced with permission of the copyright owner. Further reproduction prohibited without permission.

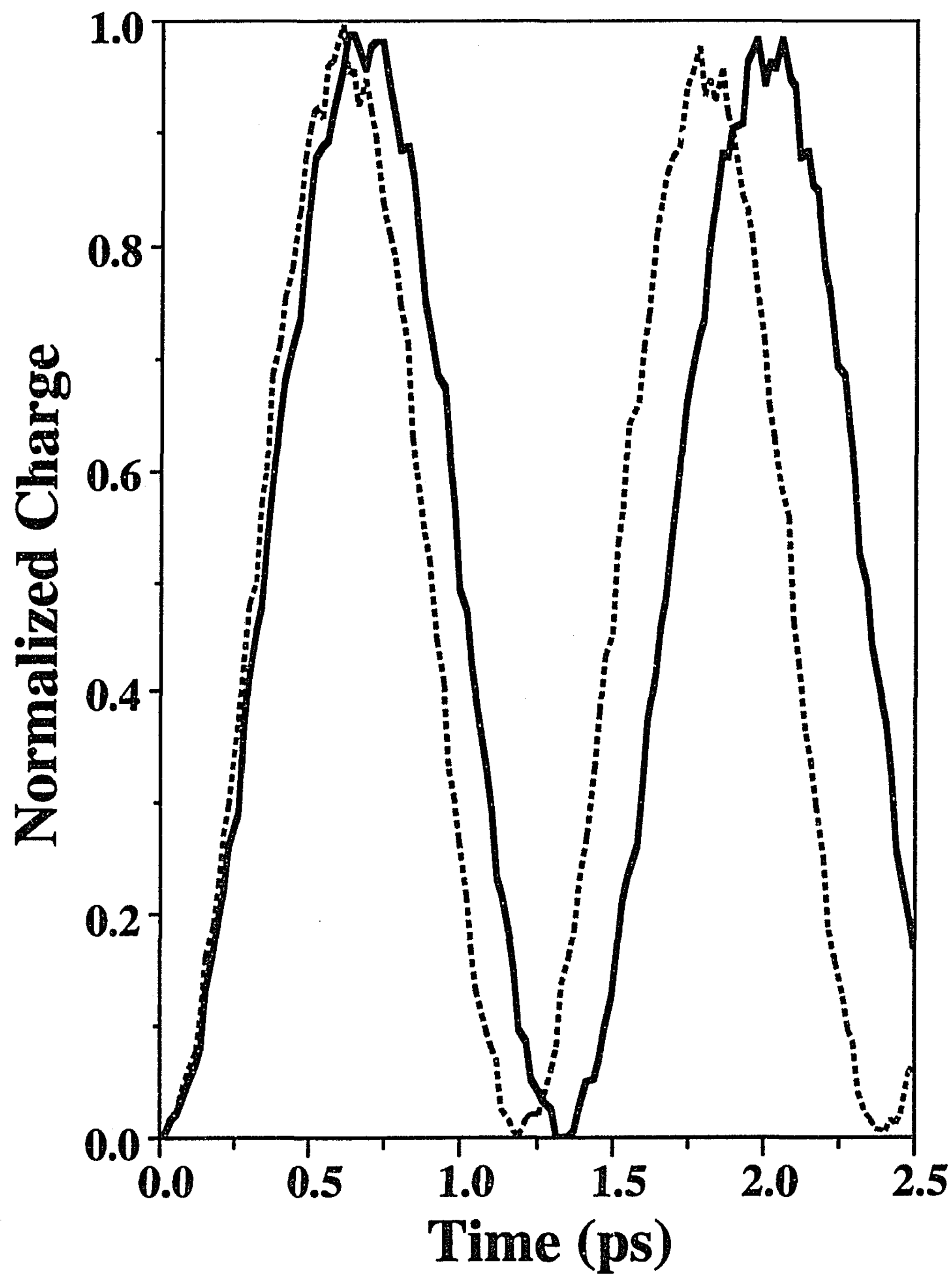

Fig. 3.4 Normalized Charge inside the narrow well as a function of time. The solid(dotted) line is the charge oscillation without (with) the Coulomb interaction.

Reproduced with permission of the copyright owner. Further reproduction prohibited without permission.

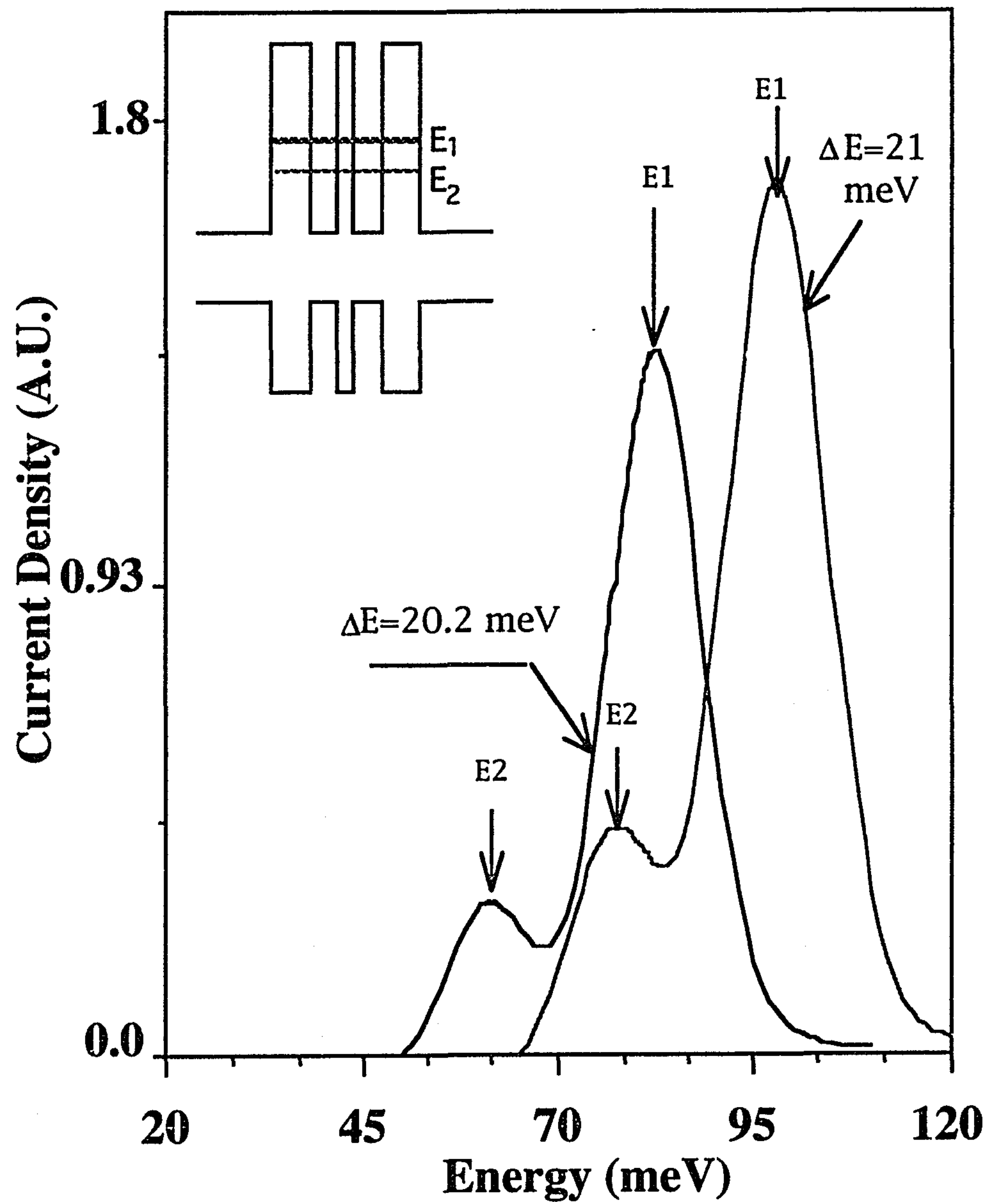

Fig. 3.5 Energy levels in a coupled quantum well structure without (solid) and with (dotted) Coulomb interaction.

Reproduced with permission of the copyright owner. Further reproduction prohibited without permission.

CHAPTER FOUR

ELECTRON TUNNELING DYNAMICS THROUGH A DOUBLE BARRIER STRUCTURE IN THE PRESENCE OF LO PHONON MODES

4.1 Introduction

Electron tunneling dynamics in double barrier devices has received special attention because of its novel electronic transport properties in high speed electronics. One of the important issues in the study of electron tunneling in nanostructures is the inelastic scattering through the electron-phonon interaction. Experimentally, Goldman, Tsui, and Cunningham[1] provided an evidence that the longitudinal optical (LO) phonon assists in tunneling in the valley current region of a double barrier structure. The effect of electron-phonon interaction on tunneling has been theoretically treated in the steady state by several investigators.[2-4] Gelfand *et al*[2] obtained the electron tunneling through a thin potential barrier with local Einstein phonons by means of a continued fraction expansion and demonstrated the feedback mechanism by which inelastic scattering alters the probability of elastic scattering. Wingreen *et al*[3] converted the problem to that of electron scattering in a single resonant state with phonons and confirmed the experimental results provided by Goldman *et al.*[1] Recently, a novel independent boson model approach was proposed by Cai *et al*[4] to calculate the 1-D electron

Reproduced with permission of the copyright owner. Further reproduction prohibited without permission.

tunneling probability with electron-phonon interaction. They showed how the boundary conditions uniquely determine the transmitted and reflected currents. Dynamics of electron tunneling through double barrier structures without phonons has also been treated by several investigators. Collins *et al*[5] showed that the temporal behavior of resonant tunneling is characterized by a time constant of $\tau=2h/\Gamma$, where Γ is the resonant energy width. Guo *et al*[6] estimated the charge build-up time by calculating the probability of finding the electron inside the quantum well of a double barrier structure. The tunneling dynamics in the presence of phonons has not been properly treated. Some researchers[7,8] tried to carry out an analogy to electron tunneling with phonons by considering a time modulated barrier height, where transmitted current was found to have energy side bands (analogous to absorption or emission of phonon quanta). This analogy is not complete simply because phonon population can not be accounted for.

In this chapter, a method was developed to investigate the temporal dynamics of electron tunneling by directly solving the time dependent Schrödinger's equation. This method allows us to calculate several important time constants such as tunneling time and charge build up time in the presence of different phonon modes in a semiconductor nanostructure. The method was demonstrated by studying electron-tunneling dynamics through a GaAs/AlGaAs based double barrier structure in the presence of plane wave phonons. The temporal profiles of the tunneling current density are calculated at different temperatures. The magnitude of the current density is shown to decrease when the effect of the electron-phonon coupling on resonant

Reproduced with permission of the copyright owner. Further reproduction prohibited without permission.

tunneling is taken into account due to inelastic-scattering-induced reflection increase. The temperature dependence of the tunneling peak current density is compared with the available experimental data.[9]

4.2 Theory

In this section, I outline the theory of electron-phonon interaction and will apply it to the case of an electron wave packet tunneling through a double barrier structure.

The Hamiltonian of the electron and phonon system is given by:

$$H = H_e + H_{ph} + H_{e-ph}. \tag{4.1}$$

Here H_e is the Hamiltonian for a pure electronic system which was mentioned in chapter 2 and is repeated here for convenience:

$$H_e = -\frac{\hbar^2}{2}\frac{\partial}{\partial z}\frac{1}{m^*(z)}\frac{\partial}{\partial z} + V_0(z), \tag{4.2}$$

where $V_0(z)$ is the potential profile of the selected double barrier structure. In this chapter, I chose a structure consisting of a 45-Å GaAs quantum well sandwiched between two 28-Å $Al_{0.3}Ga_{0.7}As$ barriers. H_{ph} is the Hamiltonian for a pure phonon system. In my model the phonon system is considered to be in a dynamic equilibrium state with a characteristic temperature *T*. Furthermore, the effect of electron-phonon interaction on the phonon system is assumed to be weak enough. Therefore, H_{ph} is neglected in our model. H_{e-ph} is the Hamiltonian for

Reproduced with permission of the copyright owner. Further reproduction prohibited without permission.

the electron-phonon interaction, an interaction Hamiltonian which I will derive below.

To begin with, consider the diatomic model of a linear chain in which the macroscopic theory is fully embodied in the following pair of equations:

$$\ddot{u} = b_{11}u + b_{12}E \tag{4.3}$$

$$P = b_{12}u + b_{22}E \tag{4.4}$$

where u is defined as the relative displacements between the positive and negative ions in the lattice chain. P is the dielectric macroscopic polarization and E is the total electric field (due to the polarization and the free charges). The $b's$ are constants to be determined. For the system under consideration, the dielectric constant for any particular frequency ω can be deduced from Eqs. (4.3) and (4.4) by considering harmonic like solution as follows:

$$\left.\begin{array}{l} E = E_o \\ u = u_o \\ P = P_o \end{array}\right\} \times e^{-i\omega t} \tag{4.5}$$

Thus we obtain from these equations,

$$\begin{array}{r} -\omega^2 u = b_{11}u + b_{12}E, \\ P = b_{12}u + b_{22}E \end{array} \tag{4.6}$$

when u is eliminated from this equation, it is seen that P and E are related by:

Reproduced with permission of the copyright owner. Further reproduction prohibited without permission.

$$P=\left\{b_{22}-\frac{b_{12}^2}{-b_{11}-\omega^2}\right\}E. \tag{4.7}$$

Comparing this equation with the definition of the dielectric displacement,

$$D=\varepsilon_o E+P=\varepsilon E \tag{4.8}$$

we obtain the dielectric constant:

$$\varepsilon=\varepsilon_o+b_{22}+\frac{b_{12}^2}{-b_{11}-\omega^2} \tag{4.9}$$

which is most conveniently written as:

$$\varepsilon=\varepsilon_\infty+\frac{\varepsilon_o-\varepsilon_\infty}{1-(\omega/\omega_o)^2} \tag{4.10}$$

where ε_o is the static dielectric constant, ε_∞ is the high frequency dielectric constant and ω_o is the infrared dispersion frequency. Comparing the above two equations results in:

$$\begin{aligned} b_{11}&=-\omega_o^2\\ b_{12}&=\omega_o(\varepsilon_o-\varepsilon_\infty)^{\frac{1}{2}}\\ b_{22}&=\varepsilon_\infty-\varepsilon_o \end{aligned} \tag{4.11}$$

From Maxwell's equation:

$$\nabla.D=\nabla.(\varepsilon_o E+P)=\rho \tag{4.12}$$

Substituting Eq. (4.4) in Eq. (4.12) results in:

$$\nabla.E=\frac{1}{\varepsilon_o+b_{22}}\{-b_{12}\nabla.u+\rho\} \tag{4.13}$$

Reproduced with permission of the copyright owner. Further reproduction prohibited without permission.

From vector algebra, the vector u can be split into two parts, a solenoidal and irrotational(transverse and longitudinal):

$$u = u_t + u_l \tag{4.14}$$

such that

$$\begin{aligned} \nabla . u_t &= 0 \\ \nabla \times u_l &= 0 \end{aligned} \tag{4.15}$$

then Eq. (4.13) becomes:

$$\nabla . E = \frac{1}{\varepsilon_o + b_{22}} \{ -b_{12} \nabla . u_l + \rho \} \tag{4.16}$$

if the there were no free charges, then $E = -(b_{12}/\varepsilon_o + b_{22}) u_l$. In the case of the presence of free charges, then the solution for the electric field will be the field without free charges plus the Coulomb field produced by the charge density in *vacuum* (charge alone without the lattice) which can be expressed as:

$$E_{vac}(R) = -\nabla \int \frac{\rho(R')}{|R - R'|} dR' \tag{4.17}$$

then the solution for Eq. (4.16) can be written as:

$$E = \frac{-b_{12}}{\varepsilon_o + b_{22}} u_l + \frac{E_{vac}}{\varepsilon_o + b_{22}} = \frac{-\omega_o}{\varepsilon_\infty} (\varepsilon_o - \varepsilon_\infty)^{1/2} u_l + \frac{1}{\varepsilon_\infty} E_{vac} \tag{4.18}$$

The total Hamiltonian for the system composed of the lattice motion and the free charges can be deduced form the system energy density

Reproduced with permission of the copyright owner. Further reproduction prohibited without permission.

consideration. Assuming the charge density is free charges then the Maxwell's equations can be written as follows:

$$\begin{aligned}
&\nabla.D=\nabla.(\varepsilon_o E+P)=-e_i\sum_i \delta(R-R_i)\\
&\nabla.H=0\\
&\nabla\times E=-\mu\dot{H}\\
&\nabla\times H=J+\dot{D}=\varepsilon_o\dot{E}+\dot{P}+\sum_i e_i\dot{R}_i\delta(R-R_i)
\end{aligned} \tag{4.19}$$

where *d* is the three dimensional Dirac delta function. Using the last two equation of Eq. (4.19):

$$\begin{aligned}
\nabla.(E\times H)&=(H.\nabla\times E-E.\nabla\times H)\\
&=-\mu H.\dot{H}-\varepsilon_o E.\dot{E}-E.\dot{P}-\sum_i e_i\dot{R}_i E.\,\delta(R-R_i)
\end{aligned} \tag{4.20}$$

Integrating over an arbitrary volume:

$$\begin{aligned}
&\int_v \nabla.(E\times H)dv=\int_s (E\times H)\\
&-\int_v\left[\mu H.\dot{H}+\varepsilon_o E.\dot{E}+E.\dot{P}+\sum_i e_i\dot{R}_i E.\,\delta(R-R_i)\right]dv
\end{aligned} \tag{4.21}$$

Note that integration over the volume was changed into integration over surface was made by use of Green's theorem. In addition, $E\times H$ is the pointing vector for electromagnetic energy flux; thus the left hand side of the equation represents the rate at which electromagnetic energy flows out of the volume.

The last term in the above equation can be written as:

$$\sum_i e_i\dot{R}_i E.\,\delta(R-R_i)=\sum_i e_i\dot{R}_i E(R_i) \tag{4.22}$$

Reproduced with permission of the copyright owner. Further reproduction prohibited without permission.

Using the equation of motion of charges :

$$m_i \ddot{R}_i = e_i E(R_i) \tag{4.23}$$

we find that:

$$-\frac{d}{dt}\left[\tfrac{1}{2} m_i \dot{R}_i^2\right] = -m_i \dot{R}_i . \ddot{R}_i = -e_i \dot{R}_i E(R_i) \tag{4.24}$$

Hence, the last term is equal to the rate of decrease in kinetic energy of charges within the volume. From the conservation of energy then:

$$\mu H . \dot{H} + \varepsilon_o E . \dot{E} + E . \dot{P} \tag{4.25}$$

must equal to the rate of change of energy density. If we denote the energy density by E_T then dE_T/dt must equal to the expression of Eq (4.25). With E_T expressed as:

$$E_T = \tfrac{1}{2}\dot{u} - \tfrac{1}{2} b_{11} u^2 - b_{12} u . E - \tfrac{1}{2} b_{22} E^2 + E . P + \tfrac{1}{2}\varepsilon_o E^2 + \tfrac{1}{2}\mu H^2 \tag{4.26}$$

then dE_T/dt can be written as:

$$\begin{aligned} \frac{dE_T}{dt} &= \dot{u}(\ddot{u} - b_{11} u - b_{12} E) + \\ &\quad \dot{E}(P - b_{12} u - b_{22} E) + E . \dot{P} + \varepsilon_o E . \dot{E} + \mu H . \dot{H} \end{aligned} \tag{4.27}$$

Note that the quantities in brackets vanish by Eqs. (4.3) and (4.4) and the remaining expression is exactly the expression given via Eq. (4.25).

Substituting for P from Eq. (4.4) into Eq. (4.26) and using the values given for the constants then Eq. (4.26) can be written as:

$$E_T = \tfrac{1}{2}\left(\dot{u}^2 + \omega_o^2 u^2\right) + \tfrac{1}{2}\varepsilon_\infty E^2 + \tfrac{1}{2}\mu H^2 \tag{4.28}$$

Reproduced with permission of the copyright owner. Further reproduction prohibited without permission.

The system total Hamiltonian is obtained by integrating the energy density over space and adding the kinetic energy of the free charges:

$$H_{sys} = \sum_i \tfrac{1}{2} m_i \dot{R}_i^2 + \int_v \left\{ \tfrac{1}{2}\left(\dot{u}^2 + \omega_o^2 u^2\right) + \tfrac{1}{2}\varepsilon_\infty E^2 + \tfrac{1}{2}\mu H^2 \right\} dv \qquad (4.29)$$

neglecting the radiation effects, the magnetic field may then be put to zero. Substituting for the electric field from Eq. (4.18) and for the displacement from Eq. (4.14), results in the following expression for the system Hamiltonian:

$$\begin{aligned} H_{sys} &= \sum_i \tfrac{1}{2} m_i \dot{R}_i^2 + \int_v \tfrac{1}{2\varepsilon_\infty} E_{vac}^2 dv + \\ &+ \int_v \tfrac{1}{2}\left\{\left(\dot{u}_t^2 + \omega_o^2 u_t^2\right) + \left(\dot{u}_l^2 + \tfrac{\varepsilon_o}{\varepsilon_\infty}\omega_o^2 u_l^2\right)\right\} dv \qquad (4.30) \\ &- \omega_l \left[\tfrac{1}{\varepsilon_\infty} - \tfrac{1}{\varepsilon_o}\right]^{1/2} \int_v u_l . E_{vac} dv \end{aligned}$$

where $\omega_l = \left(\varepsilon_o/\varepsilon_\infty\right)^{1/2}\omega_o$. The first two terms in the above Hamiltonian represent the charges in the medium. The first being the kinetic energy and the second being the charges Coulomb interaction and self energies. The third term represent the Hamiltonian of the lattice medium in the absence of free charges. The last term represent the interaction between the charges and lattice motion or the electron-phonon interaction. Hence the electron-phonon interaction Hamiltonian is given by:

$$H_{e-ph} = -\omega_l \left[\frac{1}{\varepsilon_\infty} - \frac{1}{\varepsilon_o}\right]^{1/2} \int_v u_l . E_{vac} dv \qquad (4.31)$$

By considering a three dimensional crystal lattice, and noting that $u_l(R,t) = u_l(R)e^{-i\omega t} + c.c.$ we can make a Fourier analysis of the coordinate $u_l(R)$ as:

Reproduced with permission of the copyright owner. Further reproduction prohibited without permission.

$$u_l(R) = \frac{1}{\sqrt{V}} \sum_q X(q) e^{iq.R} \tag{4.32}$$

where V is the volume of the crystal containing N unit cells. $X(q)$ is a normal coordinate operator which for a harmonic oscillator can be written in a standard way in terms of the annihilation and creation operators as:

$$\begin{aligned} X(q) &= \sqrt{\frac{\hbar}{2\omega_l(q)}}\left(a_q^{\dagger} + a_q\right) \\ a_q &\equiv \frac{i}{\sqrt{2\hbar\omega_l}} p_q + \sqrt{\frac{\omega_l}{2\hbar}} X(q) \\ a_q^{\dagger} &\equiv \frac{-i}{\sqrt{2\hbar\omega_l}} p_q^{\dagger} + \sqrt{\frac{\omega_l}{2\hbar}} X(q) \end{aligned} \tag{4.33}$$

where p_q is the moment operator.

Hence the interaction Hamiltonian can be written as:

$$H_{e-ph} = \sum_q \omega_l(q) \left[\frac{1}{\varepsilon_\infty} - \frac{1}{\varepsilon_o}\right]^{1/2} \sqrt{\frac{\hbar}{2\omega_l(q)V}} \int_v \left(a_q^{\dagger} e^{i\omega t} + a_q e^{-i\omega t}\right) e^{iq.R} . E_{vac} dv \tag{4.34}$$

In the following we will replace $\int E_{vac} dv$ generated by a single electron by its Fourier transform $2e\sqrt{\pi}\sum_q (1/q) e^{iq.R}$ and replace $e^{iq.R}$ by 1 since we are interested in electron-long wave optical phonon interactions for which the wave number is small, then the above Hamiltonian can be written as:

Reproduced with permission of the copyright owner. Further reproduction prohibited without permission.

$$H_{e-ph} = \sum_q \left\{ \left[\frac{1}{\varepsilon_\infty} - \frac{1}{\varepsilon_o} \right]^{1/2} \sqrt{\frac{2\pi e^2 \hbar \omega_l(q)}{Vq^2}} \right\} \left(a_q^\dagger e^{i\omega t} + a_q e^{-i\omega t} \right)$$
$$= \sum_q M(q) \left(a_q^\dagger e^{i\omega t} + a_q e^{-i\omega t} \right) \quad (4.35)$$

(for further information see references 9 and 10).

Considering for example a single electron interacting with a one dimensional, 1 mm long lattice (number of unit cells is then 1770) composed of GaAs atoms. Here $\varepsilon_\infty = 10.88$, $\varepsilon_o = 12.85$ and lattice constant $a = 5.65 \AA$. The dispersion relation connecting the phonon frequency ω and wave numbers q for a diatomic crystal is given by[11]:

$$\omega^4 - 2C\left(\frac{m_1 + m_2}{m_1 m_2}\right)\omega^2 + \frac{2C^2}{m_1 m_2}\left(1 - \cos(qa)\right) \quad (4.36)$$

where C is the force constant connecting the lattice atoms and the m_1 and m_2 are the atomic masses of the Ga and the As atoms. These are 1.14×10^{-25}kg and 1.227×10^{-25}kg respectively. With $\omega(q = 0) = 5.46 \times 10^{13} s^{-1}$ for GaAs LO phonons the force constant can then be readily evaluated and it is found to be $C = 88.1$ N/m By solving for the phonon frequency from Eq. (4.36) for all the wave numbers within the first Brillion zone boundaries the electron-phonon scattering matrix *M(q)* in Eq. (4.35) can then be evaluated.

Fig. (4.1) displays as a function of phonon wave numbers the LO phonon frequency In part (a) and the electron-phonon scattering matrix *M(q)* in part (b). Note that the scattering matrix reflects the strength of the electron-phonon coupling. Hence from Fig. (4.1b), it is clear that the electron-phonon coupling increases for smaller wave numbers.

Reproduced with permission of the copyright owner. Further reproduction prohibited without permission.

Using the above described model, the one dimensional (1-D) time-dependent Schrödinger's equation for a tunneling electron in a double barrier structure with electron-phonon interaction is given by:

$$i\hbar\frac{\partial\psi}{\partial t} = H_e\psi + \left(Ve^{-i\omega t} + V^{\dagger}e^{i\omega t}\right)\psi, \tag{4.37}$$

where ψ is the product of the electron and phonon wave functions. V and $V^{\dagger}$ are defined as:

$$V = \sum_q M(q)a_q \tag{4.38a}$$

and

$$V = \sum_q M^*(q)a_q^{\dagger} \tag{4.38b}$$

It is difficult to find the wave function directly from Eq.(4.37) since V and $V^{\dagger}$ contain the phonon wave vector dependent electron-phonon scattering matrix and number *operators* of a_q and $a_q^{\dagger}$. However, when the electron phonon interaction is limited such that (i) only electrons at the incident energy E can virtually emit (absorb) and then absorb (emit) phonons without net generation or absorption of phonons., and (ii) electrons can only be scattered to the $E \pm \hbar\omega$ states by real emission and absorption processes, then the wave function of the electron-phonon system at the incident energy E in the double barrier structure can be expressed as:

Reproduced with permission of the copyright owner. Further reproduction prohibited without permission.

$$\psi(z,t)=\left(1-\frac{VV^{\dagger}+V^{\dagger}V}{\hbar^2\omega^2}\right)\psi^{(0)}(z,t)|n\rangle+\frac{V}{\hbar\omega}\psi^{(1)}(z,t)|n\rangle$$
$$+\frac{V^{\dagger}}{\hbar\omega}\psi^{(2)}(z,t)|n\rangle, \tag{4.39}$$

where $|n\rangle$ is the phonon wave function describing a *single* phonon state. The $\psi^{(0)}(z,t)$, $\psi^{(1)}(z,t)$, and $\psi^{(2)}(z,t)$ are the electronic wave function components associated with the *single* phonon states $|n\rangle$, $|n-1\rangle$,and $|n+1\rangle$, respectively.

The tunneling process of an electron wave packet with the electron-phonon interaction included when the incident energy E is equal to the resonant energy E_r is illustrated in Fig. 4.2.

Substituting the wave function given in Eq.(4.39) into Eq.(4.37) and multiplying from the left by the phonon state $\langle n|$ and then averaging over the *phonon assembly*, the first component associated with $\psi^{(0)}(z,t)$ in Eq.(4.40) is obtained. Similarly, multiplying by the phonon states $\langle n-1|$, $\langle n+1|$ will result in the second and third component associated with $\psi^{(1)}(z,t)$, and $\psi^{(2)}(z,t)$ in Eq.(4.40), respectively:

$$i\hbar\frac{\partial}{\partial t}\begin{pmatrix}\psi^{(0)}(z,t)\\ \psi^{(1)}(z,t)\\ \psi^{(2)}(z,t)\end{pmatrix}=$$
$$\begin{pmatrix} H_e & \frac{\hbar\omega g n_q}{1-\xi}e^{i\omega t} & \frac{\hbar\omega g(n_q+1)}{1-\xi}e^{-i\omega t}\\ \hbar\omega(1-\xi)e^{-i\omega t} & H_e & 0\\ \hbar\omega(1-\xi)e^{i\omega t} & 0 & H_e\end{pmatrix}\begin{pmatrix}\psi^{(0)}(z,t)\\ \psi^{(1)}(z,t)\\ \psi^{(2)}(z,t)\end{pmatrix}, \tag{4.40}$$

Reproduced with permission of the copyright owner. Further reproduction prohibited without permission.

where $\xi = g(2n_q + 1)$ and g is the electron-phonon coupling constant. In Eq. (4.40) the average values of $VV^\dagger$ and $V^\dagger V$ over the phonon assembly were used and are given by:

$$\left\langle VV^\dagger \right\rangle = \sum_q |M(q)|^2 (n_q + 1), \qquad (4.41a)$$

$$\left\langle V^\dagger V \right\rangle = \sum_q |M(q)|^2 n_q, \qquad (4.41b)$$

and

$$g = \sum_q \left[|M(q)| / \hbar\omega \right]^2, \qquad (4.41c)$$

where $n_q = \left[exp(\hbar\omega / k_B T) - 1 \right]^{-1}$ is the phonon population.

The numerical solution of the time-dependent Schrödinger equation [Eq. (4.40)] is obtained by converting it into the following difference equation using the procedure outlined in chapter 2:

$$\frac{1}{m^*_{j+1} + m^*_j} \begin{pmatrix} \psi^{(0)}_{j+1,l+1} \\ \psi^{(1)}_{j+1,l+1} \\ \psi^{(2)}_{j+1,l+1} \end{pmatrix} -$$

$$\begin{pmatrix} -\eta_j & \frac{e^2}{\hbar} \frac{\omega g n_q}{1-\xi} e^{i\omega(l+1)} & \frac{e^2}{\hbar} \frac{\omega g (n_q + 1)}{1-\xi} e^{-i\omega(l+1)} \\ \frac{e^2 \omega}{\hbar} (1-\xi) e^{-i\omega(l+1)} & -\eta_j & 0 \\ \frac{e^2 \omega}{\hbar} (1-\xi) e^{i\omega(l+1)} & 0 & -\eta_j \end{pmatrix} \begin{pmatrix} \psi^{(0)}_{j,l+1} \\ \psi^{(1)}_{j,l+1} \\ \psi^{(2)}_{j,l+1} \end{pmatrix}$$

$$+ \frac{1}{m^*_{j-1} + m^*_j} \begin{pmatrix} \psi^{(0)}_{j-1,l+1} \\ \psi^{(1)}_{j-1,l+1} \\ \psi^{(2)}_{j-1,l+1} \end{pmatrix} + \frac{1}{m^*_{j+1} + m^*_j} \begin{pmatrix} \psi^{(0)}_{j+1,l} \\ \psi^{(1)}_{j+1,l} \\ \psi^{(2)}_{j+1,l} \end{pmatrix} + \frac{1}{m^*_{j-1} + m^*_j} \begin{pmatrix} \psi^{(0)}_{j-1,l} \\ \psi^{(1)}_{j-1,l} \\ \psi^{(2)}_{j-1,l} \end{pmatrix}$$

Reproduced with permission of the copyright owner. Further reproduction prohibited without permission.

$$+\begin{pmatrix} -\gamma_j & -\frac{\varepsilon^2}{\hbar}\frac{\omega g n_q}{(1-\xi)}e^{i\omega l} & -\frac{\varepsilon^2}{\hbar}\frac{\omega g(n_q+1)}{(1-\xi)}e^{-i\omega l} \\ -\frac{\varepsilon^2}{\hbar}\omega(1-\xi)e^{-i\omega l} & -\gamma_j & 0 \\ -\frac{\varepsilon^2}{\hbar}\omega(1-\xi)e^{i\omega l} & 0 & -\gamma_j \end{pmatrix}\begin{pmatrix}\psi_{j,l}^{(0)} \\ \psi_{j,l}^{(1)} \\ \psi_{j,l}^{(2)}\end{pmatrix} = 0 \tag{4.42}$$

where

$$\eta_j = \frac{2\varepsilon^2}{\hbar\delta}i - \frac{\varepsilon^2}{\hbar^2}V_{0j} - \frac{1}{m_{j+1}^* + m_j^*} - \frac{1}{m_{j-1}^* + m_j^*} \tag{4.43a}$$

and

$$\gamma_j = \frac{2\varepsilon^2}{\hbar\delta}i + \frac{\varepsilon^2}{\hbar^2}V_{0j} + \frac{1}{m_{j+1}^* + m_j^*} + \frac{1}{m_{j-1}^* + m_j^*}, \tag{4.43b}$$

$\delta(\varepsilon)$ and $l(j)$ are the time (space) interval and index, respectively.

The above three equations (Eq. (4.42)) for the three components of the electron wave function are coupled with each other through phonon emission and absorption. Each equation represents a complex tridiagonal matrix system. Each equation is converted into lower and upper diagonal matrices (see chapter 2). The forward and backward substitution along with Gaussian elimination to solve for the three coupled function at a particular space point j is then used to solve theses equations.

The 1-D current density (J) is calculated at the observation point z_0 to the right of the second barrier as indicated in Fig. 4.1. Substituting the wave function given in Eq. (4.39) into the quantum mechanical

Reproduced with permission of the copyright owner. Further reproduction prohibited without permission.

current density expression and averaging over the phonon assembly, the total electron current density observed at point z_0 is given by:

$$J = \left\{1 - \left[g(n_q + 1) + g n_q\right]\right\}^2 J_0 + g n_q J_1 + g(n_q + 1) J_2, \qquad (4.44)$$

where

$$J_k = \frac{\hbar}{2m^* i}\left(\psi^{(k)*}\frac{\partial \psi^{(k)}}{\partial z} - \frac{\partial \psi^{(k)*}}{\partial z}\psi^{(k)}\right), \qquad (4.45)$$

with k=0, 1, 2.

For the calculation in this chapter, a Gaussian electron wave packet was used as the initial electron wave function with a central kinetic energy equal to the ground state resonant energy of the double barrier structure.

4.3 Results and Discussion

The calculated 1-D resonant current density temporal profiles are shown in Fig. 4.3 by the solid curve for no phonon coupling, g=0.0, the dotted curve for g=0.1 and T=300 K, and the dashed curve for g=0.1 and T=0 K.

Let me discuss theses curves, starting with the discussion of the solid curve in Fig. 4.3 which represent the *elastic* (coherent) resonant tunneling current density at channel E_r. The current reaches a maximum value at 300 fs after the excitation of the electron wave packet at the left lead of the structure. This resonant tunneling time is

Reproduced with permission of the copyright owner. Further reproduction prohibited without permission.

determined by four factors: (i) how far the packet is placed away from the left barrier in the left lead, (ii) the structure dimensions, (iii) how far the observation point is from the right barrier, and (iv) what the central kinetic energy of the wave packet is. The value of 300 fs implies an average electron traveling speed of 6×10^7 cm/sec which is consistent with the speed calculated using the central kinetic energy of 90 meV indicating coherent tunneling nature. The current density decreases once the wave packet passes the observation point z_0 and decays exponentially with a time constant of 320 fs. The dashed curve in Fig. 4.3 reflects the *net loss* of tunneling current observed at z_0 due to inelastic scattering at zero temperature. The maximum value of the current density decreases further at 300 K as shown by the dotted curve in Fig. 4.3 because both real emission and absorption are allowed. It should be noted that the effect on transit time through the double barrier structure in the presence of phonons is negligible which is attributed to the fact that tunneling time is primarily determined by the width of the energy level which the electron wave packet is tunneling through.

In Fig. 4.4 the calculated temperature dependence of the peak current density ratio $\{J(T)/J(10K)\}$ is shown by the solid curve. As can be seen, the peak current density remains almost constant over the temperature range 0-100 K. However, as the temperature is increased further, the scattering processes increase and the tunneling current density starts to decrease. For comparison, the measured data by Bar-Joseph *et al.*[12] are shown by the stars in Fig. (4.4) The thermionic contribution for the current density predicted by theory[13] is subtracted

Reproduced with permission of the copyright owner. Further reproduction prohibited without permission.

from the data point at 300 K. The thermionic contribution for the other data points in negligible. It is clear that both calculated and measured peak current density decreases as the temperature increases. The difference in the magnitude of measured and calculated data may be due to the fact that my model considers only plane-wave phonons, while in reality the confined, interface and acoustic phonons should be taken into account.

It should be pointed out that the use of the value g=0.1 is just for demonstrational purposes. The magnitude of phonon-assisted tunneling is smaller for smaller vales of g.[5] The used value of g in my calculations may be over estimated for GaAs/$Al_xGa_{1-x}As$ structures but it may be appropriate for II-VI compound based structures.[4] Finally it should be emphasized that my approach can be used to study the phonon-assisted tunneling dynamics associated with various phonon modes (as will be shown in chapter 5) since the realistic electron-phonon scattering matrix can be taken care of.

Reproduced with permission of the copyright owner. Further reproduction prohibited without permission.

4.4 References

1. V. J. Goldman, D. C. Tsui, and J. E. Cunningham, Phys. Rev. B **36**, 7635 (1987).
2. B. Y. Gelfand, S. Schmitt-Rink, and A. F. J. Levi, Phys. Rev. Lett. **62**, 1683 (1989).
3. N. S. Wingreen, K. W. Jacoobson, and J. W. Wilkins, Phys. Rev. Lett. **61**, 1396 (1988).
4. W. Cai, T. F. Zheng, P. Hu, B. Yudanin, and M. Lax, Phys. Rev. Lett. **63**, 418 (1989).
5. S. Collins, D. Lowe, and J. R. Barker, J. Phys. C **20**, 6233 (1987).
6. H. Gou, K. Diff, G. Neofotistos, and J. Gunton, Appl. Phys. Lett. **53**, 131 (1988).
7. A. P. Jauho and M. Johnson, Superlatt. Microstruct. **6**, 303 (1989).
8. A. P. Jauho, Phyd. Rev. B, **41**, 12327 (1990).
9. M. Born and K. Huang, *Dynamical Theory of Crystal lattices,* (1985) pages (82-100).
10. G. Srivastiva, *The Physics of Phonons,* (1990), chapter 4.
11. C. Kittle, *Introduction to Solid State Physics,* 6th ed. (1986) Chap. 4.
12. I. Bar-Joseph, Y. Gedalyahu, A. Yacoby, T. Woodward, D. Shemla, D. Sivco, and A. Cho, Phys. Rev. B **44**, 8361 (1991).
13. S. Sze, *Physics of Semiconductors* (Wiley, New York, 1981), p. 256.

Reproduced with permission of the copyright owner. Further reproduction prohibited without permission.

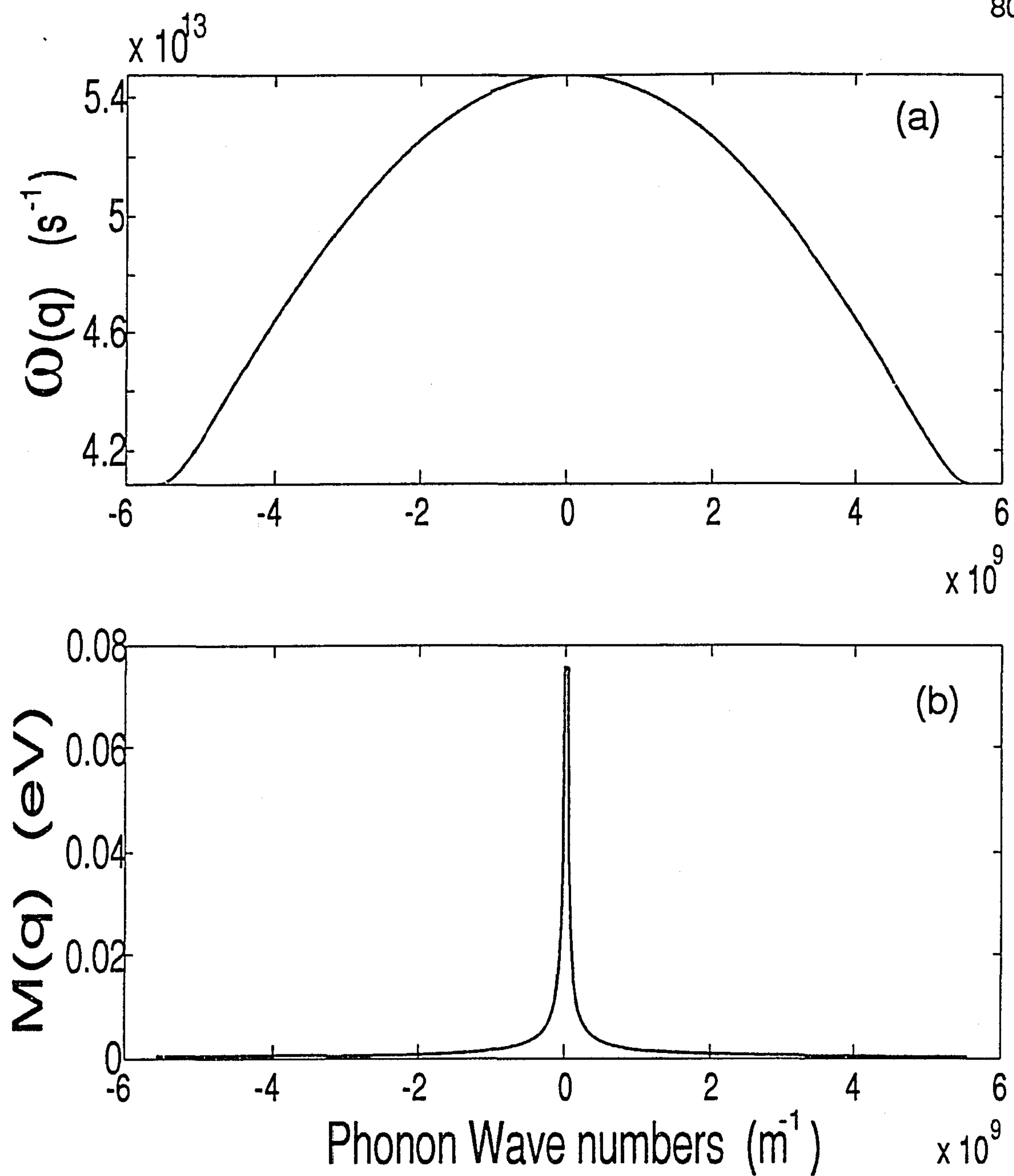

Fig. (4.1) (a) The LO-phonon frequency versus wave numbers dispersion relation. (b) THe electron-LO phonon scattering matrix as a function of phonon wave numbers.

Reproduced with permission of the copyright owner. Further reproduction prohibited without permission.

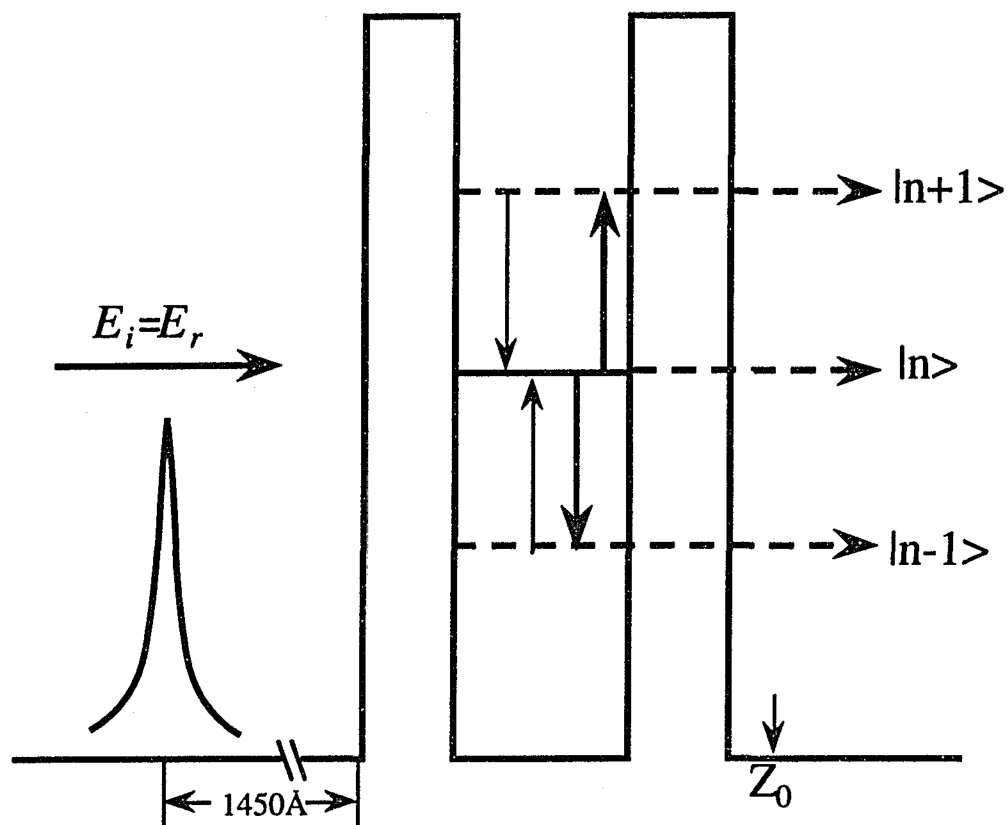

Fig. 4.2 Tunneling current components in a double barrier structure in the presence of electron-phonon interaction. The double barrier structure consists of a 45Å quantum well and two 28Å barriers of 280 meV potential.

Reproduced with permission of the copyright owner. Further reproduction prohibited without permission.

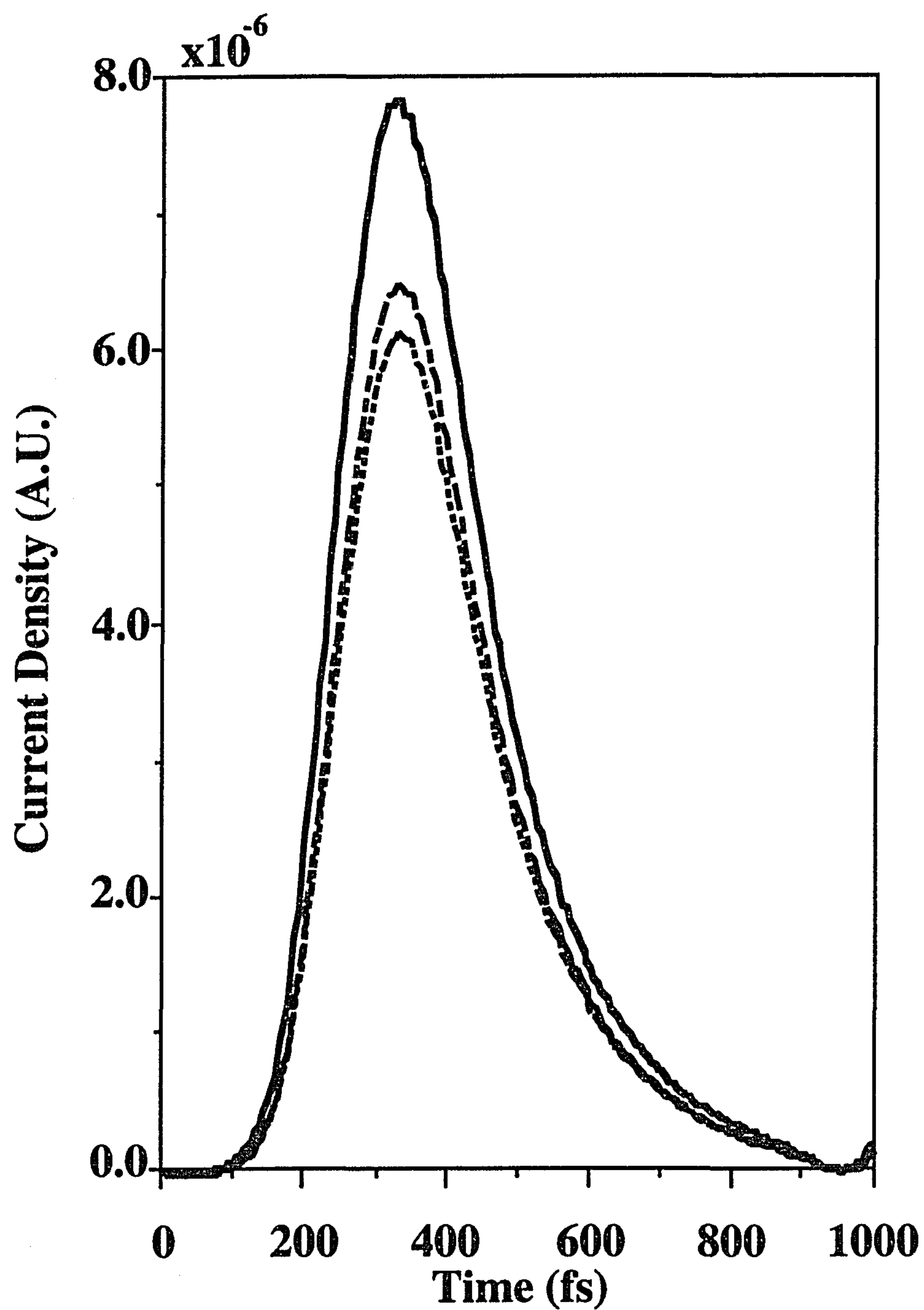

Fig. 4.3 Temporal behavior of the 1D resonant tunneling current density for the different conditions: (i) the solid curve for coupling constant g=0.0, (ii) the dotted curve for g=0.1 and T=300 K, and (iii) the dashed curve for g=0.1 and T=0 K.

Reproduced with permission of the copyright owner. Further reproduction prohibited without permission.

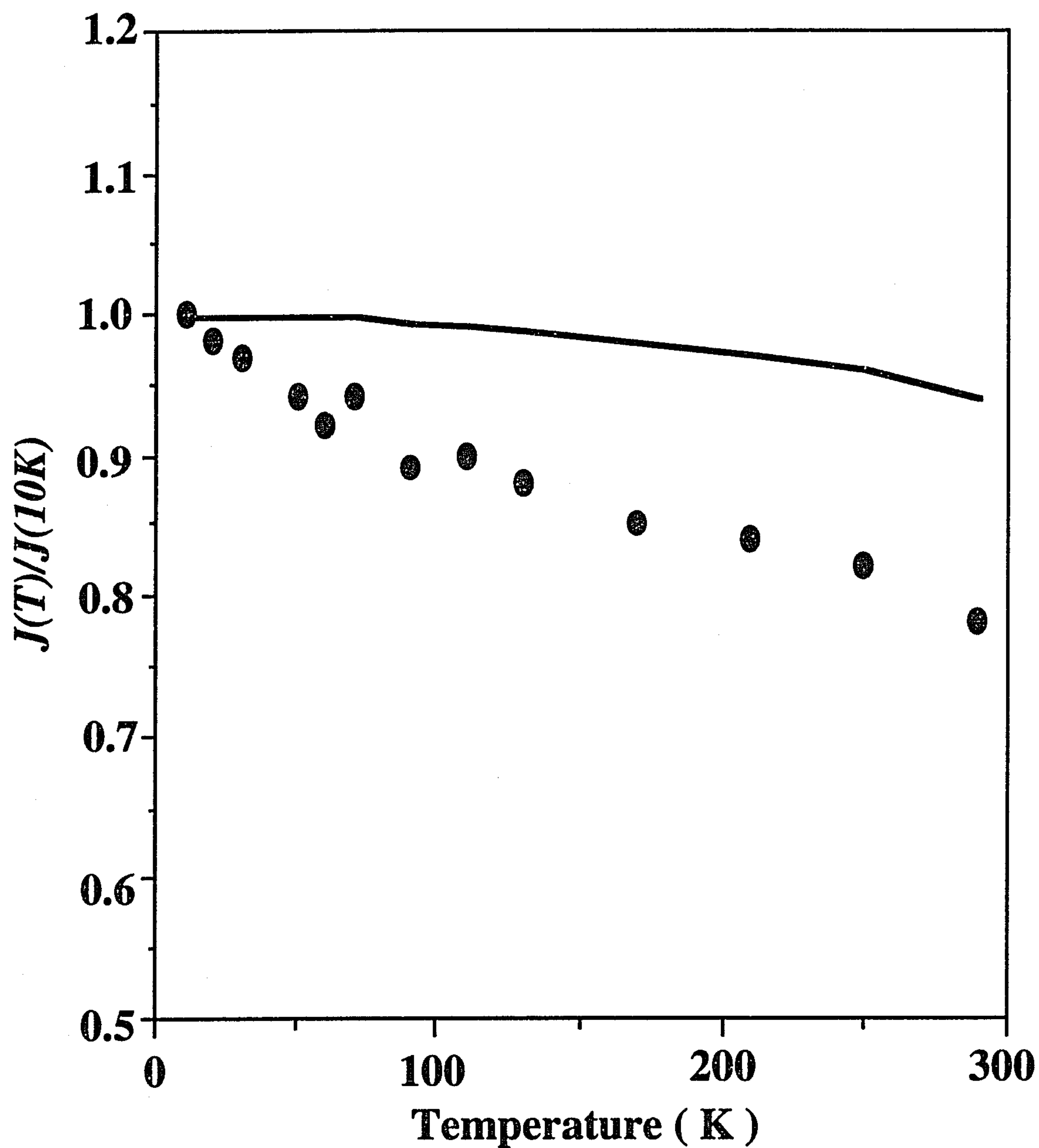

Fig. 4.4 The temperature dependence of the tunneling current density peak ratio $J(T)/J(10K)$. The solid curve is calculated by the model described in the text. The solid circles indicate the experimental data.

Reproduced with permission of the copyright owner. Further reproduction prohibited without permission.

CHAPTER FIVE

ULTRAFAST CHARGING DYNAMICS IN A DOUBLE BARRIER STRUCTURE IN THE PRESENCE OF LOCALIZED PHONON MODES

5.1 Introduction

Solid state surfaces and interfaces between two media are connected with a variety of interesting phenomena. On one hand, their existence results in a completely novel effects and, on the other hand, the properties of the bulk are changed. Double hetrostructures are important for a large field of semiconductor devices. Electron-LO phonons which are accompanied by macroscopic electric fields, couple to electrons in theses structures. The interfaces of the system alter the spectrum of the LO phonons of the bulk case. First, the properties of the bulk LO phonons are changed by the scattered and reflected waves. Second, new states in the spectrum of the LO phonons occur: interface phonons. The electrons interact with both, LO and interface phonons. While a great deal of work has examined the electron-phonon interaction in layered materials, using different phonon modes[1], little has focused on the *dynamics* of electron tunneling in a double barrier structure in the presence of localized phonon modes (symmetrical interface, antisymmetrical interface and confined phonon modes). Turely[2] studied in the steady state case the effect of localized phonon

Reproduced with permission of the copyright owner. Further reproduction prohibited without permission.

modes on electron tunneling current in a double barrier structure and showed that phonon assisted tunneling is primarily caused by two types of localized phonon modes: confined phonons in the quantum well and symmetrical interface phonons.

In the last chapter, I discussed the effect of electron-plane wave LO phonon interaction on the dynamics of electron tunneling through a double barrier structure. In this chapter, I will extend this subject of the last chapter to investigate the effect of electron-localized phonon modes interaction on the charge build-up (see chapter two) dynamics inside the quantum well of a double barrier structure. I well show that the probability of finding the electron inside the quantum well is reduced due to confined and symmetric interface phonon modes, while the effect of antisymmetric interface phonon modes is negligible. I will also show that the charge build-up time inside the quantum well is not affected by any of these phonon modes. The results of phonon assisted charge build-up when an electron wave packet is incident at the energy channels $E_r \pm \hbar\omega$ are also presented.

5.2 Localized Phonon Modes Dispersion Relations

The coupling function of a single electron to the long-wave length optical phonons of a multilayer system or the electron-phonon scattering matrix is given by:[3,4]

Reproduced with permission of the copyright owner. Further reproduction prohibited without permission.

$$\Gamma_j(q_\parallel, z) = -\frac{i}{q_\parallel}\left(\frac{\varepsilon_0 e^2 \hbar}{2A\omega_j(q_\parallel)}\right)^{1/2} E_\parallel^j(q_\parallel, z). \tag{5.1}$$

This function describes the coupling strength of a single electron at the position z with the j-th LO phonon mode in the layered structure which has the dispersion relation $\omega_j(q_\parallel)$. $E_\parallel^j(q_\parallel, z)$ denotes the longitudinal part of the electric field connected with the j-th LO phonon mode. A is the cross sectional area in the x-y plane. For the nonzero components of the monochromatic electric field we use the two-dimensional Fourier series:

$$E^j(\boldsymbol{x}, t) = \frac{1}{A}\sum_{q_\parallel} e^{i(q_\parallel x_\parallel - \omega t)} E^j(q_\parallel, z). \tag{5.2}$$

where $\boldsymbol{x}$ is a vector in the direction perpendicular to z.

Since the long-wave optical phonons are macroscopic normal modes, the lattice dynamical properties of the media of the double barrier structure are completely described by its macroscopic dielectric function which I assume to be:

$$\varepsilon_\nu(\omega) = \varepsilon_{\infty\nu}\frac{\omega_{L\nu}^2 - \omega^2}{\omega_{T\nu}^2 - \omega^2}, \tag{5.3}$$

where ν=1,2 denotes the barrier or the quantum well material of the double barrier structure. $\varepsilon_{\infty\nu}$ is the high frequency optical dielectric constant, $\omega_{L\nu}$, and $\omega_{T\nu}$ are the longitudinal and transverse optical (LO and TO) phonon frequency, respectively. In the following I will describe each of the localized phonon modes in some detail.

Reproduced with permission of the copyright owner. Further reproduction prohibited without permission.

5.2.1 Interface Phonon Modes

The interface phonons discussed here are long-wave optical phonons which owe their existence to the presence of the interfaces of the double barrier structure. Their electromagnetic fields are localized at the interfaces of the two materials forming the double barrier structure and the field magnitude decay exponentially from the interfaces. Therefore, we find with the boundary conditions $E(q_{\|}, z)\Big|_{z=\pm\infty} = 0$ from Maxwell's equations for the longitudinal part of the electric field:

$$E^{s}_{\| I}(q_{\|}, z) = iC^{s}_{I}\begin{cases} D^{s}_{0}\, e^{-q_{\|}(z-a)} & z > a, \\ \left[A^{s}_{1}\, e^{q_{\|}z} - B^{s}_{1}\, e^{-q_{\|}z}\right]; & a > z > 0 \\ D^{s}_{2}\, e^{q_{\|}z}; & 0 > z. \end{cases} \tag{5.4}$$

where C^{s}_{I} is a normalization constant, I denotes the interface phonons, and s is the index of the different interface phonon modes. By requiring $E^{s}_{\| I}(q_{\|}, z)$ and $\varepsilon_{\nu}(\omega)dE^{s}_{\| I}(q_{\|}, z)/dz$ to be continuous across the interfaces at z=0, a and obtain

$$(\varepsilon_1 + \varepsilon_2)^2 - (\varepsilon_1 - \varepsilon_2)^2 \gamma^2 = 0 \tag{5.5}$$

with

$$\gamma = e^{-q_{\|}a}. \tag{5.6}$$

For the field amplitudes in Eq. (5.4) we find:

Reproduced with permission of the copyright owner. Further reproduction prohibited without permission.

$$
\begin{aligned}
D_0^s &= -1, \\
A_1^s &= \frac{\varepsilon_2 - \varepsilon_1}{2\varepsilon_1}\gamma, \\
B_1^s &= \frac{\varepsilon_2 + \varepsilon_1}{2\varepsilon_1}\gamma^{-1}, \\
D_2^s &= \frac{\varepsilon_2 + \varepsilon_1}{\varepsilon_2 - \varepsilon_1}\gamma^{-1}.
\end{aligned}
\tag{5.7}
$$

due to the symmetry of the double barrier structure, the dispersion relation (5.5) of the interface phonons is split into two different ones, one for the so-called antisymmetric interface phonon modes and one for the antisymmetric interface phonon modes by rewriting that equation in the following format:

$$
\gamma = \pm\frac{\varepsilon_1(\omega) + \varepsilon_2(\omega)}{\varepsilon_1(\omega) - \varepsilon_2(\omega)}. \tag{5.8}
$$

For the *antisymmetric interface phonon modes* the positive root applies and the dispersion is:

$$
\varepsilon_1(\omega) + \varepsilon_2(\omega)\frac{1-\gamma}{1+\gamma} = 0. \tag{5.9}
$$

With the use of the dielectric function given via Eq. (5.3) the explicit interface antisymmetric dispersion relation follows:

$$
\begin{aligned}
\omega_{A\pm}(q_{\parallel}) = \Bigg\{ &\frac{1}{2\left(\varepsilon_1^A + \varepsilon_2^A\right)}\Big(\varepsilon_1^A\left(\omega_{L1}^2 + \omega_{T2}^2\right) + \varepsilon_2^A\left(\omega_{L2}^2 + \omega_{T1}^2\right) \\
&\pm\Big[\varepsilon_1^A\left(\omega_{L1}^2 + \omega_{T2}^2\right) + \varepsilon_2^A\left(\omega_{L2}^2 + \omega_{T1}^2\right)\Big)^2 - \\
&4\left(\varepsilon_1^A + \varepsilon_2^A\right)\left(\varepsilon_1^A\omega_{L1}^2\omega_{T2}^2 + \varepsilon_2^A\omega_{L2}^2\omega_{T1}^2\right)\Big]^{1/2}\ \Big)\Bigg\}^{1/2}
\end{aligned}
\tag{5.10}
$$

Reproduced with permission of the copyright owner. Further reproduction prohibited without permission.

with

$$\varepsilon_1^A = \varepsilon_{\infty 1}(1+\gamma), \tag{5.11a}$$

$$\varepsilon_2^A = \varepsilon_{\infty 2}(1-\gamma). \tag{5.11b}$$

with theses relations in mind, the field amplitudes in Eq. (5.7) for the antisymmetric phonon modes become:

$$\begin{aligned} D_0^A &= -1, \\ A_1^A &= -\frac{\gamma}{1-\gamma}, \\ B_1^A &= -\frac{1}{1-\gamma}, \\ D_2^A &= 1, \end{aligned} \tag{5.12}$$

and the normalization constant becomes:

$$C_1^{A\pm} = \left\{ \frac{q_{\parallel}(1-\gamma)}{2\varepsilon_0^2} \times \left(\frac{\left(\omega_{T1}^2 - \omega_{A\pm}^2(q_{\parallel})\right)^2 \left(\omega_{T2}^2 - \omega_{A\pm}^2(q_{\parallel})\right)^2}{\varepsilon_1^A\left(\omega_{L1}^2 - \omega_{T1}^2\right)\left(\omega_{T2}^2 - \omega_{A\pm}^2(q_{\parallel})\right)^2 + \varepsilon_2^A\left(\omega_{L2}^2 - \omega_{T2}^2\right)\left(\omega_{T1}^2 - \omega_{A\pm}^2(q_{\parallel})\right)^2} \right) \right\}^{1/2}. \tag{5.13}$$

The coupling function of a single electron and the antisymmetric phonons of the double barrier structure is found using the pervious analysis:

Reproduced with permission of the copyright owner. Further reproduction prohibited without permission.

$$\Gamma_I^{A\pm}(q_\parallel, z) = -\left(\frac{\varepsilon_0 e^2 \hbar}{2A\omega_{A\pm}(q_\parallel)}\right)^{1/2} \times$$

$$\begin{cases} e^{-q_\parallel(z-a)}; & z > a \\ \dfrac{1}{1-\gamma}\left[\gamma e^{q_\parallel z} - e^{-q_\parallel z}\right]; & a > z > 0 \\ -e^{-q_\parallel z}; & 0 > z \end{cases} \tag{5.14}$$

For the symmetric interface phonon modes:

$$\varepsilon_1(\omega) + \varepsilon_2(\omega)\frac{1+\gamma}{1-\gamma} = 0. \tag{5.15}$$

Using the dielectric function given in Eq. (5.3), the symmetric interface phonon modes dispersion relation is as follows:

$$\omega_{s\pm}(q_\parallel) = \left\{\frac{1}{2\left(\varepsilon_1^s + \varepsilon_2^s\right)}\left(\varepsilon_1^s\left(\omega_{L1}^2 + \omega_{T2}^2\right) + \varepsilon_2^s\left(\omega_{L2}^2 + \omega_{T1}^2\right) \pm \right.\right.$$
$$\left[\left(\varepsilon_1^s\left(\omega_{L1}^2 + \omega_{T2}^2\right) + \varepsilon_2^s\left(\omega_{L2}^2 + \omega_{T1}^2\right)\right)^2\right. \tag{5.16}$$
$$\left.\left.\left. -4\left(\varepsilon_1^s + \varepsilon_2^s\right)\left(\varepsilon_1^s \omega_{L1}^2 \omega_{T1}^2 + \varepsilon_2^s \omega_{L2}^2 \omega_{T1}^2\right)\right]^{1/2}\right)\right\}^{1/2}$$

with

$$\varepsilon_1^s = \varepsilon_{\infty 1}(1-\gamma), \tag{5.17a}$$

$$\varepsilon_2^s = \varepsilon_{\infty 2}(1+\gamma), \tag{5.17b}$$

The field amplitudes and normalization constant are respectively:

Reproduced with permission of the copyright owner. Further reproduction prohibited without permission.

$$D_0^s = -1,$$
$$A_1^s = -\frac{\gamma}{1+\gamma},$$
$$B_1^s = \frac{1}{1+\gamma},$$
$$D_2^s = -1, \tag{5.18}$$

$$C_I^{s\pm} = \left\{ \frac{q_{\parallel}(1+\gamma)}{2\varepsilon_0^2} \times \left(\frac{\left(\omega_{T1}^2 - \omega_{s\pm}^2(q_{\parallel})\right)^2 \left(\omega_{T2}^2 - \omega_{s\pm}^2(q_{\parallel})\right)^2}{\varepsilon_1^s\left(\omega_{L1}^2 - \omega_{T1}^2\right)\left(\omega_{T2}^2 - \omega_{s\pm}^2(q_{\parallel})\right)^2 + \varepsilon_2^s\left(\omega_{L2}^2 - \omega_{T2}^2\right)\left(\omega_{T1}^2 - \omega_{s\pm}^2(q_{\parallel})\right)^2} \right) \right\}^{1/2}. \tag{5.19}$$

The coupling function of a single electron with the symmetric interface phonon modes is obtained as follows:

$$\Gamma_I^{s\pm}(q_{\parallel}, z) = -\left(\frac{\varepsilon_0 e^2 \hbar}{2A\omega_{s\pm}(q_{\parallel})} \right)^{1/2} \frac{C_I^{s\pm}}{q_{\parallel}} \times \begin{cases} e^{-q_{\parallel}(z-a)}; & z > a \\ \frac{1}{1-\gamma}\left[\gamma e^{q_{\parallel}z} - e^{-q_{\parallel}z}\right]; & a > z > 0 \\ -e^{q_{\parallel}z}; & 0 > z. \end{cases} \tag{5.20}$$

5.2.2 Confined Phonon Modes

Besides the interface phonon modes discussed above, there exist also in the spectrum of the long-wave optical phonons what is called the confined LO optical phonon modes. These phonon modes occur only at those frequencies where the lattice dielectric functions of the two semiconductor materials forming the double barrier structure vanish.

Reproduced with permission of the copyright owner. Further reproduction prohibited without permission.

Following the same procedure, the coupling function of an electron with confined phonon modes in the quantum well area can be written as:

$$\Gamma_{L1}^{m}(q_{\|},z) = -\left(\frac{e^2\hbar\omega_{L2}}{Aa\varepsilon_0}\left(\frac{1}{\varepsilon_{\infty 1}} - \frac{1}{\varepsilon_{s1}}\right)\right)^{1/2} \begin{cases} 0; & z > a \\ \dfrac{\sin\left(q_{\perp}^{m} z\right)}{\sqrt{q_{\|}^2 + \left(q_{\perp}^{m}\right)^2}}; & a > z > 0 \\ 0; & 0 > z, \end{cases} \tag{5.21}$$

with

$$q_{\perp}^{m} = \frac{\pi}{a} m; \qquad m = 1, 2, 3, \ldots . \tag{5.22}$$

and

$$\varepsilon_{s1} = \varepsilon_{\infty 1}\left(\omega_{L1}/\omega_{T1}\right)^2 \tag{5.23}$$

In Fig. (5.1) the spatial dependence of the coupling function of the electron of the electron-interface and electron-confined phonon modes is displayed. Fig. (5.1) was obtained using the following values for the material constants of GaAs:

$$\varepsilon_{\infty 1} = 10.90, \qquad \omega_{L1} = 5.496\times 10^{13} s^{-1}, \qquad \omega_{T1} = 5.057\times 10^{13} s^{-1}$$

and for AlGaAs

$$\varepsilon_{\infty 2} = 10.22, \qquad \omega_{L2} = 6.979\times 10^{13} s^{-1}, \qquad \omega_{T2} = 6.731\times 10^{13} s^{-1}$$

One last thing to mention is that the above mentioned electron-phonon coupling matrices are valid only within the quantum well region and the two barriers. In the investigation to follow I will limit the electron-phonon scattering to these regions only. The regions of the left

Reproduced with permission of the copyright owner. Further reproduction prohibited without permission.

and right lead of the double barrier structure will be electron-phonon scattering free.

5.3 Theory

The theory of electron tunneling through a double barrier structure in the presence of localized phonon modes (interface and confined) follows the same theory developed in chapter four for the electron tunneling in a double barrier structure in the presence of plane wave phonon modes.

The selected structure consists of a 45-Å quantum well sandwiched between two 28-Å GaAs/$Al_{0.3}Ga_{0.7}As$ barriers. A Gaussian wave packet with a central kinetic energy equal to the quasi-bound state energy of the double barrier quantum well was used as the initial wave function

The probability of finding the electron inside the quantum well of the double barrier structure is calculated via:

$$p(t) = \int_0^a \psi(z,t)\psi^*(z,t)dz. \tag{5.24}$$

Using the wave function given in Eq. (4. 23) and averaging over the phonon population, the above probability can be written as:

$$p(t) = \int_0^a \left[\left(1 - g(z)(2n_q + 1)\right)^2 \left|\psi^{(0)}\right|^2 + g(z)n_q\left|\psi^{(1)}\right|^2 + g(z)(n_q + 1)\left|\psi^{(2)}\right|^2 \right] dz$$

Reproduced with permission of the copyright owner. Further reproduction prohibited without permission.

(5.25)

where the function $g(z)$ is the electron-phonon coupling factor and is given by:

$$g(z)=\sum_q\left(\frac{|\Gamma(q,z)|}{\hbar\omega}\right)^2\rightarrow\frac{A}{(2\pi)^2}\int\left(\frac{|\Gamma(q,z)|}{\hbar\omega}\right)^2 d^2q. \tag{5.26}$$

The summation in the above equation over the wave vector q is limited by the continuum approximation and should be performed up to the limit $|q|<|q_c|$ where q_c is the cutoff wave vector of the continuum approximation, which is about 10^8 m^{-1}.

5.4 Results and Discussion

The probability of finding the electron inside the quantum well of a double barrier structure is a direct measure of the electron density inside the well. The probability is enhanced when the electron wave packet is incident E energy matches the resonant energy E_r. A substantial fraction of the wave packet can tunnel through the barriers on resonance. The probability $p(t)$ is shown as the solid curve at resonance in Fig. (5.2) in the absence of the electron-phonon interaction After the initial build-up time (some times defined as charging time, which is the time period from when the wave packet inters the first barrier until the probability reaches a maximum), which is about 330 fs for the double barrier structure used in our calculations, the probability $p(t)$ reaches a maximum and then decays exponentially with a time constant of 850 fs.

Reproduced with permission of the copyright owner. Further reproduction prohibited without permission.

The dashed, dot dashed, dotted curves in Fig. (5.2) show the temporal profiles of $p(t)$ when the electron is allowed to interact with interface antisymmetric, interface symmetric and confined phonon modes at room temperature, respectively.

It is clear from Fig. (5.2) that the effect of interface antisymmetric phonon mode on the probability is negligible. The reason for this is that the initial (at E_r) and final electron states (at $E_r + \hbar\omega$ or $E_r - \hbar\omega$) have the same parity resulting in a weak electron-phonon coupling. On the other hand, the initial and final electronic states are approximately symmetric with respect to the GaAs quantum well center, this implies that localized phonon modes with electrostatic potential that is symmetric with respect to the center of the quantum well center are most likely to be emitted, and hence the more pronounced effect by the symmetric interface and confined phonon modes on the tunneling probability. The decrease of the electron probability density in the quantum well when the electron interacts with symmetric and confined phonon modes is attributed to an increase in the reflected charge in the left lead of the double barrier structure, since the electron-phonon coupling will include non resonant states.

The phonon assisted charge build-up when incident energy is at $E_r + \hbar\omega\,(E_r - \hbar\omega)$ at room temperature is shown by the solid (dashed) curve in Fig. (5.3).The solid curve represents carriers incident at one phonon energy over the resonant energy. After crossing the first barrier and while tunneling through the quantum well, a phonon is emitted and the carrier continue tunneling to the second barrier and to the continuum through the quasi-bound state. The dashed curve is

Reproduced with permission of the copyright owner. Further reproduction prohibited without permission.

similar to the solid curve with carriers incident at one phonon energy below the resonant energy. After the tunneling through the first barrier a phonon is absorbed and tunneling is continued to the second barrier through the quasi-bound state. It is noticed that from this figure (5.3) that the room temperature phonon assisted charge build-up is about two orders of magnitude smaller than the charge build up when the electron wave packet is incident the resonant energy (Fig. (5.2)). Moreover, the charge build-up time when the incident energy is at $E_r + \hbar\omega$ is shorter than build-up time when the packet is incident with $E_r - \hbar\omega$ energy. That is due to the fact that tunneling at the $E_r + \hbar\omega$ is faster through the double barrier structure. The association of the phonon operators V ($V^\dagger$) with the oscillating factor $e^{-i\omega t}\left(e^{i\omega t}\right)$ are responsible for the modulations that appear on the phonon assisted charge build-up curves (not clear on the solid curve because the modulations are small).

It should be mentioned that the symmetric interface phonon mode considered here is the inner symmetric mode which in which the electrostatic potential peaks at the interface between the quantum well and the barriers. The other type of the symmetric phonon mode is called the outer symmetric phonon mode for which the electrostatic potential peaks at the interface between the emitter/collector layers of the double barrier structure. The outer symmetric interface phonon mode has a negligible effect on the dynamics of the resonant tunneling since electronic wave function does not extend very far into the barriers and it would be expected that outer symmetric phonons will not strongly couple to the electronic states.

Reproduced with permission of the copyright owner. Further reproduction prohibited without permission.

The magnitude of the phonon-assisted charge build-up is affected by the electron-phonon coupling factor $g(z)$ which is characterized by its maximum value g_{max}. A larger value of g_{max}. implies a lager magnitude of the phonon assisted charge build-up. The value of g_{max}. versus quantum well width is plotted in Fig. (5.4) as the solid, dashed and dot-dashed curves for confined, inner interface symmetric and inner interface antisymmetric phonon modes, respectively. It is clear from this figure that inner symmetric interface phonon modes dominate when the quantum well width approaches the zero, while confined phonon modes dominate for moderate quantum well widths (about 40-Å). On the other hand, the interface antisymmetric phonons have small effect for all quantum well widths. As the quantum well increases, the value of g_{max}. for confined (interface) phonon modes decreases toward a constant value of 0.012 (0.021).

Reproduced with permission of the copyright owner. Further reproduction prohibited without permission.

5.5 REFERENCES

1) H. Rucher, E. Molinari and P. Lugli, Phys. Rev. B, **44**, 3463 (1991)

2) P. J. Turely and S. Teitsworth, J. Appl. Phys. **72**, (6) 2356 (1992)

3) L. Wendler and R. Pechstedt, Phys. stat. Sol. (b) **141**, 129 (1987)

4) L. Wendler, Phys. Stat. Sol. (b) **129**, 513 (1985).

Reproduced with permission of the copyright owner. Further reproduction prohibited without permission.

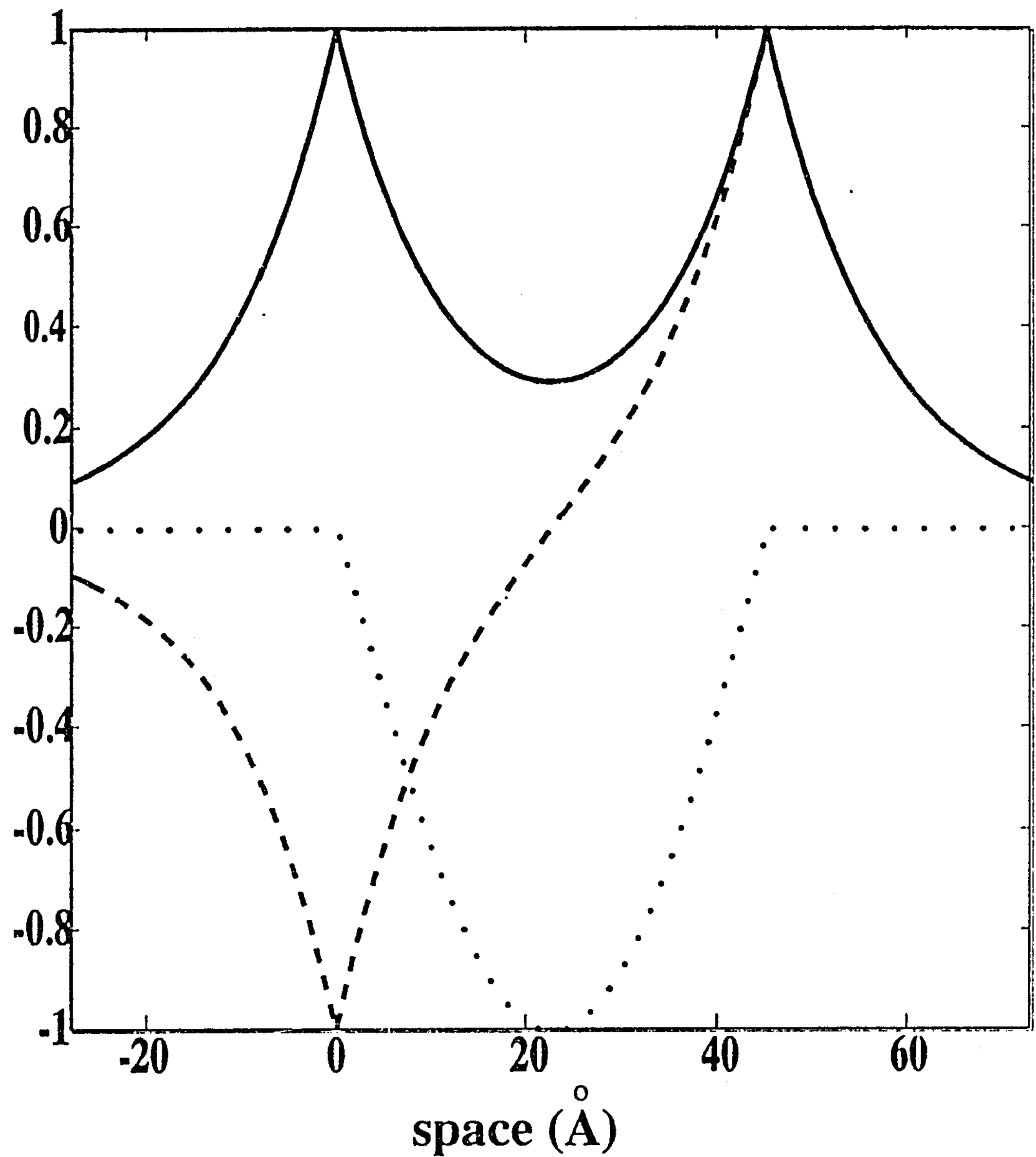

Fig. 5.1 The spatial dependence of the localizec phonon modes electrostatic potential. Solid curve represent the interface antisymmetric phonon modes. The dashe (dotted) represent the interface symmetric (confined) phonon modes.

Reproduced with permission of the copyright owner. Further reproduction prohibited without permission.

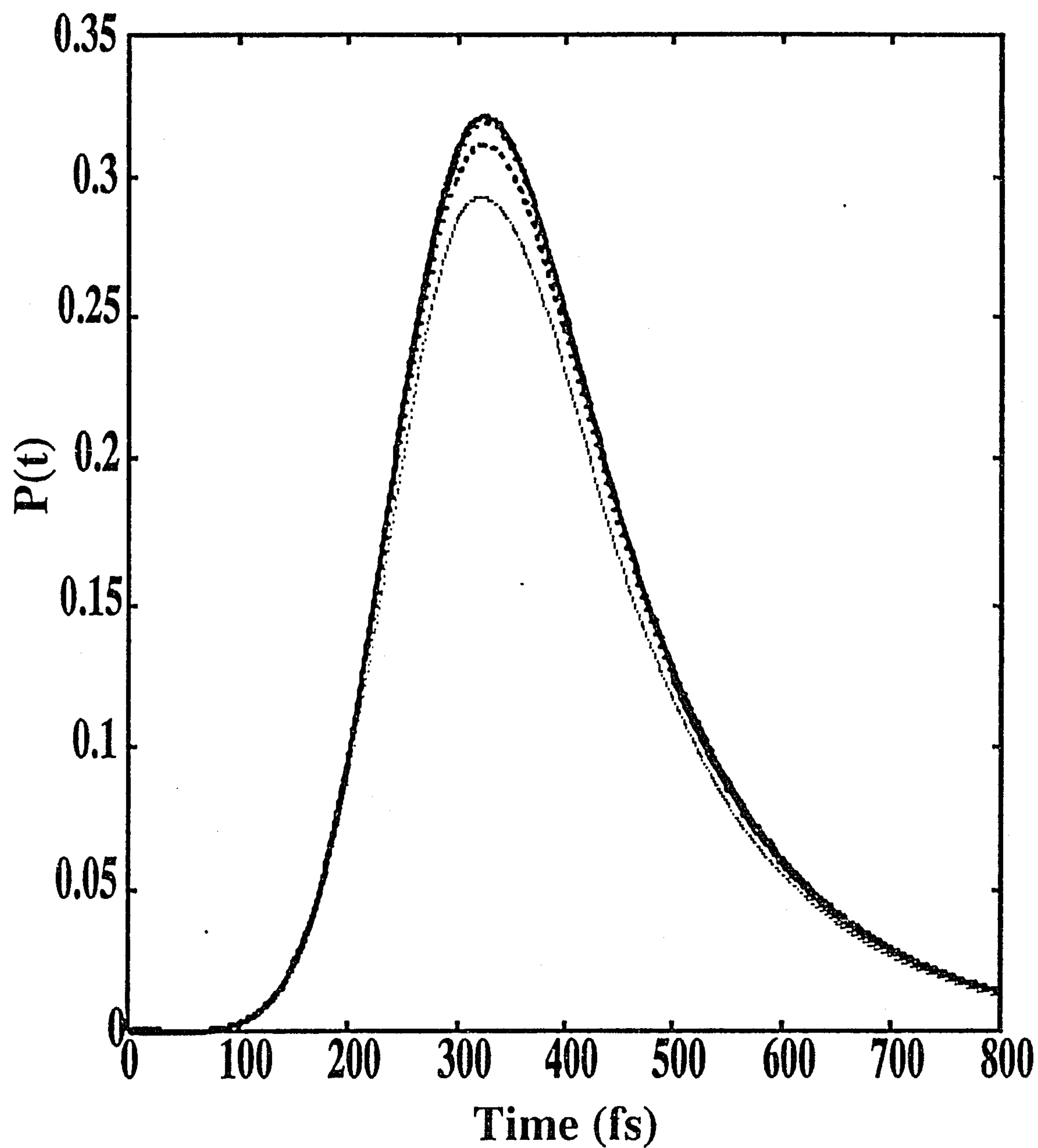

Fig. 5.2 The temporal development of the charges inside the quantum well of a double barrier structure. The solid curve is for no electron-phonon ijnteraction. The dashed, dot-dashed and dotted curves when electron interacts with interface antisymmetric, interface symmetric and confined phonon, respectively.

Reproduced with permission of the copyright owner. Further reproduction prohibited without permission.

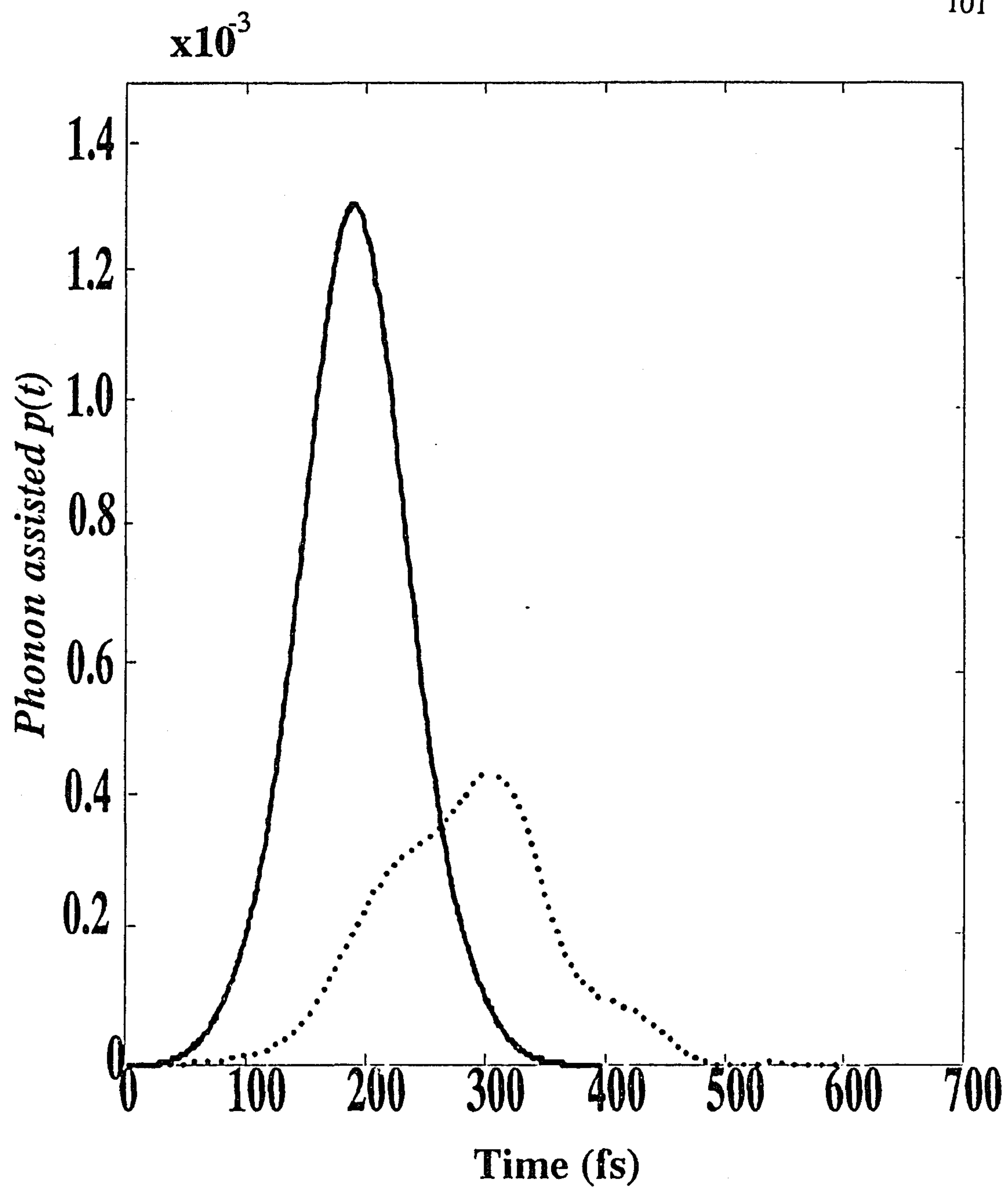

Fig. 5.3 The phonon assisted charge build-up due to confined phonon modes at room temperature. The solid (dashed) curve is when the electron wave packet is incident at one phonon energy above the resoant energy (one phonon energy below the resonant energy.

Reproduced with permission of the copyright owner. Further reproduction prohibited without permission.

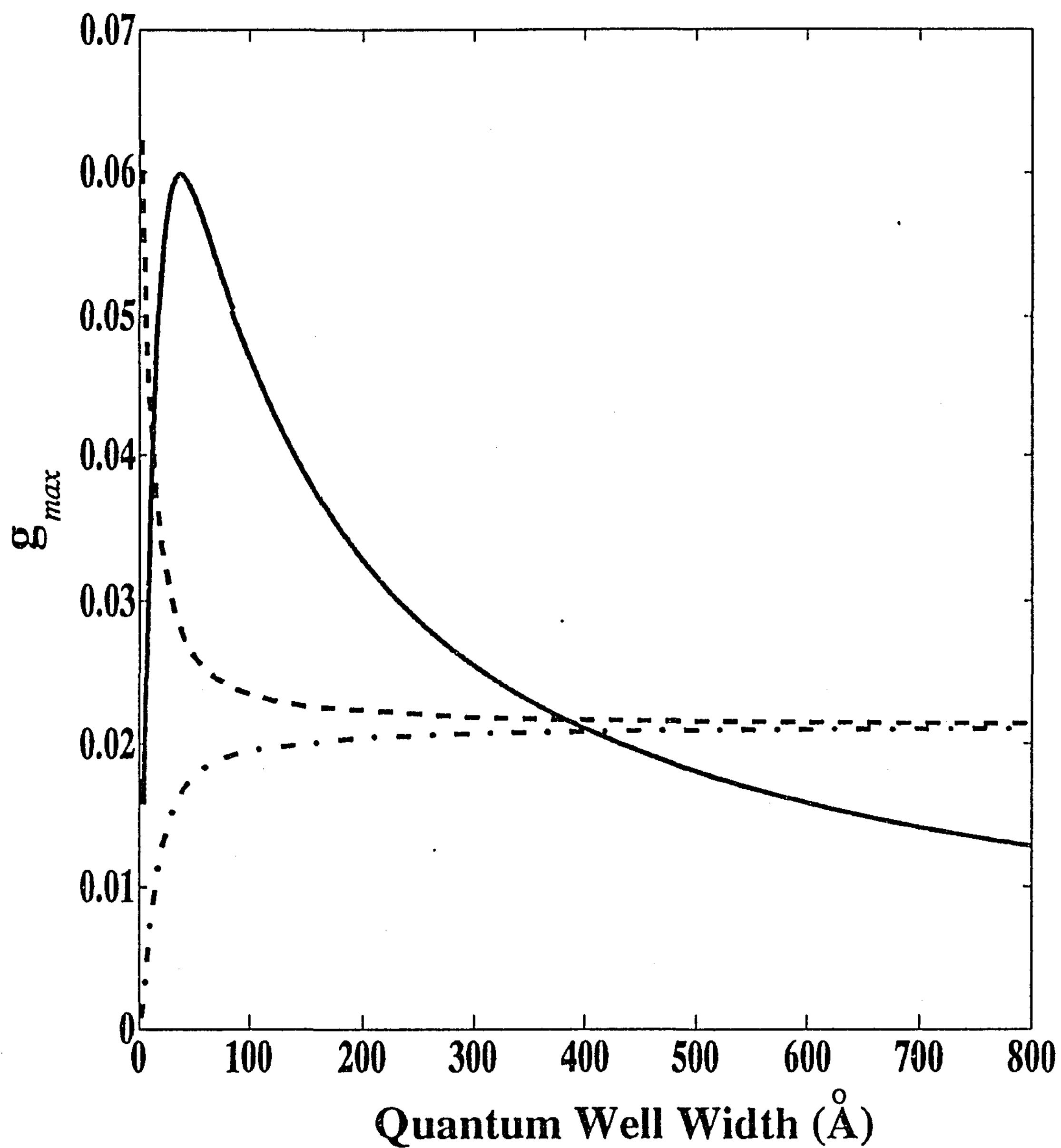

Fig. 5.4 The maximum value of the electron phonon coupling function g(z) as a function of the quantum well width. The solid, dashed and dot-dashed curves are for confined, interface symmetric and interface antisymmetric phonon modes, respectively.

Reproduced with permission of the copyright owner. Further reproduction prohibited without permission.

CHAPTER SIX

BARRIER POTENTIAL DESIGN CRITERIA IN MULTIPLE QUANTUM WELL BASED SOLAR CELL STRUCTURES

6.1 Introduction

The process of converting electromagnetic radiation is usually known as the photovoltaic effect. Like most of the principles on which energy conversion devices are based, the photovoltaic effect is not a new discovery. Back in 1839 a voltage was noted to develop when light was directed onto one of the electrodes in an electrolyte solution. Researchers turned the problem of utilizing photovoltaic effect as a power source in 1954 where a conversion efficiency of 6% was achieved[1] by means of p-n semiconductor junctions. A 15% efficiency was achieved when p-n silicon junctions were used. To set the stage for considering the physical process of turning light into electricity in a p-n junction it well be helpful to consider several other optical phenomena in semiconductors. It is interesting to note that many semiconductors that exhibit unusual properties under electrical and thermal excitation also exhibit interesting properties when irradiated with electromagnetic waves of various frequencies. For example, Silicon, a material that has found wide application in transistors, appears to have the typical metallic luster when viewed with ordinary light. When viewed under

Reproduced with permission of the copyright owner. Further reproduction prohibited without permission.

longer wavelength infrared radiation, however, Silicon becomes transparent. If we view the specimen of Silicon with very long-wave infrared radiation and slowly reduce the wavelength of radiation, we note that the transparency of the specimen increases. Further reduction in wavelength bring us to a point where the specimen's opaqueness increases abruptly. The shorter wavelength radiation is of higher energy, and thus when the radiation has a wavelength of 1.108 microns, it corresponds to an energy of 1.12 eV, which is the forbidden band width of silicon. Therefore, photons of this energy or higher are capable of exciting electrons from near the top of the valance band into energy levels near the bottom of the conduction band.

Photoconductivity is generally defined as the increase in the electrical conductivity of a semiconductor element when a radiation of the proper frequency is directed onto a semiconductor. The property has been widely exploited in devices designed to detect radiation. photoconductivity occurs appreciably when ever radiation having an energy larger than the forbidden energy gap of the semiconductor.

The photoconversion device that has attained the highest efficiency is the p-n junction. Since the density of electrons is larger in the n-type region than in the p-type region, electrons in the n side of the junction diffuse down the concentration gradient to the p-type region where they recombine with holes. Positive holes will flow simultaneously toward the n-type region . In a very short time (in the order of a nanosecond) the charging process is completed, with the p-type region possessing an excess of negative charge and the n-type taking on an excess positive charge. A contact potential deference

Reproduced with permission of the copyright owner. Further reproduction prohibited without permission.

having an energy $\Delta\phi$ (called the built-in potential) develops across the junction of such a magnitude to oppose the further flow of electrons and holes due to the concentration gradient. The region adjacent to the junction is referred to as the deletion region. Fig. (6.1) shows a p-n junction when irradiated by sun light. Electrons hole pairs will be generated leading to a change in the built in potential and a current to flow.

Up to date the conversion efficiency was progressing in single band solar cell and reached[2,3] a value of 28% in cells made from GaAs structures. Factors or losses that prohibit photoconversion devices from achieving high efficiencies include extrinsic and intrinsic ones. The extrinsic losses include the reflection losses which have been reduced almost to zero, by means of transparent coatings with appropriate thickness and refractive index. Hence, these losses are no longer of major concern. The *intrinsic* losses are the hard to control. These losses are schematically shown in Fig. (6.2) and can be classified as follows:

1) The inability of a single band gap material to absorb photon energies ($\hbar\omega$) less than the band gap energy (E_g).
2) Solar photons with $\hbar\omega > E_g$ generate free carriers that immediately loose most of their excess energy through nonradiative thermalization processes.
3) Recombination losses that increase with increasing the biasing voltage across the structure.

The vertical stacking of solar cells connected electrically in series with band-gap that decreases as light penetrates into the stack was suggested

Reproduced with permission of the copyright owner. Further reproduction prohibited without permission.

to offer much higher efficiency[4]. However, the highest efficiency observed for two cell tandem arrangements[5] was found comparable to those of single band gap material cells due to problems in making contacts between the cells.

In an attempt to overcome these intrinsic looses associated with the single band gap material mentioned above, multiple quantum well (MQW) systems were proposed to replace the intrinsic-depletion region in a p-n junction and to provide a novel approach for potentially high efficiency solar cells.[6,7] One of the advantages associated with the MQW structures is to custom-design a wide effective band gap by the suitable choice of various quantum well widths to cover the major portion of the solar cells. By changing the well width in the multiple quantum well structures, absorption can be insured to take place at the different quantum well energy levels, thereby reducing thermalization looses. Resonant electron tunneling can play a crucial rule to achieve maximum carrier collection efficiency. Although various kinds of tunneling processes have been extensively studied, using the resonant tunneling to enhance the solar cell efficiency has not been addressed.

Fig. (6.3a) shows a schematic representation of the intrinsic MQW region of the $p^+ - i - n^+$ solar cell structure. The quantum wells are designed under flat band conditions in Fig. (6.3b) such that the effective absorption band-gap will cover the whole energy spectrum of interest. To insure maximum energy level coupling throughout the structure under the application of electric field, the quantum well widths are designed such that the bound states lie at an energy equal to the voltage drop between any two adjacent wells. The barrier widths are

Reproduced with permission of the copyright owner. Further reproduction prohibited without permission.

optimized to enhance the resonant tunneling between adjacent wells. In Fig. (6.3c) the basic structure is shown under the resonant condition to maximize carrier collection through electron tunneling. Carriers absorbed in the MQW region will tunnel through the leftmost structure and then collected at the n^+ collector side at z_o.

In this chapter, the design criteria for achieving a maximum output power in GaAs/$Al_xGa_{1-x}As$ and InAs/$Ga_yIn_{1-y}As$ multiple quantum well based solar cell structures will be discussed. Suitable MQW structures to cover the major solar spectrum well be presented and the role played by electron resonant tunneling will be investigated.

6.2 Theory

In this section, the power, current, and maximum efficiency of a p-n junction will be outlined. The results will be extended to include the MQW structure in a p-i-n structure.

Built-in potential barrier due to the doping in the p-n junction can be altered by applying a voltage to this junction. If the p side is made more negative (*reversed biased*) with respect to the n side, then the energy barrier will increase and is seen now as $\Delta\phi + eV$ (V is the applied voltage) and it is virtually impossible for any electrons from the n type to surmount this barrier and enter the p-type. If we *forward bias* the p-n junction by making the p side more positive with respect to the n type, the potential barrier will be reduced and electrons will find it easier to escape to the p side. These situations are illustrated in Fig. (6.4).

Reproduced with permission of the copyright owner. Further reproduction prohibited without permission.

The equivalent circuit of a photovoltaic cell is also shown in Fig.(6.4).In the analysis to follow the intrinsic series resistance R_s and the intrinsic shunt resistance R_{sh} will be neglected. The simplified circuit without R_s and R_{sh} will yield essentially the same results as the more realistic model. Application of Kirchhoff's law to this simplified circuit will result in several interesting relationships. When a p-n junction is illuminated, the light causes a current I_l to flow in the load R_o; the relationship between this current, the current that would flow when the p-n junction were short circuited I_{ph} (photon current), the current that flows across the junction I_j, and the thermal current I_{th} is given by:

$$I_l = I_{ph} + I_{th} - I_j. \tag{6.1}$$

The photon current I_{ph} is usually refereed to as the short circuit current I_{sc} or $I_{sc} \equiv I_{ph}$. Eq. (6.2) can then be written in the following format:

$$I_l = I_{sc} + I_{th} - I_j. \tag{6.2}$$

Since it is more common to analyze the solar cells using current densities, rather than in terms of currents, I will now switch to the current density notations and will drop the subscript on the load current. The current densities are based on the area of exposed junctions. Eq. (6.2) can be written as follows:

$$J = J_{sc} + J_{th} - J_j \tag{6.3}$$

The junction current density is calculated as follows:

Reproduced with permission of the copyright owner. Further reproduction prohibited without permission.

$$J_j = e \int_{E_b/\hbar}^{\infty} d\omega \int d\Omega \cos(\theta) \rho \vartheta_g \tag{6.4}$$

where ρ is the radiation density incident on the surface of the semiconductor of the solar cell, ϑ_g is the group velocity and E_b is the barrier material band-gap. ρ is given by:

$$\rho = \frac{1}{4\pi^2} \frac{n^2 \omega^2}{c^2} \exp\left(\frac{eV - \hbar\omega}{kT} \right) \tag{6.5}$$

where n is the refractive index. The radiation incident on the solar cell surface with angles greater than $\sin(\theta) = 1/n$ is totally reflected, consequently:

$$\int d\Omega \cos(\theta) = \pi\left(1 + 1/n^2\right) \tag{6.6}$$

and the dark current becomes:

$$\begin{aligned} J_j &= \frac{e\left(n^2+1\right)}{4\pi^2 c^2} \int_{E_b/\hbar}^{\infty} \omega^2 \exp\left(\frac{eV - \hbar\omega}{kT} \right) d\omega \\ &= \frac{e\left(n^2+1\right) E_b^2 kT}{4\pi^2 c^2 \hbar^3} \exp\left(\frac{eV - E_b}{kT} \right) \left(1 + \frac{2kT}{E_b} + \frac{2k^2T^2}{E_b^2} \right) \\ &\approx \frac{e\left(n^2+1\right) E_b^2 kT}{4\pi^2 c^2 \hbar^3} \exp\left(\frac{eV - E_b}{kT} \right) = A\exp\left(\frac{eV - E_b}{kT} \right) \end{aligned} \tag{6.7}$$

The thermal current is simply $J_{th} = J_j(V=0)$ and hence:

$$J_{th} = \frac{e\left(n^2+1\right) E_b^2 kT}{4\pi^2 c^2 \hbar^3} \exp\left(\frac{-E_b}{kT} \right) = A\exp\left(\frac{-E_b}{kT} \right) \tag{6.8}$$

Reproduced with permission of the copyright owner. Further reproduction prohibited without permission.

this current is negligible for $E_b \geq 0.3$ eV compared to J_{sc}. In our work the minimum value for the barrier material band-gap is about 0.7 eV. Therefore, the thermal current will be neglected in our calculations. Hence:

$$J = J_{sc} - J_j \tag{6.9}$$

Now we turn our attention to the calculation of the solar cell efficiency. The maximum voltage that could be measured on the cell would occur under *open circuit* conditions, that is to say $J = 0$ or equivalently $R_o \to \infty$. From Eqs. (6.7) and (6.9) we have:

$$eV_{oc} = E_b - kT\ln\left(A/J_{scp}\right) \tag{6.10}$$

To find the voltage that will produce the maximum power density we compute the output power of the solar cell:

$$P = JV = \left(J_{sc} - A\exp\left(\frac{eV - E_b}{kT}\right)\right)V \tag{6.11}$$

Taking the derivative of this equation with respect to V and setting the result equal to zero yields an implicit equation for the voltage that maximizes the power:

$$\frac{eV_{mp}}{kT} = \ln\left(\frac{J_{sc}}{A}\right) + \frac{E_b}{kT} - \ln\left(\frac{eV_{mp}}{kT} + 1\right). \tag{6.12}$$

or

$$eV_{mp} = eV_{oc} - kT\ln\left(1 + eV_{mp}/kT\right) \tag{6.13}$$

Reproduced with permission of the copyright owner. Further reproduction prohibited without permission.

The current density that maximizes the power may be found by combining the expression for the maximum power voltage V_{mp} as given via Eq. (6.13) with the expression given for the current density given in Eq. (6.9):

$$J_{mp} = J_{sc} - \frac{J_{sc}}{1 + eV_{mp}/kT} \tag{6.14}$$

or

$$J_{mp} \approx \frac{J_{sc}}{1 + kT/(eV_{mp})} \tag{6.15}$$

The maximum power density is then given by:

$$P_{max} \approx \frac{V_{mp} J_{sc}}{1 + kT/eV_{mp}} \tag{6.16}$$

The power density input to the junction is simply the total number of photons in the solar spectrum, N_{ph}, times the average energy of each of those photons, ϕ_{ave}. The maximum efficiency can be approximated as follows:

$$\eta_{max} = \frac{P_{max}}{P_{in}} \approx \frac{V_{mp} J_{sc}}{\left[1 + kT/eV_{mp}\right] N_{ph} \phi_{ave}}. \tag{6.17}$$

The short circuit current density J_{sc} in single band-gap solar cell structure used to be assumed by the number of absorbed carriers. In MQW solar cell structures this short circuit density will be dependent on the carrier tunneling probability which drastically affect the prediction of the calculated power or efficiency.

Eq. (6.15) is rewritten as follows:

Reproduced with permission of the copyright owner. Further reproduction prohibited without permission.

$$J_{mp} = \frac{J_{scp}}{1 + kT/eV_{mp}} \tag{6.18}$$

where J_{scp} is the peak value of the time-dependent tunneling short circuit current density. I will show the calculation of J_{scp} later in the chapter.

Using Eqs. (6.10) and (6.13)along with the relation between the barrier potential V_o, the quantum well band-gap E_w, and the barrier material band gab E_b:

$$V_o = Q_c(E_b - E_w) \tag{6.19}$$

where Q_c is the conduction band offset parameter, a numerical solution to the implicit relationship between V_{mp} and V_o can be obtained.

The calculated value of V_{mp} using Q_c=0.7, E_w =1.42 eV for GaAs/Al_xGa_{1-x}As or E_w =0.36 eV for InAs/Ga_yIn_{1-y}As structures at T=300K was found to have a linear relationship with the barrier potential given by:

(1) for InAs/Ga_yIn_{1-y}As structures,

$$eV_{mp} = 1.28V_o + 0.004 \text{ with } E_w = 0.36 \text{ eV}; \tag{6.20}$$

(2) for GaAs/Al_xGa_{1-x}As structures,

$$eV_{mp} = 1.28V_o + 0.930 \text{ with } E_w = 1.42 \text{ eV}, \tag{6.21}$$

where the voltage at maximum power will be in volts when the barrier potential in electron-volts.

The expression for the energy efficiency for InAs/Ga_yIn_{1-y}As and GaAs/Al_xGa_{1-x}As structures are, respectively:

Reproduced with permission of the copyright owner. Further reproduction prohibited without permission.

$$\eta = \frac{J_{mp}V_{mp}}{P_{in}} = \frac{J_{mp}(1.28V_o + 0.004)}{N_{ph}\phi_{ave}} \tag{6.22}$$

and

$$\eta = \frac{J_{mp}V_{mp}}{P_{in}} = \frac{J_{mp}(1.42V_o + 0.93)}{N_{ph}\phi_{ave}} \tag{6.23}$$

Now I go back to the calculation of the short circuit current density tunneling through the MQW structure.

An initial electron wave packet of the form:

$$\psi(z,t=0) = \sqrt{\frac{2}{l_z}}\sin\left(\frac{\pi z}{l_z}\right) \tag{6.24}$$

was placed in the left most well. l_z is the width of the left most quantum well where the carrier absorption takes place. The calculation of the short circuit current density $J_{sc}(z_o,t)$ at the end of the structure at point z_o follows exactly the procedure detailed in chapters two and three.

6.3 Results and Discussion

Fig. (6.5) shows the temporal profiles of $J_{sc}(z_o,t)$ for different barrier potentials when the structure is biased at resonance (see Fig. (6.3c)). In this figure it was assumed that 10^{16} electrons/s.cm^2 reaching the ground state energy level in the absorption band at equilibrium condition Each time the barrier potential was changed, the widths of the various quantum wells were changed. The electric field was applied for each barrier potential structure and was tuned in each case until maximum collection was achieved.

Reproduced with permission of the copyright owner. Further reproduction prohibited without permission.

Two salient features can be observed from the curves of Fig. (6.5): First, the time required for $J_{sc}(z_o,t)$ to reach the peak value J_{scp} at the collector side of the solar cell increases as the barrier potential increases. This change is due to the fact that the tunneling time is inversely proportional[7] to the width of the energy level which the electrons are tunneling through. The larger the barrier potential, the narrower the energy levels. Hence, the more time needed for the carriers to reach the collector side. Second, the peak value of the short circuit current density J_{scp} decreases as the barrier potential increases. This change is attributed to the carrier tunneling probability being smaller for larger barriers.

In addition to the current density, the other parameter in determining the solar cell efficiency is the output voltage. Based on the solution of the intrinsic relation for the solar cell output voltage at maximum (V_{mp}), it is found that the relation between the V_{mp} and the barrier potential (V_o) is always linear, $V_{mp} = \alpha V_o + \beta$. The slope α is found to be the same in spite of the MQW materials. However, the constant β is found to be negligible compared to αV_0 for structures with small band gap material for quantum well such as $InAs/Ga_yIn_{1-y}As$ structures and is the dominant factor for structures with large band gap material for quantum well such as $GaAs/Al_xGa_{1-x}As$ structures. The value of β increases as the band gap material for the quantum well increases. As a result, it is found that a maximum efficiency can be achieved at a specific barrier potential or barrier material band gap for structures with small quantum well band-gap where β is negligible. In the $InAs/Ga_yIn_{1-y}As$ MQW structure case, this barrier potential is about

Reproduced with permission of the copyright owner. Further reproduction prohibited without permission.

450 meV. For MQW structure with large quantum well band gap such as GaAs/Al_xGa_{1-x}As, where β is the dominating factor in determining V_{mp}, the efficiency is found to decrease linearly as the barrier potential increases.

Fig. (6.6) shows the calculated solar cell current density J_{mp} at the maximum power along with the solar cell output voltage V_{mp} at the maximum power for both of the MQW systems under consideration. This figure shows clearly the exponential decline of J_{mp} as a function of the barrier potential. This is due to the current density dependence on carrier tunneling probability which decline exponentially with barrier potential. The cell output voltage V_{mp} increases linearly with the barrier potential.

Fig. (6.7) shows the calculated efficiency curves using Eqs.(6.21) and (6.22) for the two MQW systems mentioned above. From the InAs/Ga_yIn_{1-y}As MQW structure efficiency curve, it is clear that the efficiency *peaks* when the structure is designed with the value of y ≈ 0.6 such that the barrier potential is about 450 meV. This effect can be attributed to the fact that V_{mp} being directly proportional and directly determined by V_o and its minimum and maximum magnitude are not far from those of the barrier potential with J_{mp} being exponentially decaying with V_o as shown in Fig.(6.4). Their product gives a peak at a specific barrier potential. The efficiency of InAs/Ga_yIn_{1-y}As based cells reaches 72%. Absorption in the different bands will result in approximately the same efficiency if carrier absorption is kept constant. The efficiency in GaAs/Al_xGa_{1-x}As based cells decreases linearly when the barrier potential increases since the minimum value of eV_{mp} is

Reproduced with permission of the copyright owner. Further reproduction prohibited without permission.

larger than the largest barrier potential and not primarily determined by V_o for the barrier potentials under consideration. Increasing the barrier potential beyond the 700 meV potential will not improve the results, because the current density will reach negligible values. Barrier potentials lower than 200 meV were not considered since MQW wells with small barriers will not be suitable to cover large portion of the sun spectrum. An efficiency of about 80% results because of the large tunneling current density due to large carrier tunneling probability and large voltage at maximum power at the 200 meV barrier potential.

In order to properly design a complete structure, I display in Fig. (6.8) the solar spectrum intensity versus the wave numbers (energy). It is clear that the MQW solar cell structure should be designed to cover energies between 0.5 to 3.2 eV. the sun radiation spectrum

Based on our simulated results, a suggested MQW solar cell structure should embody $InAs/Ga_{0.6}In_{0.4}As$ structure where the efficiency peaks followed by $Ga_{0.6}In_{0.4}As/GaAs$ with the barrier potential of 300 meV. This structure is followed by $Al_aGa_{1-a}As/Al_bGa_{1-b}As$ where a, b are to be chosen such that each MQW structure results in a barrier potential of about 300 meV. Note that even the efficiency is higher for barrier potentials less than 300 meV, use of 200 meV or lower barrier potentials might not be practical since the resulting quantum wells will not be able to cover a large solar spectrum. Fig. (6.9) shows a schematic diagram fro the solar cell MQW structure that should be able to cover the major sun light.

It is of particular importance to note that for the MQW well solar cell to operate, the resonance condition has to be always

Reproduced with permission of the copyright owner. Further reproduction prohibited without permission.

maintained. Hence, in the design process of the MQW structure, the number of quantum wells must be designed such that the difference between the operating potential (eV_{mp}) and the built-in potential must bias the structure at the resonance condition. Maintaining the resonance is crucial. Weather fluctuations for example might disturb the carrier absorption and hence, change the operating potential resulting in breaking down the resonance condition. Due to such problems, MQW solar cells might be very useful in outer space where weather fluctuations disappears and photon flux is nearly constant at the operating potential. It is also important to mention that even our model considered only five quantum wells in the MQW structure, the calculated values for the short circuit current density under the resonant condition *will not be different,* only the time of arrival at the point z_o will increase if the number of quantum wells were increased.

Reproduced with permission of the copyright owner. Further reproduction prohibited without permission.

6.4 References

1) Stanley W. Angrist, *Direct energy conversion*, 4th edition, Allyn and Bacon Inc. 1982 (chapter 5).

2) N. R. Kaminar, D. D. Liu, H. F. MacMillan, L. D. Partain, M. Ladle Ristow, G. F. Virshup, and J. M. Gee, in *Proceedings of the 20th IEEE Photovoltaic Specialists Conference* (IEEE, New York, 1988), p. 766.

3) C. H. Henry, J. App. Phys. **51**, 4494 (1980).

4) H. Pauwels and A. de Vos, in *Proceedings of the 15th IEEE Photovoltaic Specialists Conference* (IEEE, New York, 1981), P. 377.

5) J. M. Olson, S. R. Kurts, and A. E. Kibbier, in *Proceedings of the 15th IEEE Photovoltaic Specialists Conference* (IEEE, New York, 1988), P. 777.

6) C. J. Summers and K. F. Brenan, Appl. Phys. Lett. **48**, 806, (1986).

7) K. W. J. Barnham and G. Duggan J. Appl. Phys. **67**, 3490, (1990).

Reproduced with permission of the copyright owner. Further reproduction prohibited without permission.

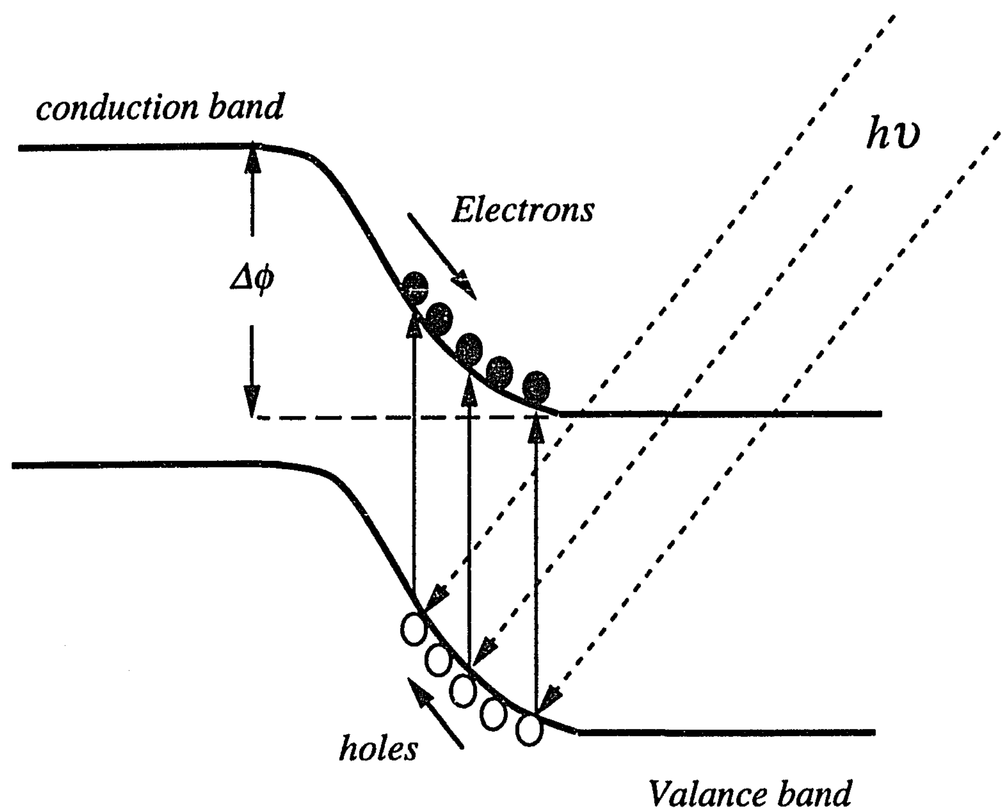

Fig. 6.1 A schematic diagram of a p-n junction showing the energy band scheme as a function of position in the junction. Photons irradiate the material results in extra carriers in the conductions band and aflow of current.

Reproduced with permission of the copyright owner. Further reproduction prohibited without permission.

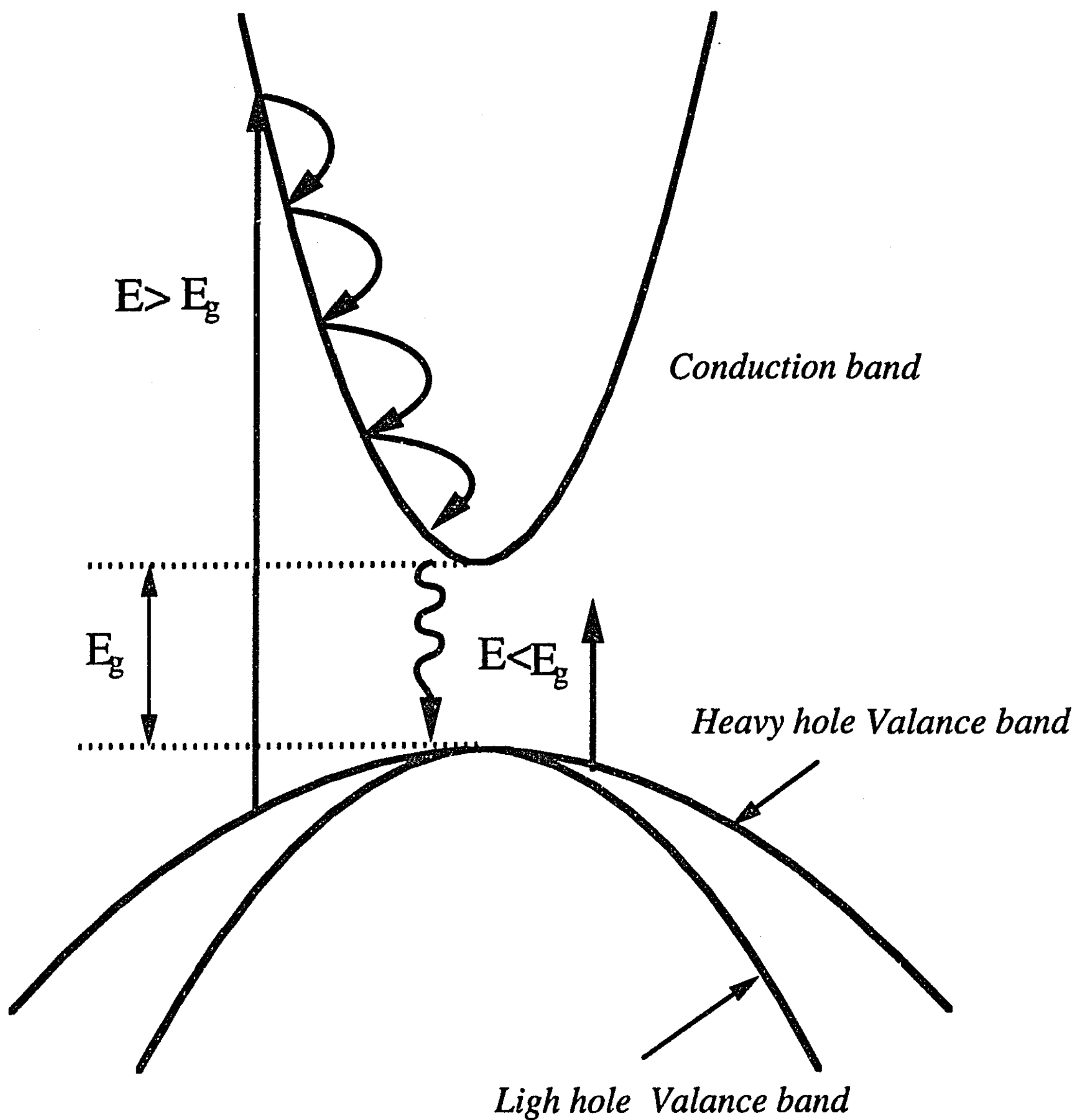

Fig. 6.2 A schematic representation of intrinsic losses associated with single band gap solar cell sttructures. These losses are solvable by using a multiple-quantum well solar cell structure.

Reproduced with permission of the copyright owner. Further reproduction prohibited without permission.

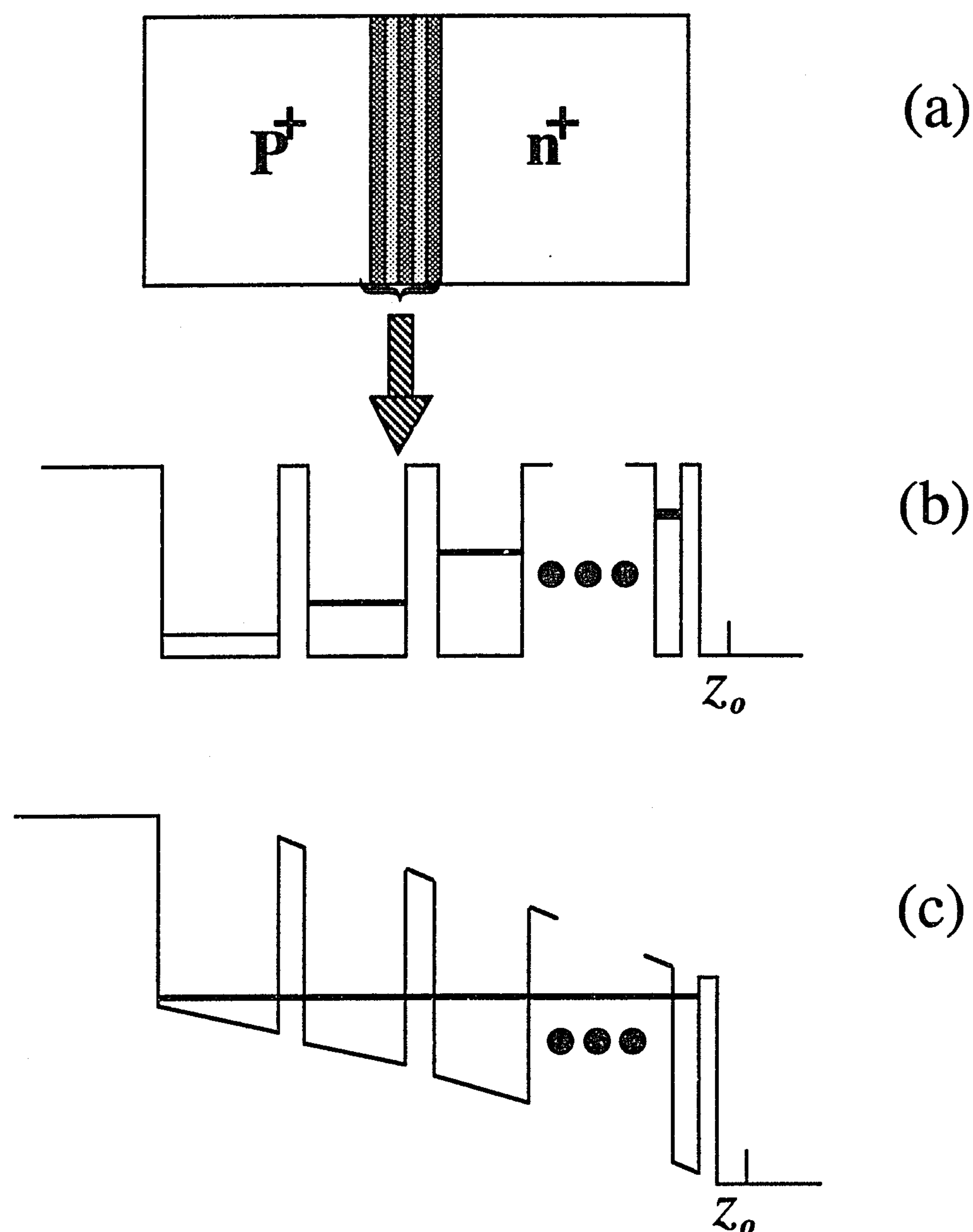

Fig. (6.3) A schematic diagram of the intrinsic MQW region of a solar cell structure, quantum well change in width to cover different absorption bands. Barrier widths are fixed at 20-Å, (a) schematic *p-i-n*, (b) under flat band conditions, (c) under resonant conditions.

Reproduced with permission of the copyright owner. Further reproduction prohibited without permission.

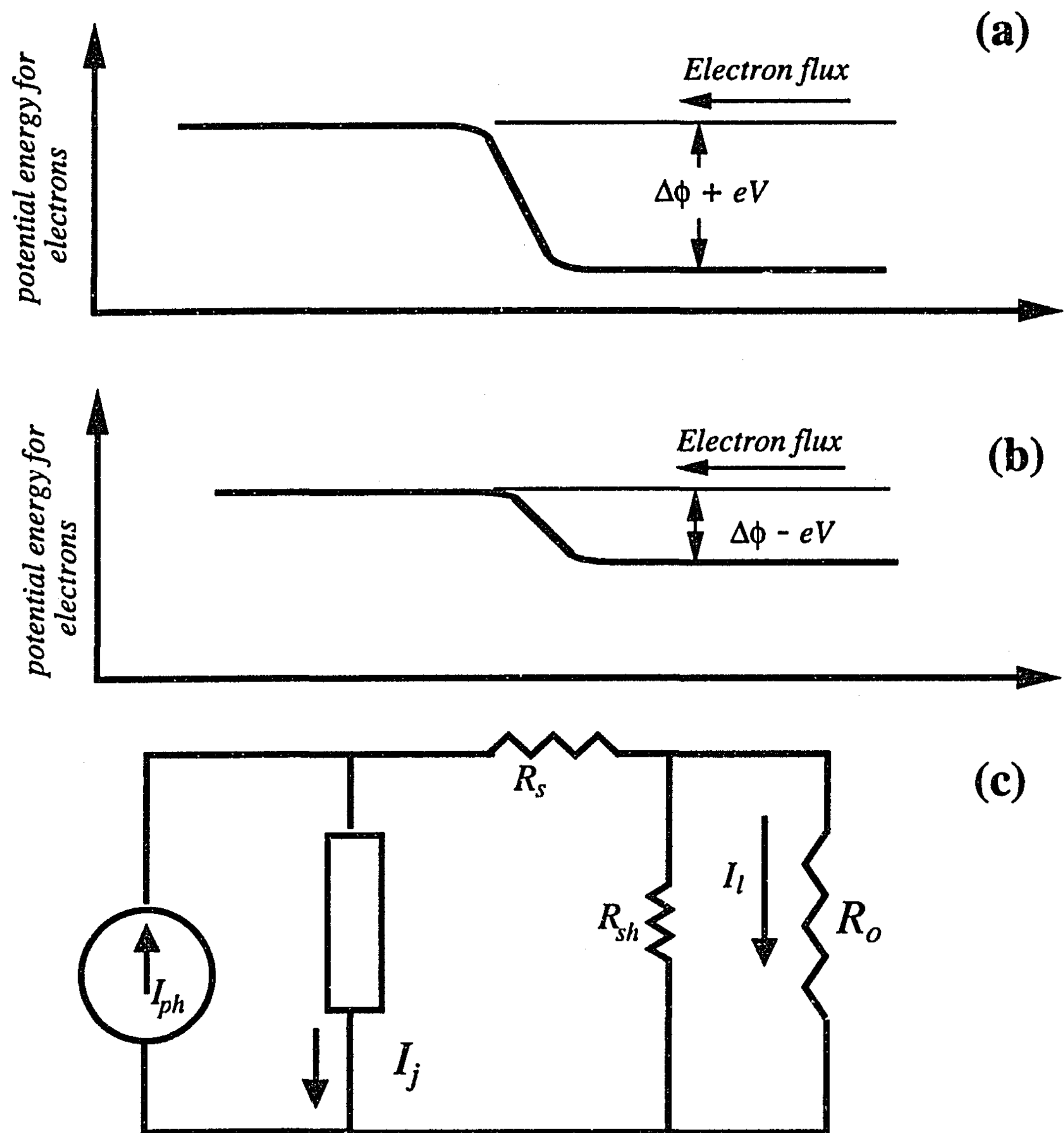

Fig. (6.4) a) the reverse biasing conditions. Barrier potential increases and the current will decrease. (b) The forward biasing conditions. The potential barrier will becrease resulting in a current increase. (c) The simlified equivalent circuit of an illuminated p-n junction photovoltaic solar cell that used in the chapter.

Reproduced with permission of the copyright owner. Further reproduction prohibited without permission.

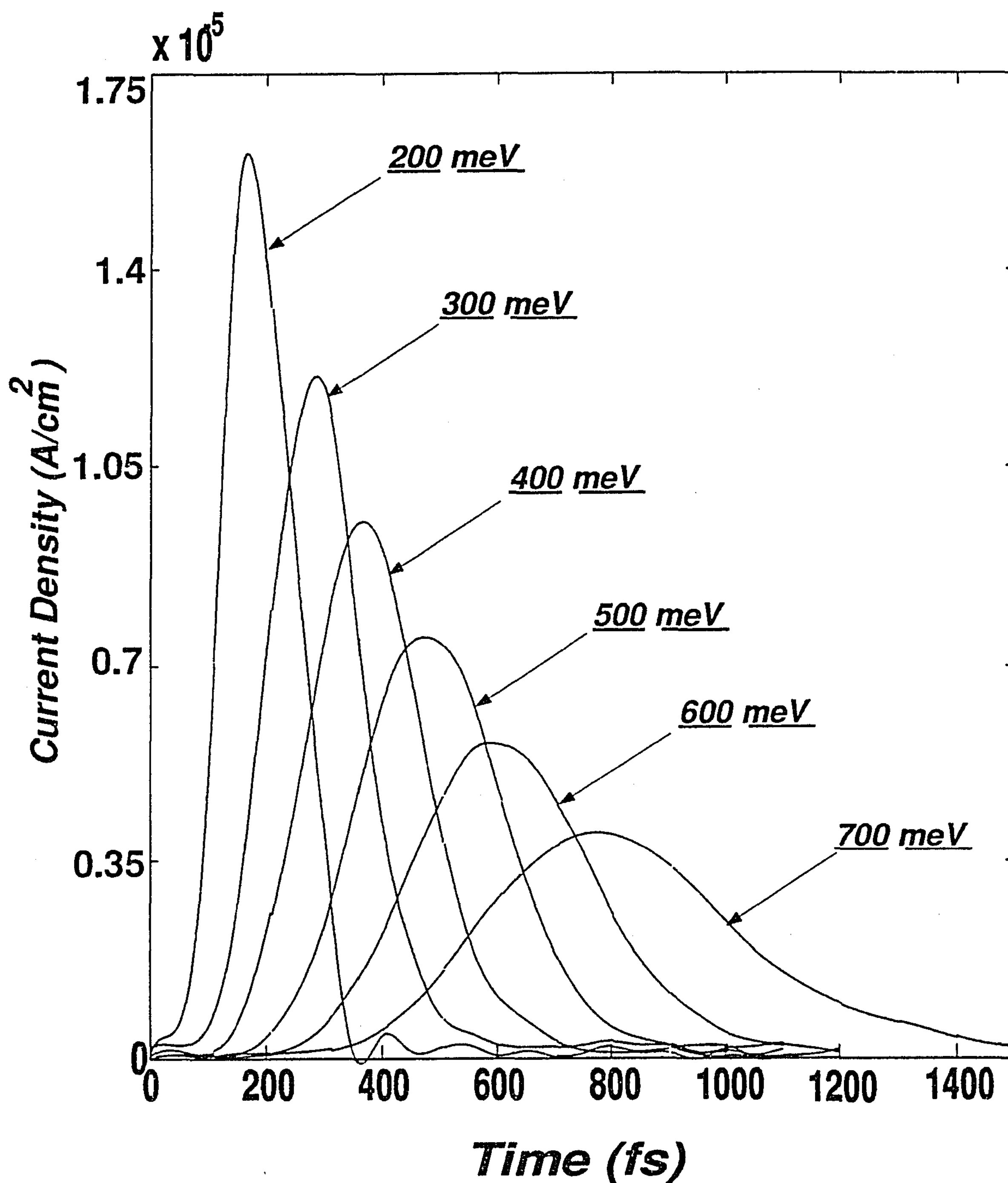

Fig. (6.5) The temporal profiles of the short circuit current density reaching the collector side of the solar cell. Each curve is marked by the barrier potential of the MQW structure used.

Reproduced with permission of the copyright owner. Further reproduction prohibited without permission.

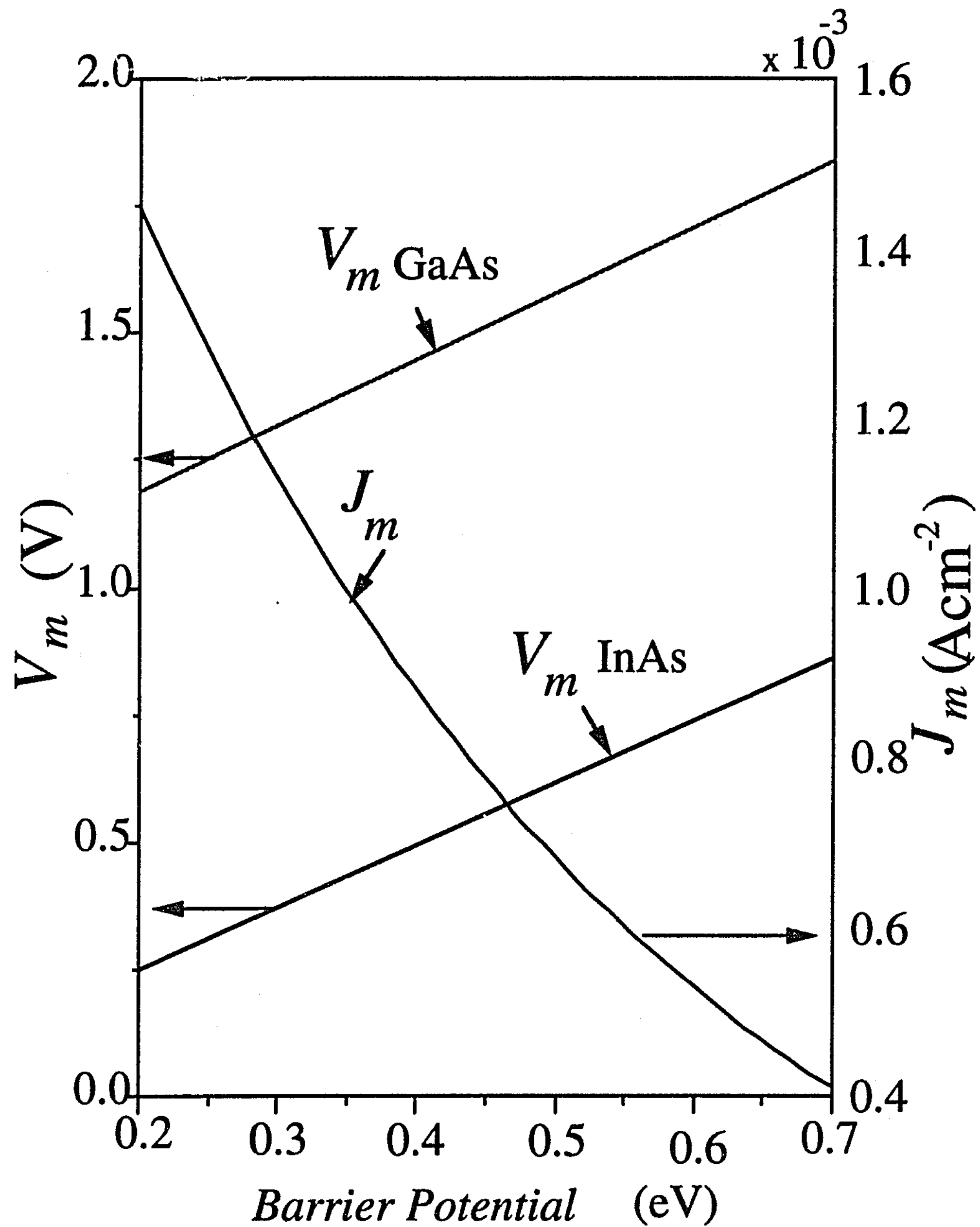

Fig. (6.6) The MQW solar cell current density at maximum power along with output voltage at maximum power for InAs/GaInAs and GaAs/AlGaAs based MQW structures.

Reproduced with permission of the copyright owner. Further reproduction prohibited without permission.

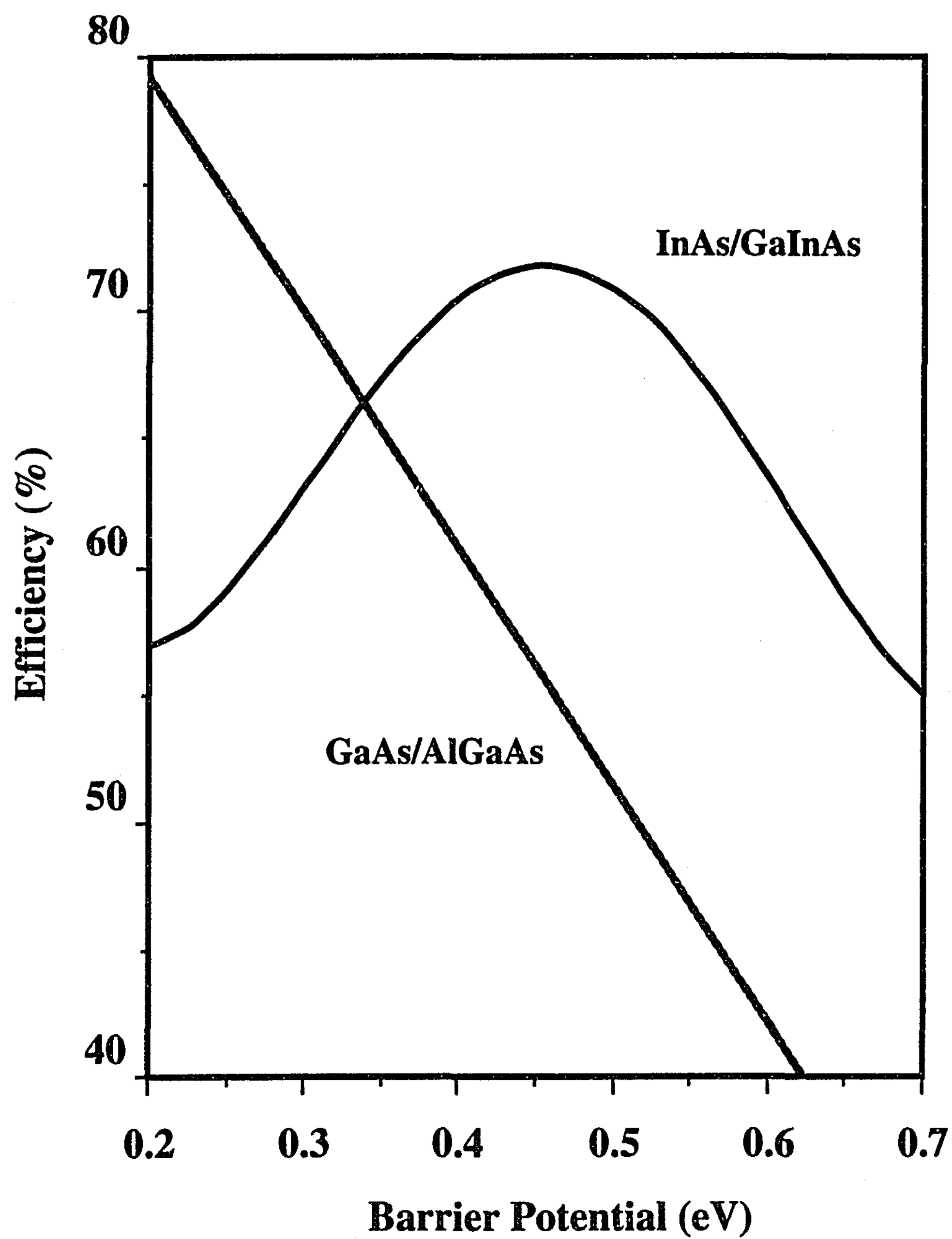

Fig. (6.7) The energy efficiency of InAs/GaInAs and GaAs/AlGaAs MQW based solar cells.

Reproduced with permission of the copyright owner. Further reproduction prohibited without permission.

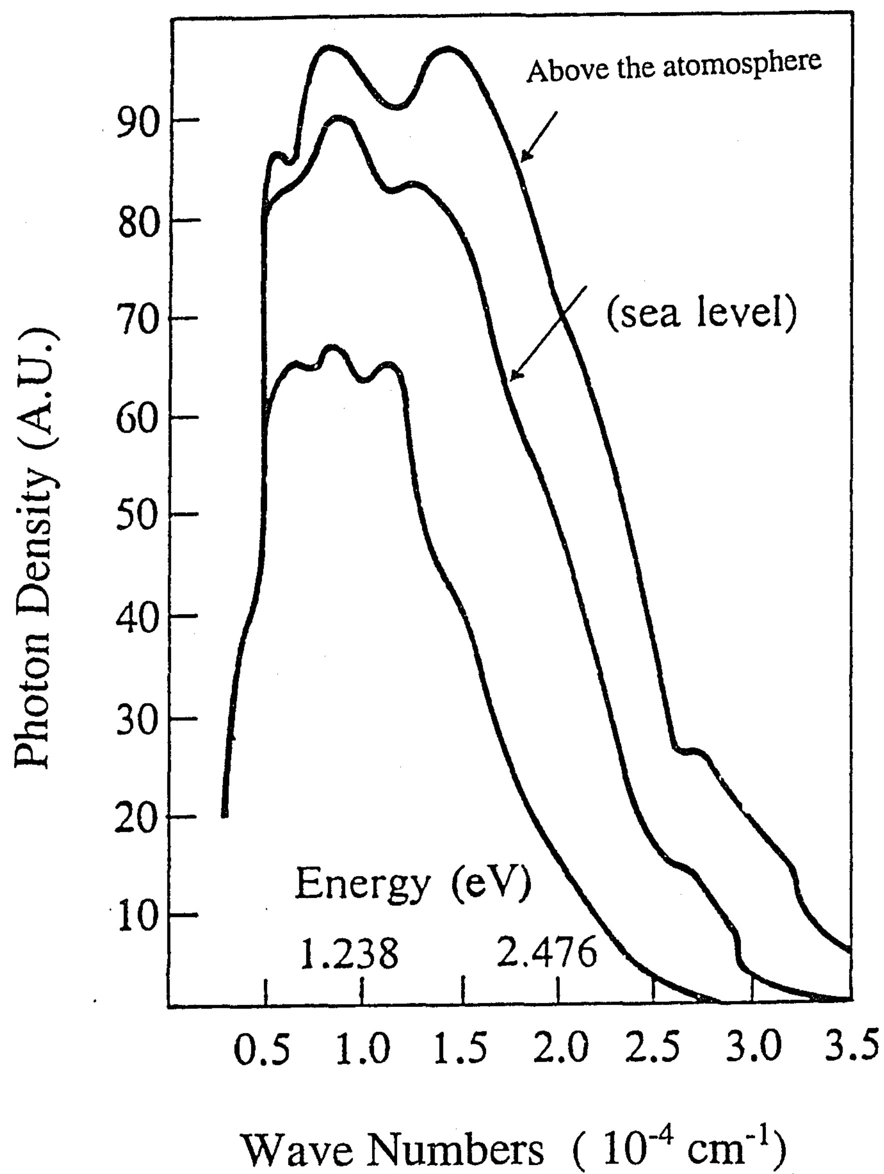

Fig. 6.8 The photon density of the solar spectrum as a function of energy for different positions.

Reproduced with permission of the copyright owner. Further reproduction prohibited without permission.

Reproduced with permission of the copyright owner. Further reproduction prohibited without permission.

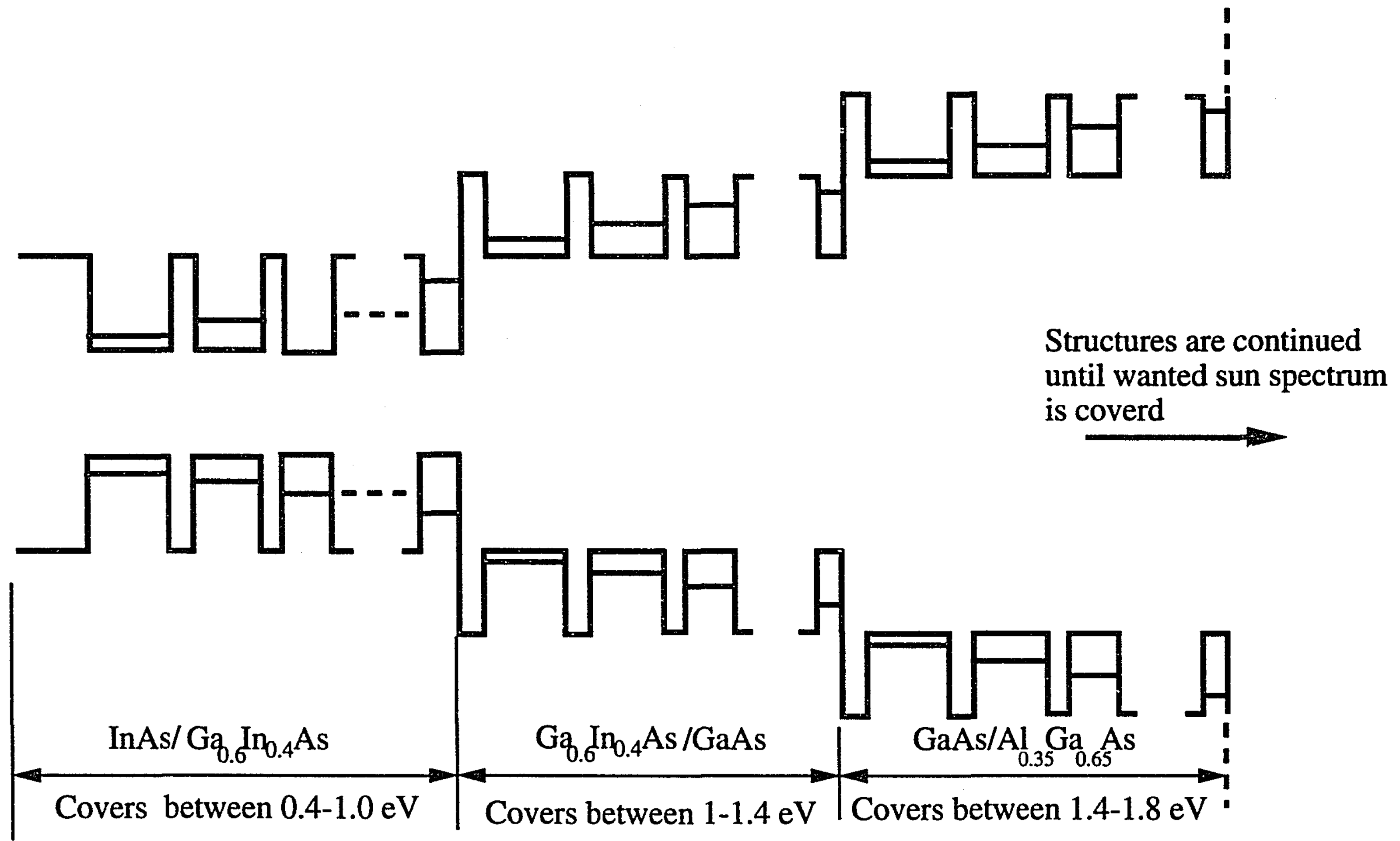

Fig. 6.9 A schematic representation of the MQW solar sell. The scheme for covering the major portion of the solar spectrum is shown. Under resonant condition energy levels will couple together and carrier collection will be achieved via resonant tunneling.

CHAPTER SEVEN

SUMMARY

7.1 Summery

The dynamics of electron tunneling in engineered semiconductor nanostructures were explored by means of the numerical solution of the time-dependent Schrödinger equation. Effect due to electron-hole and electron-phonon interactions were included as well as the use of electron resonant tunneling to design efficient multiple quantum well based solar cell structures.

In studying the dynamics of electron tunneling through a double barrier structure as a function of electron wave packet central incident energy, it was shown that (i) the charge build-up process in the quantum well of the double barrier structure will not reflect the presence of resonance states in the early time period of 0-40 fs, (ii) resonance peaks start developing as time passes the 40 fs and appear initially blue-shifted from the energy positions of the resonant states predicted using the time-independent calculations. As time increases the resonant peaks shift toward the predicted positions, and (iii) the bandwidth (FWHM) of the resonant states starts to be large and decreases as time increases.

The tunneling process is extended to investigate the effect of electron-hole interaction on the interesting phenomena of electron wave packet oscillation in double quantum wells under resonant conditions. It was demonstrated both in time and energy domains that the electron-

Reproduced with permission of the copyright owner. Further reproduction prohibited without permission.

hole interaction or equivalently the excitonic interactions affect the period of the electron wave packet oscillation in the double quantum wells by as much as 15%.

In addition to the excitonic effects, a method was presented for studying the dynamics of electron tunneling in the presence of electron-plane wave LO phonon and electron-localized LO phonon interactions. The temporal profiles of a tunneling electron wave packet at different lattice temperatures. It was shown that the tunneling current decreases in the presence of plane wave LO phonons. The calculated temperature dependence of the peak current density agrees qualitatively with available experimental data.

As an extension to the electron-plane wave phonon interaction, I investigated also the charge build-up in the quantum well of a double barrier structure in the presence of electron-localized LO phonon interactions. It was shown that the effect of antisymmetric interface phonons on the charge build-up is negligible and that symmetric and confined phonon modes reduce the probability of finding the electron inside the quantum well. Phonon assisted charge build-up was also investigated when the electron wave packet is incident at the $E_r \pm \hbar\omega$ energy channels. It was found that phonon-assisted charge build-up in the well is about 2 orders of magnitude smaller than that of resonantly injected charge. The strength of electron-phonon coupling due to confined phonons peaks at quantum well width of about 40-Å.

The use of electron resonant tunneling was applied for MQW based solar cell structures for the purpose of high energy conversion efficiency. Based on calculating the short circuit current density

Reproduced with permission of the copyright owner. Further reproduction prohibited without permission.

reaching the collector side of the solar cell and the relation between the cell output voltage and the MQW barrier potential, the role of electron resonant tunneling and the proper barrier potential was determined. It was shown that solar cell MQW structures made with small quantum well material band-gap such as that of InAs in InAs/GaInAs structures, the efficiency will peak at a specific barrier potential. The barrier potential for InAs/GaInAs was found to be around 450 meV. For structures with large quantum well material band gap as that of GaAs in GaAs/AlGaAs the efficiency declines linearly as the barrier potential is increased.

Reproduced with permission of the copyright owner. Further reproduction prohibited without permission.

CHAPTER EIGHT

FUTURE DIRECTIONS

8.1 Introduction

In chapters one through six, the basic understanding of tunneling dynamics in semiconductor heterolayres was investigated. Moreover, utilizing the tunneling dynamics for designing high efficiency solar cells was also studied. In the next two section I will outline the future direction of my research which focuses on more understanding of carrier tunneling dynamics and the possible use of carrier tunneling in designing high performance devices such as wide band photodetectors.

8.2 Electron tunneling in the presence of Γ−X mixing

One of the problems that is Associated with solar cell structures is the recombination losses. The problem was addressed earlier in chapter six. Solar cells with large structures (a few microns) can still suffer from recombination losses because increasing the length of the structure implies that the electron will take longer time while tunneling through the structure. This tunneling time might be comparable to the carrier recombination life time and, hence, recombination might take place.. A possible way to eliminate this problem is to increase the recombination life time with respect to the resonant tunneling time. One possible way of do this is to have the resonant tunneling takes place through the X states. Even though the tunneling time via X states is larger than that of

Reproduced with permission of the copyright owner. Further reproduction prohibited without permission.

Γ states due to heavy X electron mass, the recombination life times of the X electrons is orders of magnitude larger that of Γ electrons.

As a first step toward understanding the electron tunneling via X states as a possible candidate for solar cell technology is to study the charge oscillation between the X and Γ states under X and Γ level coupling.

At the presence of strong Γ-X level coupling, electrons will be initially photogenerated in the Γ valley of a superlattice structure. Γ electrons will tunnel to and populate the X valley and those will tunnel back and charge will start oscillating between the two states. The oscillation period is governed by how large is the energy separation between the X and Γ states, being largest for minimum separation.

8.3 4 to 8 μm wide band infrared photodetector

The structure for MQW based solar cell structure was designed and carrier absorption was in chapter 6 from the valance to the conduction band. A similar procedure can be used to design a multiple quantum well structure such that each quantum well will at least contain two bound states. The ground states will be doped in order that carrier absorption will take place between the ground state and the first excited energy level in each quantum well. Quantum well sizes will vary such that the energy difference between the ground state and the first excited state will span the range between 4-8 μm. Electric field will be applied to the structure to have the first excited state in each well matching every other first excited state in the other wells and resonant tunneling

Reproduced with permission of the copyright owner. Further reproduction prohibited without permission.

is used to collect absorbed carriers.

The advantage of such structure in to design a photodetector that covers completely the infrared region 4 to 8 mm which has not been achieved or done yet.

Reproduced with permission of the copyright owner. Further reproduction prohibited without permission.

APPENDIX

A.1 A FORTRAN-77 computer program to generate the figures of chapter two

This program solves the Schrödinger time dependent equation for an electron tunneling through the double barrier structure of chapter two. It uses a Gaussian wave packet as input or as an initial condition and calculates the charge inside the quantum well by integrating over the electronic wave function magnitude as the output.

```
*************************************************************
        dimension  alpha1(21000), alpha2(21000), u0(21000)
        dimension x(21000), r0(21000), a(21000), aa(21000)
        dimension bb(21000), c(21000), v(21000), gam(21000)
        dimension alpha(21000), d(21000), charge(21000)
        dimension cu0(21000)
        complex i, u0, cu0, r0, gam, bb, bet, b
        i=(0,1)
        v0=0.280
        do 1 j=0,5884
        v(j)=0.0
        alpha(j)=0.6097
1       continue
        do 2 j=5885,5944
        v(j)=v0
        alpha(j)=0.8372
2       continue
        do 3 j=5945,6064
        v(j)=0.0
        alpha(j)=0.6097
3       continue
        do 4 j=6065,6124
        v(j)=v0
        alpha(j)=0.8372
4       continue
        do 5 j=6125,20000
        v(j)=0.0
        alpha(j)=0.6097
5       continue
        do 71 j=1,20000
        x(j)=0.5*float(j-1)
71      continue
        do 77 j=1,20000
        alpha1(j)=alpha(j)+alpha(j+1)
```

Reproduced with permission of the copyright owner. Further reproduction prohibited without permission.

```
      alpha2(j)=alpha(j)+alpha(j-1)
      d(j)=alpha1(j)/alpha2(j)
77    continue
      open(7,file='charge.data')
      do 32 k=1,281
      e=float(j)
      ak=4.19e-03*sqrt(e)
      do 6 j=0,20000
      if(j.gt.5884)go to 7
      if(j.lt.100)go to 7
      u0(j)=exp(i*ak*x(j))*exp(-(x(j)-1450.)**2/6.05e+5)
      go to 6
7     u0(j)=(0.0,0.0)
6     continue
      do 12 j=1,20000
      a(j)=d(j)
      b(j)=4.74e-03*alpha1(j)*i-3.6e-03*v(j)*alpha1(j)-1.-a(j)
      c(j)=1.00
      bb(j)=4.74e-03*alpha1(j)*i+3.6e-03*v(j)*alpha1(j)+1.+a(j)
12    continue
      do 18 n=1,1000
      write(6,*)n
      do 13 j=1,20000
      r0(j)=-u0(j+1)+bb(j)*u0(j)-a(j)*u0(j-1)
13    continue
      bet=b(1)
      u0(1)=r0(1)/bet
      do 14 j=2,19999
      gam(j)=c(j-1)/bet
      bet=b(j)-a(j)*gam(j)
      u0(j)=(r0(j)-a(j)*u0(j-1))/bet
14    continue
      do 16 j=19998,1,-1
      u0(j)=u0(j)-gam(j+1)*u0(j+1)
16    continue
      do 21 j=1,20000
      cu0(j)=conjg(u0(j))
      charge(j)=u0(j)*cu0(j)
21    continue
      sum=0.0
      do 33 j=5945,6065,2
      sum=sum+(1./3.)*(charge(j)+4.*charge(j+1)+charge(j+2))
33    continue
      write(7,*) n, sum
18    continue
32    continue
      stop
    end
```

Reproduced with permission of the copyright owner. Further reproduction prohibited without permission.

A.2 A FORTRAN-77 computer program to generate the figures of chapter three

This program calculate the charge inside the double quantum well of chapter three by solving for the time dependent Schrödinger equation in the presence of electric field and electron-hole interaction. It uses as input the initial condition of the system which a photoexcited electron inside the wide well and generate the charge inside the narrow well as a function of time.

```
****************************************************************************
      dimension alpha1(21000), alpha2(21000), u0(21000)
      dimension x(21000), r0(21000), a(21000), aa(21000)
      dimension bb(21000), c(21000), v(21000), gam(21000)
      dimension alpha(21000), d(21000), charge(21000)
      dimension cu0(21000)
      complex i, u0, cu0, r0, gam, bb, bet, b
      i=(0,1)
      v0=0.230
      do 71 j=1,5000
      x(j)=0.5*float(j-1)
71    continue
      do 1 j=0,1000
      v(j)=v0
      alpha(j)=0.8372
1     continue
      open(9,file='charge.data')
      do 32 k=1,20
      va=float(k-1)/1000
      do 2 j=1001,1340
      v(j)=-(va/307.)*(x(j)-500.)
      alpha(j)=0.6097
2     continue
      do 3 j=1341,1374
      v(j)=v0-(va/307.)*(x(j)-500.)
      alpha(j)=0.8372
3     continue
      do 4 j=1375,1614
      v(j)=-(va/307.)*(x(j)-500.)
      alpha(j)=0.6097
4     continue
      do 5 j=1615,5000
      v(j)=v0-va
      alpha(j)=0.8372
5     continue
```

Reproduced with permission of the copyright owner. Further reproduction prohibited without permission.

```
      do 77 j=1,5000
      alpha1(j)=alpha(j)+alpha(j+1)
      alpha2(j)=alpha(j)+alpha(j-1)
      d(j)=alpha1(j)/alpha2(j)
77    continue
      do 6 j=0,5000
      if(j.gt.1340)go to 7
      if(j.lt.1000)go to 7
      u0(j)=sin(3.14158*(x(j)-500.)/170.)
      go to 6
7     u0(j)=(0.0,0.0)
6     continue
      do 12 j=1,5000
      a(j)=d(j)
      b(j)=4.74e-03*alpha1(j)*i-3.6e-03*v(j)*alpha1(j)-1.-a(j)
      c(j)=1.00
      bb(j)=4.74e-03*alpha1(j)*i+3.6e-03*v(j)*alpha1(j)+1.+a(j)
12    continue
      do 18 n=1,4000
      write(6,*)n
      do 13 j=1,5000
      r0(j)=-u0(j+1)+bb(j)*u0(j)-a(j)*u0(j-1)
13    continue
      bet=b(1)
      u0(1)=r0(1)/bet
      do 14 j=2,4999
      gam(j)=c(j-1)/bet
      bet=b(j)-a(j)*gam(j)
      u0(j)=(r0(j)-a(j)*u0(j-1))/bet
14    continue
      do 16 j=4998,1,-1
      u0(j)=u0(j)-gam(j+1)*u0(j+1)
16    continue
      do 21 j=1,20000
      cu0(j)=conjg(u0(j))
      charge(j)=u0(j)*cu0(j)
21    continue
      sum=0.0
      do 33 j=1374,1614,2
      sum=sum+(1./3.)*(charge(j)+4.*charge(j+1)+charge(j+2))
33    continue
      write(9,*) n, sum
18    continue
32    continue
      stop
      end
```

Reproduced with permission of the copyright owner. Further reproduction prohibited without permission.

A.3 A FORTRAN-77 computer program to generate the figures of chapters four and five.

This program solves for the electron tunneling through the double barrier structure of chapters four and five. It calculates the electron tunneling current density in chapter four in the presence of electron interacting with plane wave LO-phonons, while in chapter five it calculate the charge build-up inside the quantum well of chapter five double barrier structure in the presence of electron-localized phonon mode interaction. In both cases the initial wave function is used as the input to the program.

```
***********************************************************
      dimension alpha1(21000), alpha2(21000), u0(21000)
      dimension u1(21000), u2(21000), r1(21000), r2(21000)
      dimension cu1(21000), cu2(21000), cuden0(5000)
      dimension cuden1(5000), cuden2(5000), cuden(5000)
      dimension x(21000), r0(21000), a(21000), aa(21000)
      dimension bb(21000), c(21000), v(21000), gam(21000)
      dimension alpha(21000), d(21000), charge(21000)
      dimension cu0(21000), cc(5,5), dd(5,5), ss(5,5)
      complex i, u0, u1, u2, cu0, cu1, cu2, r0, gam, bb, bet, b
      complex r1,r2, cc, dd, ss,
      i=(0,1)
      v0=0.280
      w=0.05495
      g=0.1
      enq=0.3277
      gg=(1-g*(enq+1.)-g*enq)
      do 1 j=0,5884
      v(j)=0.0
      alpha(j)=0.6097
1     continue
      do 2 j=5885,5940
      v(j)=v0
      alpha(j)=0.8372
2     continue
      do 3 j=5941,6030
      v(j)=0.0
      alpha(j)=0.6097
3     continue
      do 4 j=6031,6086
      v(j)=v0
      alpha(j)=0.8372
```

Reproduced with permission of the copyright owner. Further reproduction prohibited without permission.

```
4       continue
        do 5 j=6087,20000
        v(j)=0.0
        alpha(j)=0.6097
5       continue
        do 71 j=1,20000
        x(j)=0.5*float(j-1)
71      continue
        do 77 j=1,20000
        alpha1(j)=alpha(j)+alpha(j+1)
        alpha2(j)=alpha(j)+alpha(j-1)
        d(j)=alpha1(j)/alpha2(j)
77      continue
        open(7,file='charge.data')
        do 32 k=91,91
        e=float(k-1)
        ak=4.19e-03*sqrt(e)
        do 6 j=0,20000
        if(j.gt.5884)go to 7
        if(j.lt.100)go to 7
        u0(j)=exp(i*ak*x(j))*exp(-(x(j)-1450.)**2/6.05e+5)
        go to 6
7       u0(j)=(0.0,0.0)
6       continue
        do 12 j=1,20000
        aa(j)=2.3719e-03*w*alpha1(j)
        a(j)=d(j)
        b(j)=4.74e-03*alpha1(j)*i-3.6e-03*v(j)*alpha1(j)-1.-a(j)
        c(j)=1.00
        bb(j)=4.74e-03*alpha1(j)*i+3.6e-03*v(j)*alpha1(j)+1.+a(j)
12      continue
        do 18 n=1,1000
        write(6,*)n
        do 13 j=1,20000
        r0(j)=-u0(j+1)+bb(j)*u0(j)+(g/gg)*aa(j)*exp(-i*w*n)*
&       (enq+1.)*u2(j)+(g/gg)*aa(j)*exp(i*w*n)*enq*u1(j)-a(j)
&       *u0(j-1)
        r1(j)=-u1(j+1)+bb(j)*u1(j)+gg*aa(j)*exp(-i*w*n)*u0(j)
&       -a(j)*u1(j-1)
        r2(j)=-u2(j+1)+bb(j)*u2(j)+gg*aa(j)*exp(i*w*n)*u0(j)
&       -a(j)*u2(j-1)
13      continue
        bet=b(1)
        u0(1)=r0(1)/bet
        u1(1)=r1(1)/bet
        u2(1)=r2(1)/bet
        do 14 j=1,19999
        gam(j0=c(j-1)/bet
        bet=b(j)-a(j)*gam(j0
        cc(1,1)=bet
        cc(1,2)=-aa(j)*(g/gg)*enq*exp(i*w*(n+1))
```

Reproduced with permission of the copyright owner. Further reproduction prohibited without permission.

```
      cc(1,3)=-aa(j)*(g/gg)*(enq+1)*exp(-i*w*(n+1))
      cc(1,4)=r0(j)-a(j)*u0(j-1)
      cc(2,1)=-gg*aa(j)*exp(i*w*(n+1))
      cc(2,2)=bet
      cc(2,3)=(0.0,0.0)
      cc(2,4)=r1(j)-a(j)*u1(j-1)
      cc(3,1)=-gg*aa(j)*expi*w*(n+1))
      cc(3,2)=(0.0,0.0)
      cc(3,4)=r2(j)-a(j)*u2(j-1)
      do 57 k1=1,4
      dd(1,k1)=cc(1,k1)
      dd(2,k1)=cc(1,k1)*(cc(2,1)/cc(1,1))-cc(2,k1)
      dd(3,k1)=cc(1,k1)*(cc(3,1)/cc(1,1))-cc(3,k1)
      ss(1,k1)=dd(1,k1)
      ss(2,k1)=dd(2,k1)
      ss(3,k1)=dd(2,k1)*(dd(3,2)/dd(2,2))-dd(3,k1)
57    continue
      u2(j)=ss(3,4)/ss(3,3)
      u1(j)=(ss(2,4)-u2(j)*ss(2,3))/ss(2,2)
      u0(j)=(ss(1,4)-u1(j)*ss(1,2)-u2(j)*ss(1,3))/ss(1,1)
14    continue
      do 16 j=19998,1,-1
      u0(j)=u0(j)-gam(j+1)*u0(j+1)
      u1(j)=u1(j)-gam(j+1)*u1(j+1)
      u2(j)=u2(j)-gam(j+1)*u2(j+1)
16    continue
      do 21 j=1,20000
      cu0(j)=conjg(u0(j))
      cu1(j)=conjg(u1(j))
      cu2(j)=conjg(u2(j))
21    continue
      cuden0(n)=(1./i)*(cu0(6100)*u0(6101)-u0(6100)*
&     cu0(6101))*(gg**2)
      cuden1(n)=(1./i)*(cu1(6100)*u1(6101)-u1(6100)*
&     cu1(6101))*(g*enq)
      cuden2(n)=(1./i)*(cu2(6100)*u2(6101)-u2(6100)*
&     cu2(6101))*(g*(enq+1))
      cuden(n)=cuden0(n)+cuden1(n)+cuden2(n)
      write(7,*)n,cuden(n)
18    continue
32    continue
      stop
      end
```

Reproduced with permission of the copyright owner. Further reproduction prohibited without permission.

A.4 A FORTRAN-77 computer program to generate the figures of chapter six

This program calculates the electron tunneling short circuit current density and electron tunneling probability through a multiple quantum well structure suitable for solar cell applications. The input is an initial wave function of the photoexcited electron in one of the quantum well. It generate the current density reaching the collector side of the cell structure.

```
*************************************************
      dimension  alpha1(21000), alpha2(21000), u0(21000)
      dimension x(21000), r0(21000), a(21000), aa(21000)
      dimension bb(21000), c(21000), v(21000), gam(21000)
      dimension alpha(21000), d(21000), charge(21000)
      dimension cu0(21000)
      complex i, u0, cu0, r0, gam, bb, bet, b
      i=(0,1)
      v0=0.500
      do 71 j=1,5000
      x(j)=0.5*float(j-1)
71    continue
      do 1 j=0,1000
      v(j)=v0
      alpha(j)=0.8372
1     continue
      open(9,file='charge.data')
      do 32 k=522,522
      va=float(k-1)/10000
      do 2 j=1001,1240
      v(j)=-(va/522.0)*(x(j)-500.)
      alpha(j)=0.6097
2     continue
      do 3 j=1241,1280
      v(j)=v0-(va/522.0)*(x(j)-500.)
      alpha(j)=0.8372
3     continue
      do 4 j=1281,1473
      v(j)=-(va/522.)*(x(j)-500.)
      alpha(j)=0.6097
4     continue
      do 50 j=1474,1513
      v(j)=v0-(va/522.0)*(x(j)-500.)
```

Reproduced with permission of the copyright owner. Further reproduction prohibited without permission.

```
      alpha(j)=0.8372
50    continue
      do 51 j=1514,1680
      v(j)=-(va/522.)*(x(j)-500.)
      alpha(j)=0.6097
51    continue
      do 52 j=1681,1720
      v(j)=v0-(va/522.0)*(x(j)-500.)
      alpha(j)=0.8372
52    continue
      do 53 j=1721,1869
      v(j)=-(va/522.)*(x(j)-500.)
      alpha(j)=0.6097
53    continue
      do 54 j=1870,1909
      v(j)=v0-(va/522.0)*(x(j)-500.)
      alpha(j)=0.8372
54    continue
      do 55 j=1910,2045
      v(j)=-(va/522.)*(x(j)-500.)
      alpha(j)=0.6097
55    continue
      do 56 j=2045,2055
      v(j)=v0-(va/522.0)*(x(j)-500.)
      alpha(j)=0.8372
54    continue
      do 5 j=2046,5000
      v(j)=-va
      alpha(j)=0.8372
5     continue
      do 77 j=1,5000
      alpha1(j)=alpha(j)+alpha(j+1)
      alpha2(j)=alpha(j)+alpha(j-1)
      d(j)=alpha1(j)/alpha2(j)
77    continue
      do 6 j=0,5000
      if(j.gt.1340)go to 7
      if(j.lt.1000)go to 7
      u0(j)=sin(3.14158*(x(j)-500.)/120.)
      go to 6
7     u0(j)=(0.0,0.0)
6     continue
      do 12 j=1,5000
      a(j)=d(j)
      b(j)=4.74e-03*alpha1(j)*i-3.6e-03*v(j)*alpha1(j)-1.-a(j)
      c(j)=1.00
      bb(j)=4.74e-03*alpha1(j)*i+3.6e-03*v(j)*alpha1(j)+1.+a(j)
12    continue
      do 18 n=1,4000
      write(6,*)n
      do 13 j=1,5000
```

Reproduced with permission of the copyright owner. Further reproduction prohibited without permission.

```
      r0(j)=-u0(j+1)+bb(j)*u0(j)-a(j)*u0(j-1)
13    continue
      bet=b(1)
      u0(1)=r0(1)/bet
      do 14 j=2,4999
      gam(j)=c(j-1)/bet
      bet=b(j)-a(j)*gam(j)
      u0(j)=(r0(j)-a(j)*u0(j-1))/bet
14    continue
      do 16 j=4998,1,-1
      u0(j)=u0(j)-gam(j+1)*u0(j+1)
16    continue
      do 21 j=1,20000
      cu0(j)=conjg(u0(j))
      charge(j)=u0(j)*cu0(j)
21    continue
      cuden(n)=(1/i)*(cu0(2100)*u0(2101)-u0(2100)*cu0(2101))
      write(9,*)n,cuden(n)
18    continue
32    continue
      stop
      end
```

Reproduced with permission of the copyright owner. Further reproduction prohibited without permission.

BIBLIOGRAPHY

Bar-Joseph, I. Y.,Gedalyahu, A. Yacoby, T. Woodward, D. Shemla, D. Sivco, and A. Cho, Phys. Rev. B **44**, 8361 (1991).

Barnham, K. W. J. and G. Duggan, J. Appl. Phys. **67**, 3490 (1990).

BenDanil, D. J. and C. B. Duke, Phys. Rev. **152**, 683 (1966).

Brown, E. R., J. R. Soderstrom, C. D. Parker, L. J. Mahoney, K. M. Mplvar, and T. C. McGill, Appl. Phys. Lett. **58**, 2291 (1991).

Cai, W., T. F. Zheng, P. Hu, B. Yudanin, and M. Lax, Phys. Rev. Lett. **63**, 418 (1989).

Capasso, F., K. Mohammad, and A. Y. Cho, IEEE J. Quantum Electron. **QE-22**, 1853 (1986).

Collins, S., D. Lowe, and J. R. Barker, J. Phys. C: Solid state Phys. **20**, 6213 (1987).

Deveaud, B., A. Chomette, F. Clerot, P. Auvrsy, A. Regreny, R. Ferreira, and G. Bastard, Phys. Rev. B, **42**, 7021 (1990).

Esaki, L. and L. L. Chang, Phys. Rev. Lett. **33**, 495 (1974).

Esaki, L. Phys. Rev. **109**, 603 (1957).

Fowler, R. H. and L. Nordheim, Proc. Roy. Soc. (London), **A119**, 173 (1928).

Frenkel, J., Phys. Rev. **36**, 1604 (1930).

Gelfand, B. Y., S. Schmitt-Rink, and A. F. J. Levi, Phys. Rev. Lett. **62**, 1683 (1989).

Reproduced with permission of the copyright owner. Further reproduction prohibited without permission.

Goldberg, A., H. M. Schey, and J. C. Swarts, Am. J. Phys. **35**, 177 (1967).

Goldman, V. J. D. C. Tsui, and J. E. Cunningham, Phys. Rev. B **36**, 7635 (1987).

Gou, H., K. Diff, G. Neofotistos, and J. Gunton, Appl. Phys. Lett. **53**, 131 (1988).

Henry, C. H. J. App. Phys. **51**, 4494 (1980).

Jauho, A. P. and M. Johnson, *Superlattices and Microstructures*, **6**, 303 (1989).

Jauho, A. P. and M. Nieto, *Superlattices and Microstructures,* **2**, 407 (1986).

Jauho, A. P., Phys. Rev. B, **41**, 12327 (1990).

Juang, C. K., J. Kuhn, and R. B. Darling, Phys. Rev. B, **41**, 12047 (1990).

Kaminar, N. R., D. D. Liu, H. F. MacMillan, L. D. Partain, M. Ladle Ristow, G. F. Virshup, and J. M. Gee, in *Proceedings of the 20th IEEE Photovoltaic Specialisits Conference* (IEEE, New York, 1988), p. 766.

Larsson, A. P., A. Andrekson, S. T. Eng, and A. Yariv, IEEE, **24**, 787 (1988).

Leo, Karl, J. Shah, E. Göbel, T. Damen, S. Schmitt, W. Schafer, and K. Köhler, Phys. Rev. Lett. **66**, 201 (1991).

Matsusue, T., M.Tsychiya, J. Shulman, and H. Sakaki, Phys. Rev. B, **42**, 5719 (1990).

Mohaidat, Jihad M., Kai Shum, and R. R. Alfano, Phys. Rev. B, **45**, 3822 (1992).

Reproduced with permission of the copyright owner. Further reproduction prohibited without permission.

Mohaidat, Jihad M., Kai Shum, and R. R. Alfano, Phys. Rev. B, **48**, 8809 (1993).

Mohaidat, Jihad M., Kai Shum, and R. R. Alfano, submitted for publication in Phys. Rev. B

Mohaidat, Jihad M., Kai Shum, and R. R. Alfano, submitted for publication in *Solid State Communication.*

Mohaidat, Jihad M., Kai Shum, and R. R. alfano, SPIE *Proceedings,* Vol. 1677 (1992).

Mohaidat, Jihad M., Kai Shum, W. B. Wang, and R. R. alfano, submitted for publication in Phys. Rev. B.

Olson, J. M., S. R. Kurts, and A. E. Kibbier, in *Proceedings of the 15th IEEE Photovoltaic Specialists Conference* (IEEE, New York, 1988), P. 777.

Oppenheimer, J. R., Phys. Rev. **31**, 66 (1928).

Pauwels, H. and A. de Vos, in *Proceedings of the 15th IEEE Photovoltaic Specialists Conference* (IEEE, New York, 1981), P. 377.

Rucher, H., E. Molinari and P. Lugli, Phys. Rev. B, **44**, 3463 (1991)

Summers, C. J. and K. F. Brenan, Appl. Phys. Lett. **48**, 806, (1986).

Sze, S. *Physics of Semiconductors* (Wiley, New York, 1981), p. 256.

Tsu, R. and L. Esaki, Appl. Phys. Lett. **22**, 562 (1973).

Tsuchiya, M., T. Matsusue, and H. Sakaki, Phys. Rev. Lett. **59**, 2356 (1987).

Reproduced with permission of the copyright owner. Further reproduction prohibited without permission.

Tsuchiya, M., T. Matsusue, and H. Sakaki, Phys. Rev. Lett. **59**, 2356 (1987).

Turely, P. J. and S. Teitsworth, J. Appl. Phys. **72**, (6) 2356 (1992)

Wendler, L. and R. Pechstedt, Phys. stat. Sol. (b) **141**, 129 (1987)

Wendler, L., Phys. Stat. Sol. (b) **129**, 513 (1985).

Wingreen, N. S., K. W. Jacoobson, and J. W. Wilkins, Phys. Rev. Lett. **61**, 1396 (1988).

Yoshimura, H., J. Schulman, and H. Sakaki, Phys. Rev. Lett. **64**, 2422 (1990).

Young, J., B. Wood, G. Aers, R. Devine, H. Liu, D. Landheer, M. Buchanan, A. SpringThrope, and P. Mandeville, Phys. Rev. Lett. **60**, 2085 (1988).

Zhang, Jin-feng and Ben-yuan Gu, Phys. Rev. B, **43**, 5028 (1991).

Reproduced with permission of the copyright owner. Further reproduction prohibited without permission.